

8. SITE 838¹

Shipboard Scientific Party²

HOLE 838A

Date occupied: 11 January 1991
Date departed: 13 January 1991
Time on hole: 1 day, 10 hr, 11 min
Position: 20°49.618'S, 176°53.402'W
Bottom felt (rig floor; m, drill-pipe measurement): 2333.8
Distance between rig floor and sea level (m): 11.0
Water depth (drill-pipe measurement from sea level, m): 2322.8
Total depth (rig floor; m): 2487.60
Penetration (m): 153.80
Number of cores (including cores with no recovery): 20
Total length of cored section (m): 153.80
Total core recovered (m): 98.65
Core recovery (%): 64.2
Oldest sediment cored:
Depth (mbsf): 153.80
Nature: basaltic gravel
Earliest age: late Pliocene
Measured velocity (km/s): 2.4

HOLE 838B

Date occupied: 13 January 1991
Date departed: 15 January 1991
Time on hole: 5 hr, 15 min
Position: 20°49.629'S, 176°53.402'W
Bottom felt (rig floor; m, drill-pipe measurement): 2333.8
Distance between rig floor and sea level (m): 11.10
Water depth (drill-pipe measurement from sea level, m): 2322.7
Total depth (rig floor; m): 2593.00
Penetration (m): 259.20
Number of cores (including cores with no recovery): 13
Total length of cored section (m): 115.20
Total core recovered (m): 1.5
Core recovery (%): 1.3
Oldest sediment cored:
Depth (mbsf): 259.20
Nature: vitric sandstone and claystone
Earliest age: late Pliocene
Measured velocity (km/s): 1.9

Principal results: Site 838 is located in the central Lau Basin, approximately 87 km west of the active backarc axis of the Eastern Lau Spreading Center (ELSC) and about 125 km east of the axis of the Lau Ridge. The regional topography at the site is dominated by broad, north-south-striking linear basins and highs, ranging in water depths between <1500 m and >2900 m. Approximately 50 km to the west of the site, a tectonically (and probably volcanically) active rift structure has been identified on long-range sidescan data. One suggestion is that it may represent a site of off-axis magmatism along an extinct ridge, the Western Lau Spreading Center. The site is close to an arbitrary north-south line separating the Lau Basin floor, characterized by a style of rifting and magmatism different from "normal" seafloor spreading such as that occurring at the ELSC. Interpretations of the magnetic anomaly fabrics at Site 838, however, suggest an origin by a simple seafloor spreading mechanism, with an age of 2 Ma for the crust beneath the site. The principal objectives for the site were (1) to assess the age and the chemistry of the basement rocks and to determine their petrogenetic relationship to those recovered at other sites throughout the basin; (2) to sample the overlying sedimentary sequence to review variations in carbonate, clay, and volcanoclastic components and to determine their likely source and stratigraphic relationships to other marker units identified during Leg 135, but especially at Sites 836 and 837; and (3) to identify the tectonic setting of the site in terms of models of backarc ridge relocation by ridge jump, ridge migration, or asymmetric spreading.

The sedimentary sequence recovered at Site 838 is 103.2 m thick and ranges in age from middle Pleistocene to the upper Pliocene (Fig. 1). The sequence is subdivided lithologically into three units. Unit I comprises clayey nannofossil oozes with thin volcanoclastic turbidite interbeds and extends down to 23.04 mbsf. Unit II, which is subdivided into five subunits, comprises volcanic gravel (pumice and glass), vitric sands, vitric silts, and clayey nannofossil ooze, and is characterized by an overall upward-fining sequence. The entire Unit I and the upper sequences of Unit II carry abundant, well-preserved fauna and flora and the Pleistocene/Pliocene boundary at the base of the nannofossil Subzone CN14a is identified within Subunit IIc. The sediments of Unit II were deposited by mass-flow processes, probably derived from a source toward the south or southwest, based on regional bathymetric trends. The rapid deposition locally resulted in poor biostratigraphic control, and the thick turbiditic sections resulted in a number of barren intervals.

Such fauna and flora that are present are well-preserved and moderately abundant throughout lower Unit II and Unit III. The deepest sedimentary unit, Unit III, extends through 98.7–259.2 mbsf, but the detailed lithostratigraphy is poorly constrained because of low recovery. The recovered sediments consist of pumiceous volcanic gravel, conglomerate, vitric sandstone, and vitric clayey siltstone. The sediment accumulation rates for Site 838 vary from 177 mm/k.y. for 55.0–94.0 mbsf; through 47 mm/k.y. for the 18.0–55.0 mbsf interval; to 21 mm/k.y. for the most recent section above 18.0 mbsf. The volcanoclastics at Site 838 are dominated throughout by pumiceous material of rhyodacite composition, but there is also a minor component of basaltic andesite glass and lithic fragments. Basement was not reached at Site 838, but igneous rock fragments recovered from the breccias and very coarse sand layers comprise plagioclase-pyroxene phyric andesite (54%–57% SiO₂) and plagioclase-amphibole-quartz phyric pumice with 70%–72% SiO₂. Quartz and cryptocrystalline silica occur as secondary phases.

The unstable sediments hampered the identification of a smooth magnetic stratigraphy. The Brunhes-Matuyama (0.73 Ma), Jaramillo (0.98 Ma), and Cobb Mountain (1.13 Ma) magnetic events were

¹ Parson, L., Hawkins, J., Allan, J., et al., 1992. *Proc. ODP, Init. Repts.*, 135: College Station, TX (Ocean Drilling Program).

² Shipboard Scientific Party is as given in the list of participants preceding the contents.

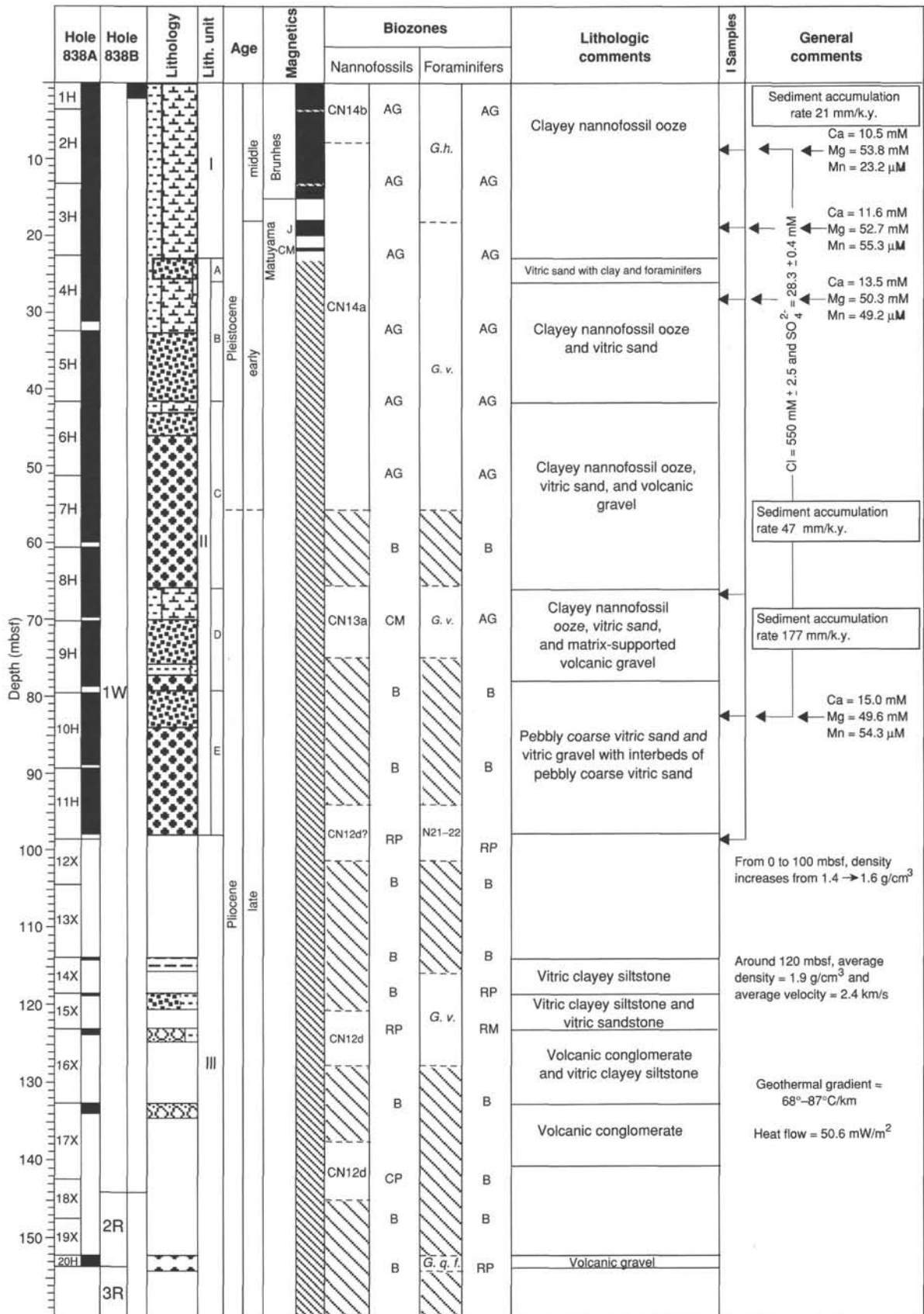


Figure 1. Site summary, Site 838. Abbreviations for abundance are as follows: A = abundant, C = common, F = few, R = rare, and B = barren. Those for preservation are as follows: G = good, M = moderate, and P = poor. Planktonic foraminifer zones are abbreviated as follows: *G. h.* = *Globorotalia crassaformis hessi*, *G. v.* = *Globorotalia crassaformis viola*, and *G. q. f.* = *Globigerinoides quadrilobatus fistulosus*.

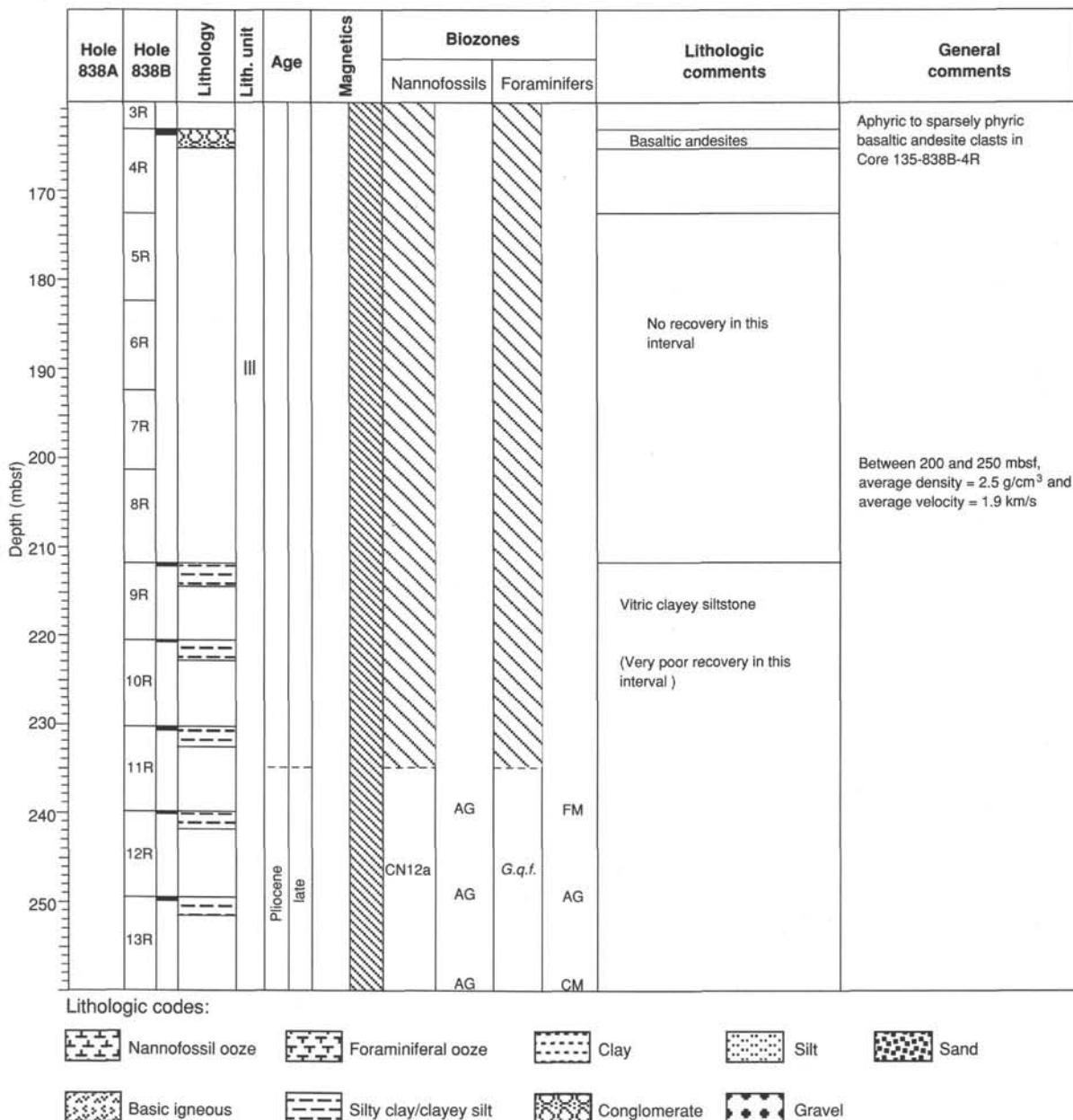


Figure 1 (continued).

distinguished, but the shortness of the sedimentary column in the Brunhes Chron suggested that part of it is missing at this site.

Only background levels of hydrocarbons were detected at Site 838. Low methane concentrations indicate that methanogenesis was not occurring, probably because levels of organic carbon were too low to sustain microbial activity. A low gradient in dissolved calcium and magnesium concentration-depth profiles calculated from interstitial water samples suggests a diffuse exchange with the underlying igneous basement. The limited pore-water data confirm the downwelling of seawater through the stratigraphic section as found at previous sites, but with more basement exchange at Site 838 than at the other sites.

Physical properties measurements for Site 838 show a wide scatter caused by the variations in interbedded lithologies. Bulk density, porosity, water content, and void ratio decrease with depth in the section, down to 200 mbsf. Below this point, however, all three index properties increase significantly, indicating that the deeper part of the section is probably underconsolidated, with high pore pressures preventing continued consolidation of the sediments at the base of the

hole. The temperature gradient at the site is 8.7°C/100 m, the highest recorded in any of the sites.

BACKGROUND AND OBJECTIVES

Background

Location and Bathymetry

Site 838 is located in the central Lau Basin about 125 km east of the Lau Ridge remnant arc and approximately 87 km west of the axial rift zone of the Eastern Lau Spreading Center (ELSC) (Fig. 2). The site is located at 20°49.6'W, 176°53.4'W. The ELSC is the presently active site of generation of new backarc basin crust at the latitude of the drill site. Site 838, however, is located on older crust that may have had its origin at a zone of crustal extension different from the ELSC. The bathymetry and GLORIA imagery show that the site is in a region of north to northeasterly

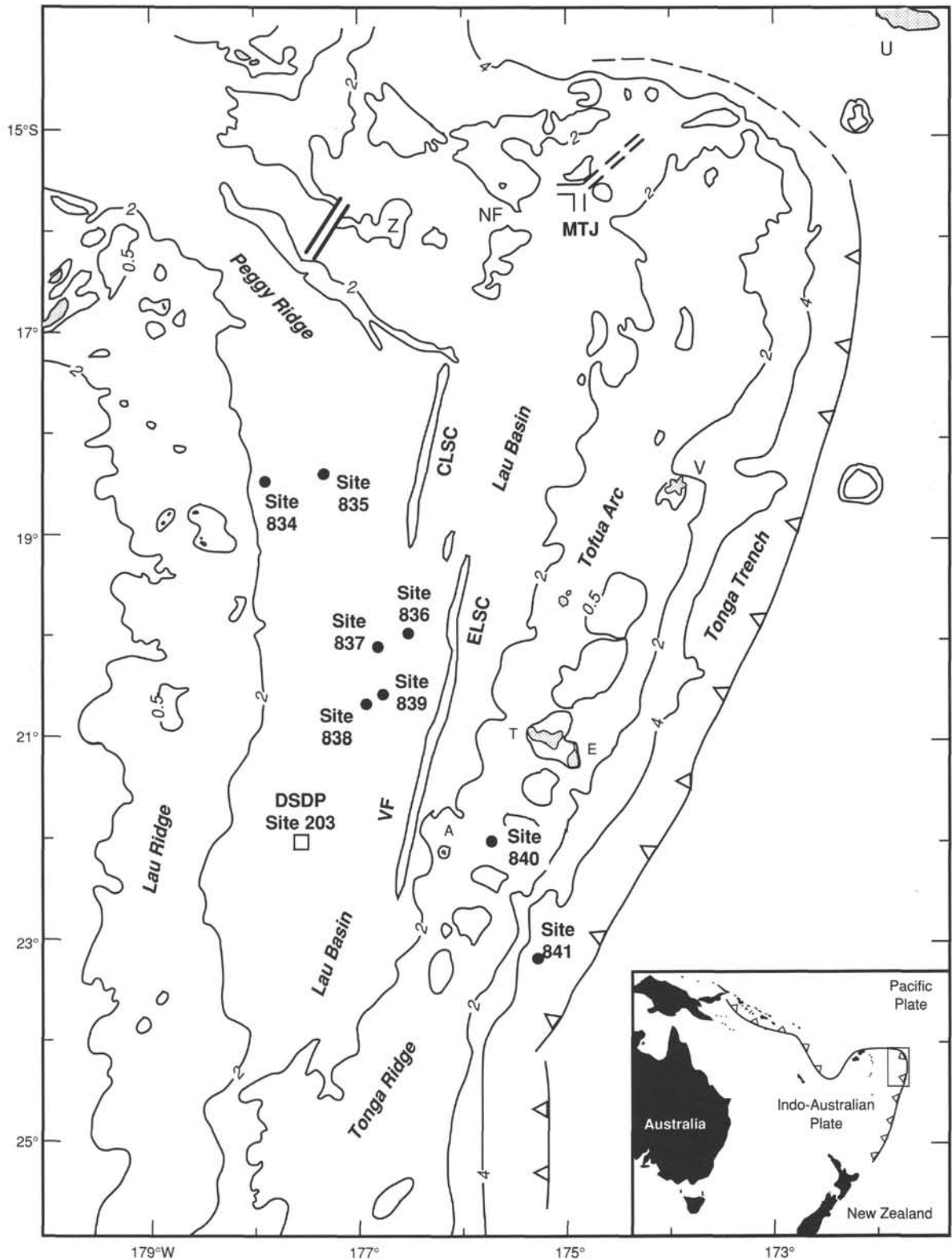


Figure 2. Bathymetry of the Lau Basin region and location of Site 838 sites. The figure also illustrates the regional setting for the locations of other drill sites in the Lau Basin and the major geologic features of the Tonga Trench and Lau Basin system. Z = Zephyr Shoal; islands include T = Tongatapu, E = 'Eua, V = Vavau, NF = Niua Fo'ou, A = Ata, and U = Upolu. Locations of the Central Lau (CLSC) and Eastern Lau (ELSC) spreading centers, Valu Fa Ridge (VF), and Mangatolu Triple Junction (MTJ) are from von Stackelberg (1990), Parson et al. (1989), Hawkins et al. (1989), and Nilsson et al. (1989). The location of DSDP Site 203 is shown as an open square. Contours in thousands of meters.

striking ridges and deeps interpreted as horsts and grabens or half-grabens.

In this discussion we will use the term "Basin 838" for the irregularly shaped, narrow, linear, sedimented trough in which the drill site is located. A bathymetric sketch chart based on echo-sounder depth data and GLORIA imagery is shown in Figure 3. Basin 838 is at least 7.5 km long on its northeast-southwest axis and about 8.2 km wide in a north-south direction as delimited by the 2200-m isobath. The maximum bathymetric relief is about 1400 m with ridges shoaling to <1500 m, rising above basins, some of which exceed 2900-m depth. The site is on a narrow terrace, at a depth of 2338 m, situated on the southwest side of a bathymetric high that rises to <1900 m. At the western limit of our bathymetric coverage the basin is about 6 km wide but it is complicated by faults which cause it to narrow to about 2 km or less at the eastern end (Fig. 4).

The site was selected to give data for a part of the Lau Basin crust estimated to be intermediate in age between the oldest backarc crust (e.g., Site 834) and young crust formed at the axial rift of the ELSC.

Geologic Setting

Our estimates of crustal ages in the Lau Basin have been based on interpretations of regional magnetic anomaly patterns. As discussed in the "Introduction and Principal Results" chapter (this volume), there are many problems in assigning ages of the crust at places more than about 50 km from the ELSC and Central Lau Spreading Center (CLSC). The best estimate for Site 838 was that it was older than 1 Ma and probably 2 Ma or younger. Additional data for heat flow and rock types are in the "Background and

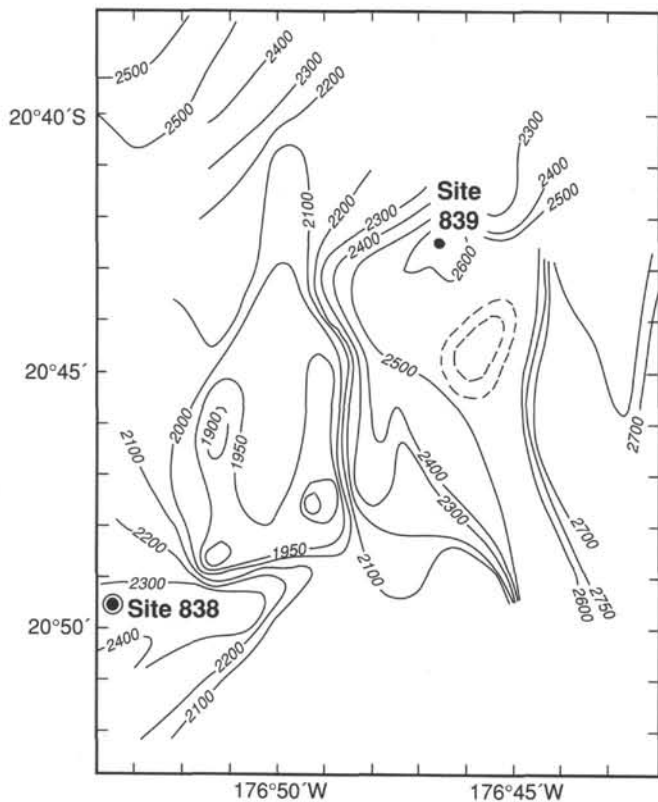


Figure 3. Bathymetric sketch chart showing the locations of Sites 838 and 839 in the central Lau Basin. The chart is based on seismic and conventional echo-sounder surveys combined with interpreted GLORIA data. Contours in meters.

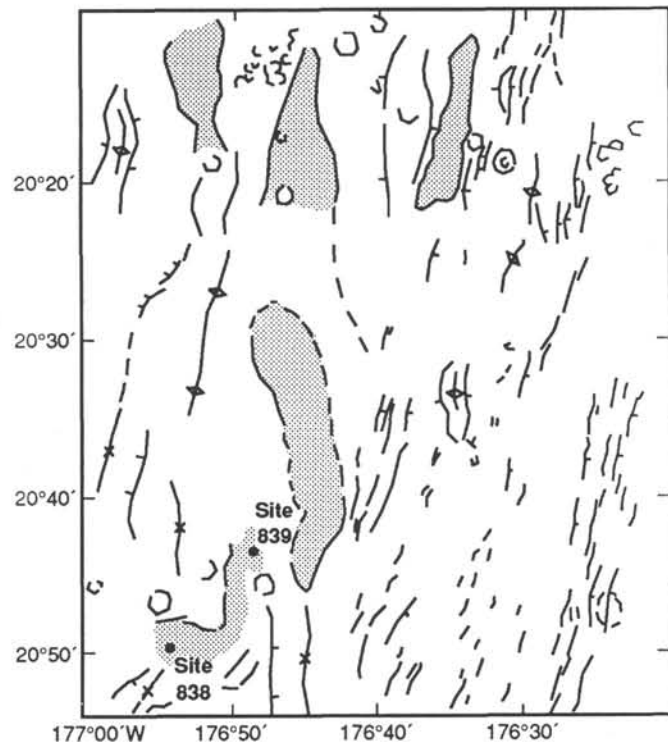


Figure 4. Morphotectonic sketch of the seafloor around Sites 838 and 839, derived from combined SeaBeam and GLORIA data. Stippled areas denote principal sedimented basins. Schematic tectonic and volcanic fabrics marked as lines with conventional structural symbols. Circular features locate volcanoes.

Objectives" section, "Site 836" chapter (this volume). A sketch map showing major morphologic and tectonic features near Basin 838 is in Figure 4.

The main bathymetric grain in the area is in a north-northeast-south-southwest direction, but Basin 838 trends about east-northeast. The basin is transected by a narrow arch that trends northerly and separates it into two segments. Site 838 is in the southwestern of these smaller basin segments. Part of the basin floor is crossed by linear and curved traces of highly reflective features, as seen on the GLORIA images, suggesting young fault scarps which cut the sedimented basin floor. These scarps define arcuate patterns, convex to the southeast, with limbs trending 035° and 240°. Ridges up to 375 m high bound both the northwest and southeast sides of the basin and are assumed to be controlled by steeply dipping faults. Some of the steep ridge flanks can be traced deeper into the seismic section, and locally deeper horizons are resolved which are provisionally interpreted as basement. A presumed basement reflector was tentatively identified at about 0.4 seconds two-way traveltime (s TWT). The apparent regional dip of the acoustic stratigraphy is toward the south.

Seismic Stratigraphy

Site 838 was selected on the basis of GLORIA data and two intersecting single channel seismic reflection profiles recorded on the *Charles Darwin* in 1988 (Parson et al., 1989) (Fig. 5A). These seismic profiles recorded 0.05 to 0.1 s TWT of sediments in the basin. Additional seismic data were collected by the *JOIDES Resolution* on the approach to the site (Fig. 5B). The seismic lines show an undulating subparallel series of reflectors in the upper 0.2 s TWT of the section which are difficult to differentiate from the gun signal (Fig. 6A). This unit overlies a diffuse zone of

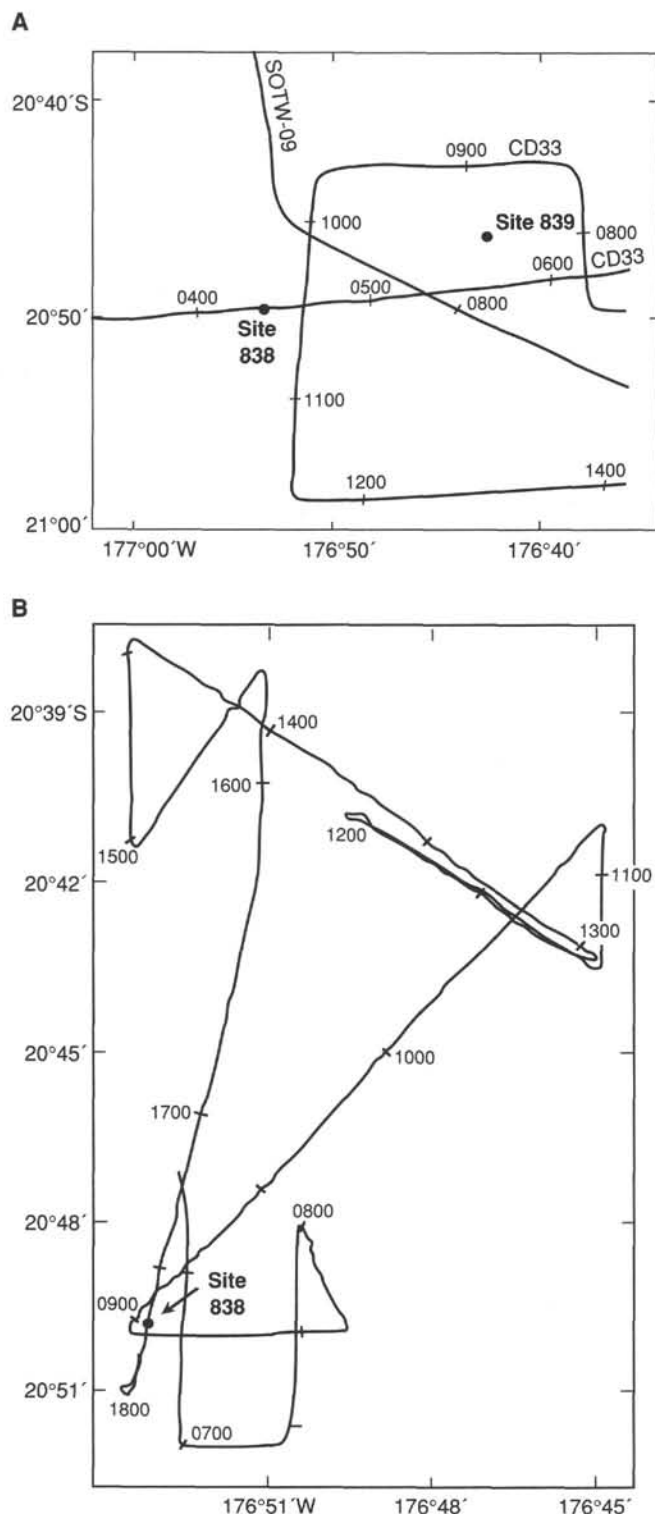


Figure 5. A. Track charts showing the locations of the seismic lines used to select Site 838, acquired by *Charles Darwin* Cruise 33 (CD33; Parson et al., 1989) and SOUTHTOW (SOTW-09; Hawkins, 1976). B. Track chart of the site approach and survey lines of the *JOIDES Resolution* at Site 838.

low-frequency reflectors which appear to dip steeply to the south and into the axis of the basin. A line interpretation of the seismic reflection profile and a seismographic interpretation of the section drilled at Site 838 are presented in Figures 6B and 6C, respectively. Because the seismic character of the strata was so different from the sections that we had sampled on the leg already, it was difficult to estimate the type or depth of the sedimentary section. The regional apparent dip of the seismic strata throughout the section is toward the south, and a tentative estimate of 100–150 m was made for the sediment thickness in the basin on the basis of the 0.1- to 0.15-s-TWT-thick upper seismic section. It was recognized, however, that the deeper reflector at 0.2 s TWT could represent “true” acoustic basement. We used the velocity values from Sites 834–837 (1675 m/s) to estimate a depth to basement of about 250 mbsf. Most of the upper seismic sequence is interpreted as the equivalent of seismic Unit A, as described in the “Introduction and Principal Results” chapter (this volume), although the profiler data are inconclusive at depth. The remainder of the section is interpreted and illustrated in Figure 6C.

Scientific Objectives

The primary objectives of Site 838 were the same as for Site 836 and are discussed in that section of the “Site 836” chapter (this volume).

OPERATIONS

Site Approach and Site Survey

Site 838 is located in the central Lau Basin, approximately 87 km west of the active backarc axis of the ELSC and about 125 km east of the axis of the Lau Ridge. The regional topography at the site is dominated by series of north-south–striking linear basins and highs, ranging in water depths from <1500 m to >2900 m.

In detail, Site 838 is situated on the northwestern flank of an irregularly shaped trough in the central Lau Basin. Intersecting single-channel seismic reflection profiles recorded by the *Charles Darwin* in 1988 (Parson et al., 1990), and the *Thomas Washington* in 1976 (Hawkins, 1976) had been used to identify the site before Leg 135 (Fig. 5A). The additional survey lines collected by the *JOIDES Resolution* were intended to define more precisely the shape of the target basin. Interpretation of the seismic data was constrained in part by the GLORIA long-range sidescan sonar coverage in the area. Inward-facing normal faults, striking approximately east-northeast–west-southwest, appear to bound a linear, sediment-filled trough in which Site 838 is located. At the western limit of coverage, the basin appears to be about 6 km wide, but is complicated at the eastern end by additional faulting that narrows the trough to <2 km. The *JOIDES Resolution* seismic data indicated a series of gently undulating subparallel reflectors in the upper 0.2 s TWT of the section (Figs. 5 and 6). This unit overlies a diffuse zone of low-frequency reflectors that appear to dip steeply toward the south and into the axis of the basin. Because the seismic character of the strata was so different from the sections we had sampled on the leg already, it was difficult to estimate the type or depth of sedimentary section. A further complication was that the optimum site appeared to have a less than suitable topographic aspect, located on a narrow terrace on the flank of the slope bounding the basin in the north. The regional apparent dip of the seismic strata throughout the section is toward the south, and a tentative estimate of sediment thickness of 100–150 m was made for the site on the basis of the 0.1- to 0.15-s-TWT-thick upper seismic section. It was recognized, however, that the deeper reflector at 0.2 s TWT could represent “true” acoustic basement. In order to convert traveltimes to depth, we based our estimated seismic velocities on values obtained from

Sites 834–837. Using a velocity of 1675 m/s, we estimated the depth to basement as around 250 mbsf.

The transit from Site 837 to Site 838 began at 0500 Universal Time Coordinated (UTC) on 11 January 1991. During the transit, one motor on the port shaft and two motors on the starboard shaft went down, causing the ship to stop for repairs. One hour total time was lost before getting underway again to the survey area. The ship slowed to 6 knots at 0615 UTC to deploy the geophysical survey equipment, which comprised two 80-in.³ water guns, the 60-element Teledyne hydrophone streamer, and the proton precession magnetometer. An 18-nmi geophysical grid survey of Site 838, including the recording of 3.5-kHz high-resolution profiler and 12-kHz echo-sounder data, began at 0635 UTC and was completed by 0939 UTC. On completion of this first site survey grid for Site 838, the lines were continued to the north and northeast to provide further seismic reflection coverage in the area of a proposed Site 839. This additional survey was completed by 1600 UTC and we returned to Site 838, recrossing the site with another survey line and dropping the beacon at 1814 UTC (Fig. 5B). The underway geophysical equipment was recovered immediately after the beacon drop and we proceeded to the site to begin drilling operations.

Drilling and Logging Summary

It was our intention to drill two holes at Site 838. The first hole would sample the sedimentary section, using the advanced piston

corer (APC) until refusal, to be followed by use of the extended core barrel (XCB) system. The second hole would be drilled with the rotary core barrel (RCB), and would wash down through the sediments to just above refusal depth. If necessary, at this second hole we would continue to sample sediments, thereafter continue into basement, and sample a shallow (50-m) section of igneous basement which appears from earlier data to be inclined toward the southeast. The *JOIDES Resolution* seismic data acquired during the site survey did not help clarify our uncertainty about the depth to basement.

Hole 838A

Hole 838A was spudded in at 0035 UTC on 12 January 1991, at 20°49.618'S, 176°53.402'W, with an 11⁷/₁₆-in. bottom-hole assembly (BHA). With Core 135-838A-1H we determined the water depth at 2333.8 m below the driller's datum, and recovered 3.76 m (Table 1). Continuous APC cores were taken from 0 to 98.7 mbsf (Cores 135-838A-1H to -11H), with a recovery of 95.52 m (96.8%). The sediments recovered were nannofossil ooze and clay with interbedded, unstable volcanoclastic sands and gravels. Frequent mud sweeps were required to keep the hole clean. Cores 135-838A-4H to -6H were oriented using the multishot tool, and water sampler temperature probe (WSTP) measurements were taken at 32.2 and 51.2 mbsf. Orientation and heat flow measurements were terminated after Core 135-838A-6H because of sloughing into the hole.

Table 1. Coring summary, Site 838.

Core no.	Date (Jan. 1991)	Time (local)	Depth (mbsf)	Cored (m)	Recovered (m)	Recovery (%)	Age
135-838A-							
1H	12	0050	0.0–3.7	3.7	3.76	101.0	middle Pleistocene
2H	12	0120	3.7–13.2	9.5	9.46	99.6	middle Pleistocene
3H	12	0150	13.2–22.7	9.5	9.85	103.0	lower Pleistocene
4H	12	0225	22.7–32.2	9.5	8.70	91.6	lower Pleistocene
5H	12	0415	32.2–41.7	9.5	9.82	103.0	
6H	12	0455	41.7–51.2	9.5	9.35	98.4	
7H	12	0640	51.2–60.7	9.5	8.98	94.5	Barren
8H	12	0730	60.7–70.2	9.5	9.10	95.8	upper Pliocene
9H	12	0805	70.2–79.7	9.5	8.77	92.3	Barren
10H	12	0850	79.7–89.2	9.5	9.28	97.7	Barren
11H	12	0925	89.2–98.7	9.5	8.44	88.8	upper Pliocene
12X	12	1025	98.7–104.2	5.5	0.00	0.0	Barren
13X	12	1130	104.2–113.9	9.7	0.00	0.0	Barren
14X	12	1320	113.9–118.5	4.6	0.32	7.0	upper Pliocene
15X	12	1600	118.5–123.1	4.6	0.32	7.0	upper Pliocene
16X	12	1750	123.1–132.8	9.7	0.68	7.0	Barren
17X	12	1935	132.8–142.4	9.6	0.14	1.5	upper Pliocene
18X	12	2100	142.4–147.4	5.0	0.00	0.0	Barren
19X	12	2215	147.4–152.1	4.7	0.00	0.0	
20H	12	2315	152.1–153.8	1.7	1.68	98.8	upper Pliocene
Coring totals				153.8	98.65	64.1	
135-838B-							
1W	13	1345	0.0–144.0	144.0	2.12	(wash core)	
2R	13	1505	144.0–153.7	9.7	0.01	0.1	upper Pliocene
3R	13	1610	153.7–163.2	9.5	0.00	0.0	
4R	13	1730	163.2–172.7	9.5	0.05	0.5	
5R	13	1835	172.7–182.4	9.7	0.00	0.0	
6R	13	1945	182.4–192.1	9.7	0.00	0.0	
7R	13	2100	192.1–201.3	9.2	0.00	0.0	
8R	13	2220	201.3–210.9	9.6	0.00	0.0	
9R	13	2335	210.9–220.6	9.7	0.25	2.6	upper Pliocene
10R	14	0040	220.6–230.2	9.6	0.02	0.2	Barren
11R	14	0140	230.2–239.9	9.7	0.45	4.6	upper Pliocene
12R	14	0235	239.9–249.5	9.6	0.25	2.6	upper Pliocene
13R	14	0340	249.5–259.2	9.7	0.48	5.0	upper Pliocene
Coring totals				115.2	1.51	1.3	
Washing totals				144.0	2.12		
Combined totals				259.2	3.63		

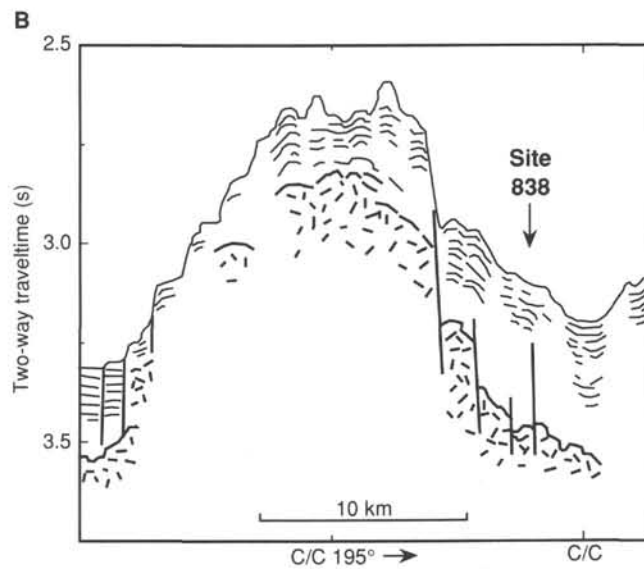
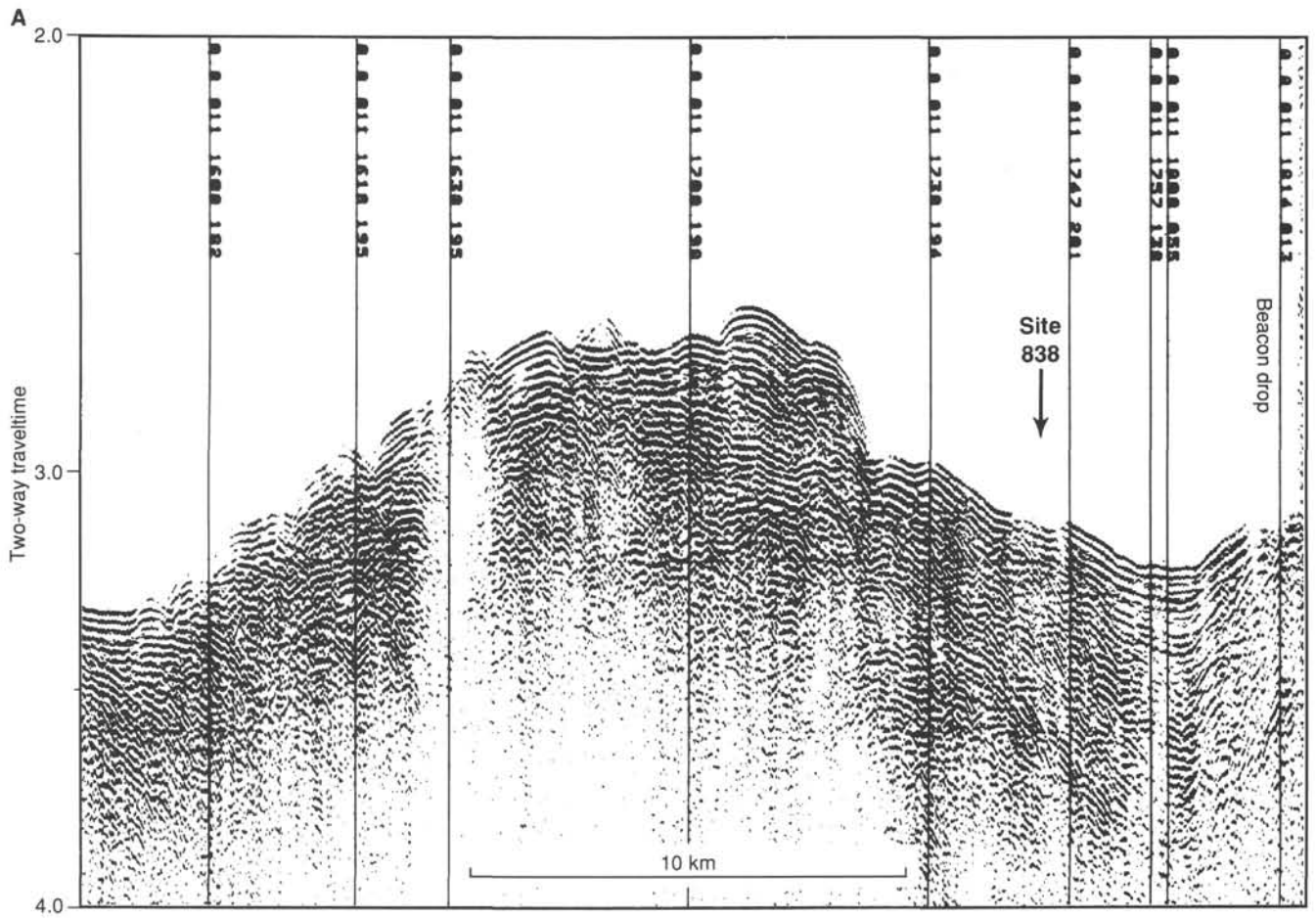


Figure 6. Seismic data for Site 838. **A.** Single-channel seismic reflection profile across Site 838, recorded by the *JOIDES Resolution*. **B.** Line drawing interpretation of Figure 6A. No differentiation has been made between seismic Units A and B in Figures 6A and 6B. **C.** Seismostratigraphic interpretation of Site 838 drilling results.

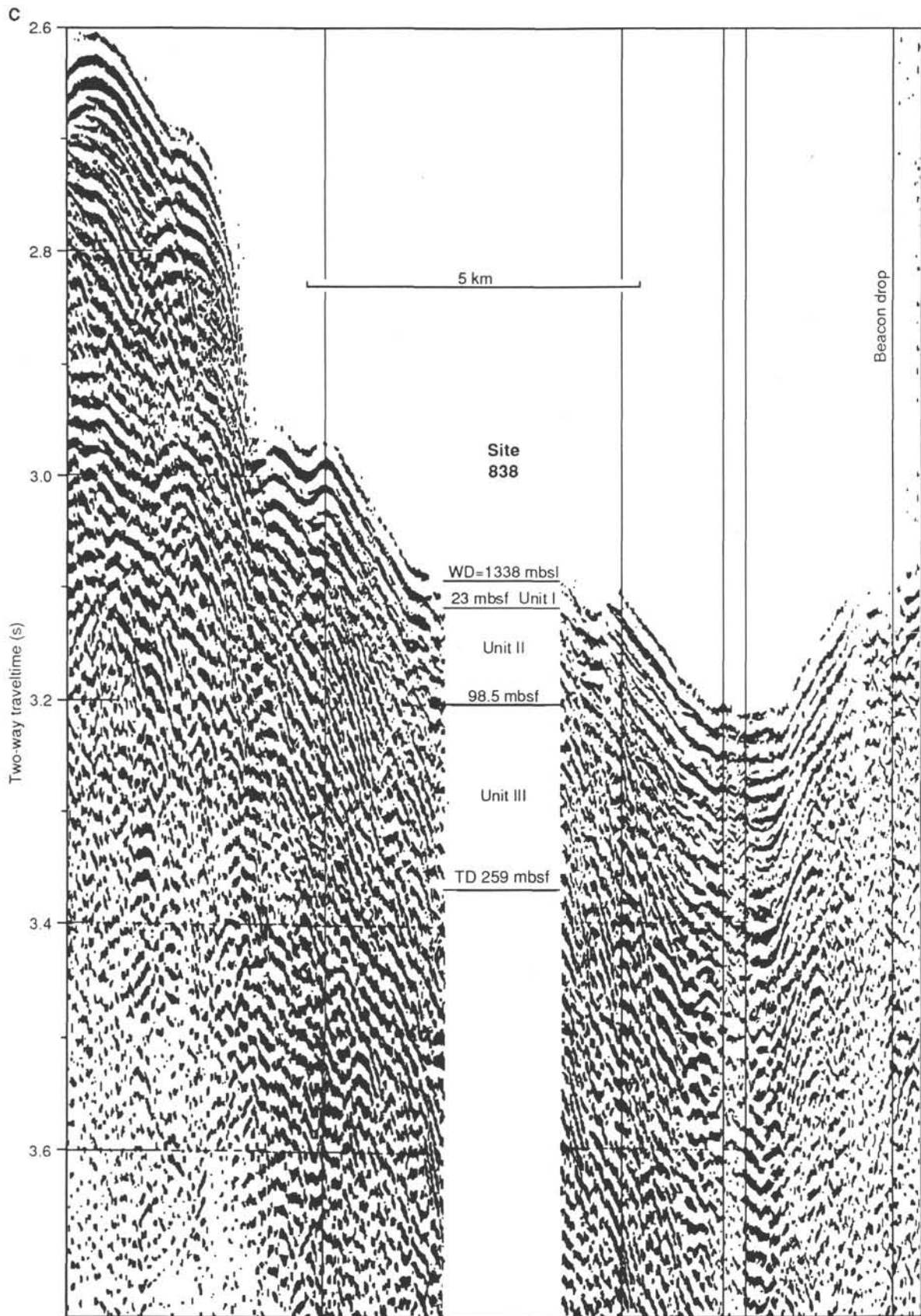


Figure 6 (continued).

Coring continued with the XCB from 98.7 to 152.1 mbsf (Cores 135-838A-12X to -19X). A length of 53.4 m was cored, with 1.46 m recovered (2.73% recovery) in volcanic sands and gravels with basalt fragments and pumice. After no recovery in Cores 135-838A-18X and -19X, a final APC core was taken. Core 135-838A-20H was taken between 152.1 and 153.8 mbsf, with 1.7 m cored and 1.68 m recovered. The core was only a partial stroke and the core liner collapsed, so coring was terminated in favor of the RCB system.

Hole 838B

The ship was moved 20 m south to 20°49.629'S, 176°53.402'W, and Hole 838B was spudded with a 9 $\frac{7}{8}$ -in. BHA and RCB bit at 1010 UTC on 13 January 1991. The mudline was estimated at 2333.7 meters below rig floor (mbrf), and no mudline core was taken. The hole was washed from 2333.7 to 2477.8 mbrf (0.0–144.0 mbsf). RCB cores were taken between 144.0 and 259.2 mbsf (Cores 135-838B-1R to -13R), with 115.2 m cored and 1.51 m recovered (1.31% recovery). Coring was terminated because of very poor recovery in a thicker-than-expected sediment section.

Logging Operations

After conditioning the hole for logging with a short trip, the bit was dropped with the mechanical bit release (MBR). The open end of the pipe was pulled to 73.0 mbrf and logs were run as follows:

Run 1: induction/sonic tool string (DIT/SDT). The log found bottom 20 m above the driller's total depth (24.6 m on a second pass) and required 2.33 hr to run.

Run 2: formation microscanner/gamma-ray tool string (FMS/NGTC). The log found bottom 32.6 m above the driller's total depth and required 2.33 hr to run.

Run 3: density/neutron tool string (HLDT/CNTG/NGT/TCC). The log found bottom 35.7 m above the driller's total depth and required 2.25 hr to run.

Run 4: Geochemical tool string (GST/ACT/NGT/CNT/TCC). The log found bottom 35.7 m above the driller's total depth and required 4.17 hr to run.

Log quality was hampered by enlargement of the hole to 15 in. in unstable, sloughing volcanoclastic silt, sand, and gravel. The hole was left full of seawater and the MBR cleared the seafloor at 0240 UTC on 15 January 1991. The *JOIDES Resolution* left Site 838 for the transit to Site 839 at 0615 UTC on 15 January 1991.

LITHOSTRATIGRAPHY

The sedimentary sequence recovered at Site 838 consists of 103.2 m of volcanoclastic sediments and clayey nannofossil oozes ranging in age from the middle Pleistocene to the upper Pliocene (see "Biostratigraphy" section, this chapter). Two holes were drilled at Site 838 (Table 1; see "Operations" section, this chapter); neither hole reached igneous basement. Of the 103.2 m sedimentary sequence recovered in Hole 838A, 98.7 m was cored by APC, 1.46 m of lithified sediments were recovered by XCB between 98.7 and 152.1 mbsf, and an additional 1.68 m of volcanoclastic sediments were recovered by APC from 152.1 to 153.8 mbsf. Hole 838B was drilled entirely by RCB with a total recovery of 1.36 m of lithified sediments between 144.0 and 259.2 mbsf. For cores with poor recovery, the stratigraphic position of the sediment within each core is unknown. The sediment cores were described and sampled for smear slide description, refractive

index of glasses, and X-ray fluorescence (XRF) and carbonate analysis.

The lithostratigraphic summary (Fig. 7) is based on Hole 838A. Table 2 summarizes the sediment lithologies recovered in Hole 838B. The sedimentary sequence at Site 838 was divided into three lithologic units (Fig. 7), based on differences in sedimentary texture, structure, and composition, and on the varying abundance of volcanoclastic deposits. Unit I is dominated by clayey nannofossil ooze with sporadic interbeds of vitric sand and vitric fine ash with foraminifers. Unit II comprises a sequence dominated by vitric sands and volcanic gravels, with minor interbeds of clayey nannofossil ooze. Unit II is subdivided into five subunits that define distinct phases of sedimentation (Fig. 7). Unit III comprises volcanic gravel and vitric sand, volcanic conglomerate, vitric sandstone, and vitric clayey siltstone (Table 2). The lithologic significance of this unit is poorly known because of the recovery of only thin sequences of lithified sediments.

Unit I

Interval: Sections 135-838A-1H-1 through -4H-1

Depth: 0–23.04 mbsf

Unit I is 23.04 m thick and is composed of homogeneous and generally structureless iron-oxyhydroxide-stained clayey nannofossil oozes, with four volcanoclastic interbeds. The age of Unit I, based on biostratigraphic and paleomagnetic data, is early to middle Pleistocene (0.02–1.44 Ma) with an average sedimentation rate of 21 mm/k.y. (see "Sedimentation Rates" section, this chapter).

Clayey Nannofossil Ooze

The clayey nannofossil ooze is composed mainly of calcareous nannofossils (47–52 vol%), clay (40–45 vol%), and planktonic foraminifer tests and test debris (up to 8 vol%). The ooze is generally homogeneous, although clasts of altered pumice (up to 2 cm across) and mottled intervals, caused by bioturbation, occur. The clayey nannofossil ooze contains an average of 55%–60% CaCO₃ (Fig. 8). This increases downward through the unit. The clayey nannofossil ooze is stained dark brown to very dark grayish brown because of the presence of iron-oxyhydroxides.

Volcanoclastic Interbeds

Volcanoclastic sediments are a minor component of Unit I and consist of a mixture of epiclastic and pyroclastic material (see "Volcanoclastic Sediments" section, below). Four very thin to thick bedded volcanoclastic interbeds occur within Unit I:

1. A diffuse, 2 cm-thick layer of bioturbated vitric clayey nannofossil mixed sediment, containing minor amounts of augite and plagioclase, occurs at 8.16–8.18 mbsf (Section 135-838A-2H-3, 146–148 cm). This is interpreted as a pyroclastic deposit.
2. A 51-cm-thick, normally graded vitric sand with foraminifers occurs between 15.79 and 16.3 mbsf (Sections 135-838A-3H-2, 109 cm, through -3H-3, 10 cm). The sand is planar laminated and contains pumice clasts up to 3 cm in diameter. It has a sharp basal contact and grades upward into clayey nannofossil ooze. The occurrence of a foraminifer-rich basal layer suggests that this bed is not a primary pyroclastic deposit.
3. A thin, normally graded vitric sand with foraminifers occurs at 19.22–19.28 mbsf (Section 135-838A-3H-5, 2–8 cm). It has an eroded basal contact and is interpreted as a distal turbidite.
4. A 2-mm-thick layer of vitric clayey nannofossil mixed sediment occurs at 22.6 mbsf (Section 135-838A-3H-7, 40 cm). This layer has a sharp basal contact and is interpreted as a pyroclastic deposit.

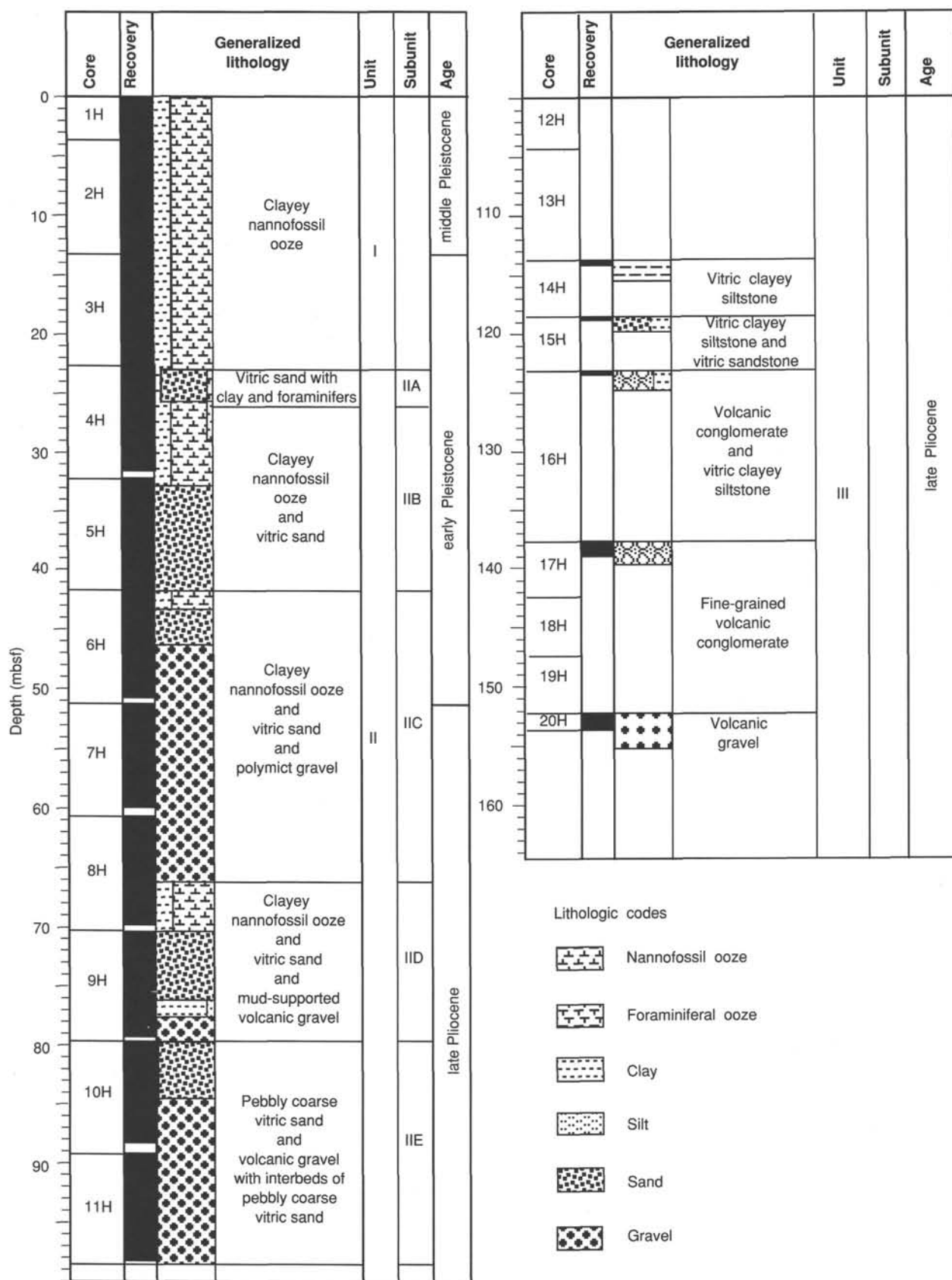


Figure 7. Lithologic summary for Hole 838A, indicating the main lithologic units identified with age as well as a generalized graphic lithology.

Table 2. Summary of sediments recovered in Unit III (Hole 838B).

Core, section, interval (cm)	Recovery (m)	Depth (mbsf)	Generalized lithology	Unit	Age
135-838B-					
9R-CC, 0-25	0.25	210.9-220.6	Vitric clayey siltstone	III	upper Pliocene
10R-1, 0-4	0.02	220.6-230.2	Vitric clayey siltstone	III	Barren
11R-1, 0-42	0.45	230.2-239.9	Vitric clayey siltstone	III	upper Pliocene
12R-1, 0-21	0.25	239.9-249.5	Vitric clayey siltstone	III	upper Pliocene
13R-1, 0-44	0.48	249.5-259.2	Vitric clayey siltstone	III	upper Pliocene

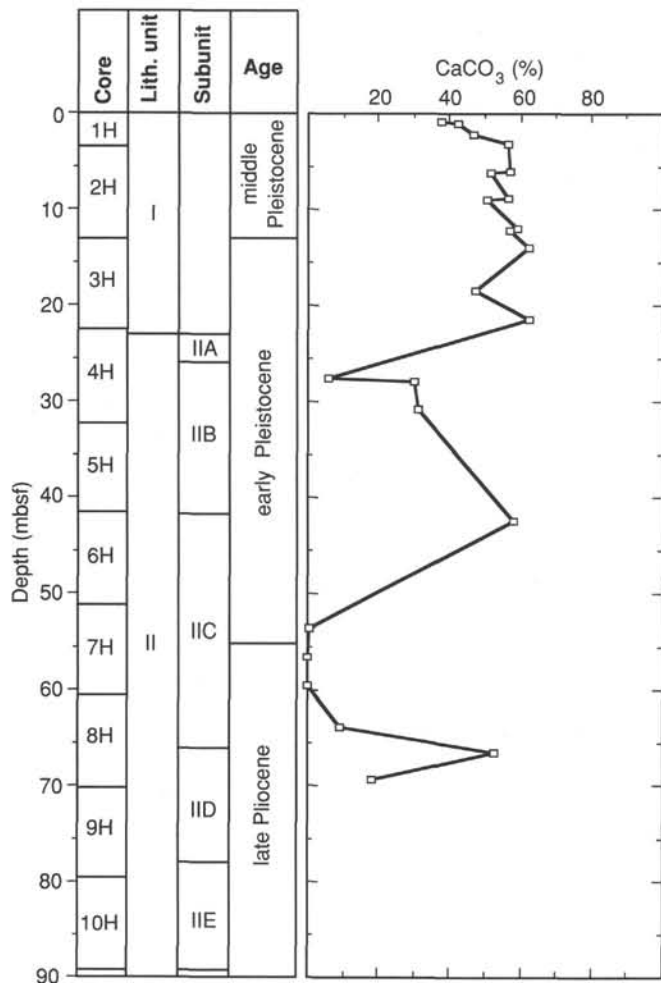


Figure 8. Downcore CaCO₃ profile for the sediment column cored in Hole 838A. The lithologic log has been included for correlation.

Unit II

Interval: Cores 135-838A-4H through -11H
 Depth: 23.04-98.7 mbsf

Unit II is distinguished from Unit I by the predominance of thin to thick-bedded epiclastic volcanic sediments. Some of these volcanoclastic sediments are interpreted as turbidites on the basis of their grain-size characteristics and sedimentary structures; others probably represent debris flows. The turbidites, most commonly found in the upper parts of Unit II, show normal grading with coarse-grained bases and eroded basal contacts. The cohesive debris-flow deposits dominate the lower part of Unit II and generally comprise ungraded, coarse vitric sands and gravels. A detailed description of these epiclastic deposits is given in the

“Volcanoclastic Sediments” section below. Unit II is divided into five subunits, each representing distinct phases of sedimentation. The volcanoclastic deposits within each subunit are separated from those in adjacent subunits by thin intervals of clayey nannofossil ooze. The volcanoclastic sediments of Unit II generally have a CaCO₃ content of up to 5%, whereas the clayey nannofossil oozes contain up to 60% CaCO₃ (Fig. 8). The age of Unit II ranges from late Pliocene to early Pleistocene (1.4-1.9 Ma). The average sedimentation rate is about 47 mm/k.y. between 23.04 and 55 mbsf and 177 mm/k.y. between 55 and 98.7 mbsf (see “Sedimentation Rates” section, this chapter).

Subunit IIA

Interval: Sections 135-838A-4H-1 through -4H-3
 Depth: 23.04-26.77 mbsf

Subunit IIA is 3.8 m thick and consists of two vitric sand intervals. The uppermost vitric sand (23.04-25.09 mbsf; Sections 135-838A-4H-2, 89 cm, through -4H-1, 34 cm) is light brownish gray and normally graded. It is structureless but has a sharp basal contact and a gradational upper contact with the clayey nannofossil ooze of Unit I. Smear slide analysis shows that the sand comprises volcanic glass (80 vol%) with minor amounts of clay (about 10 vol%) and planktonic foraminifer tests and test debris (10 vol%). The lower vitric sand (25.09-26.77 mbsf; Sections 135-838A-4H-2, 89 cm, through -4H-3, 107 cm) is grayish brown and comprises about 95 vol% volcanic glass with minor amounts of accessory minerals (5 vol%). The sand is ungraded and has a sharp basal contact (Fig. 9). The clayey nannofossil ooze below this contact shows a marked color change from yellowish brown to dark brown 8 cm beneath the base of the overlying vitric sand unit (Fig. 9). The color change is interpreted as a redox-related chemical front, possibly caused by fluid migration through the overlying, permeable vitric sand.

Subunit IIB

Interval: Sections 135-838A-4H-3 through -6H-1
 Depth: 26.77-41.82 mbsf

Subunit IIB consists of iron-oxyhydroxide-stained, clayey nannofossil ooze containing thin to thick interbeds of dark brown to black vitric sands (26.77-32.9 mbsf), overlying very dark gray to black, structureless vitric sand (32.9-41.82 mbsf). The clayey nannofossil ooze is dark brown to brown and appears devoid of sedimentary structures. There are, however, rare pumice clasts and minor mottling immediately above the gradational contact with the underlying vitric sands. The black vitric sand interbeds within the clayey nannofossil ooze are typically 2-10 cm in thickness, although a 50-cm-thick, black vitric sand bed occurs between 28.92 and 29.42 mbsf. They all show sharp, scoured bases and pronounced fining upward into clayey nannofossil ooze.

The lower part of Subunit IIB (32.9-41.82 mbsf) consists of two black to very dark gray, normally graded vitric sand beds (32.9-38.09 and 38.27-41.82 mbsf) separated by 18 cm of iron-oxyhydroxide-stained nannofossil ooze. Within the upper bed

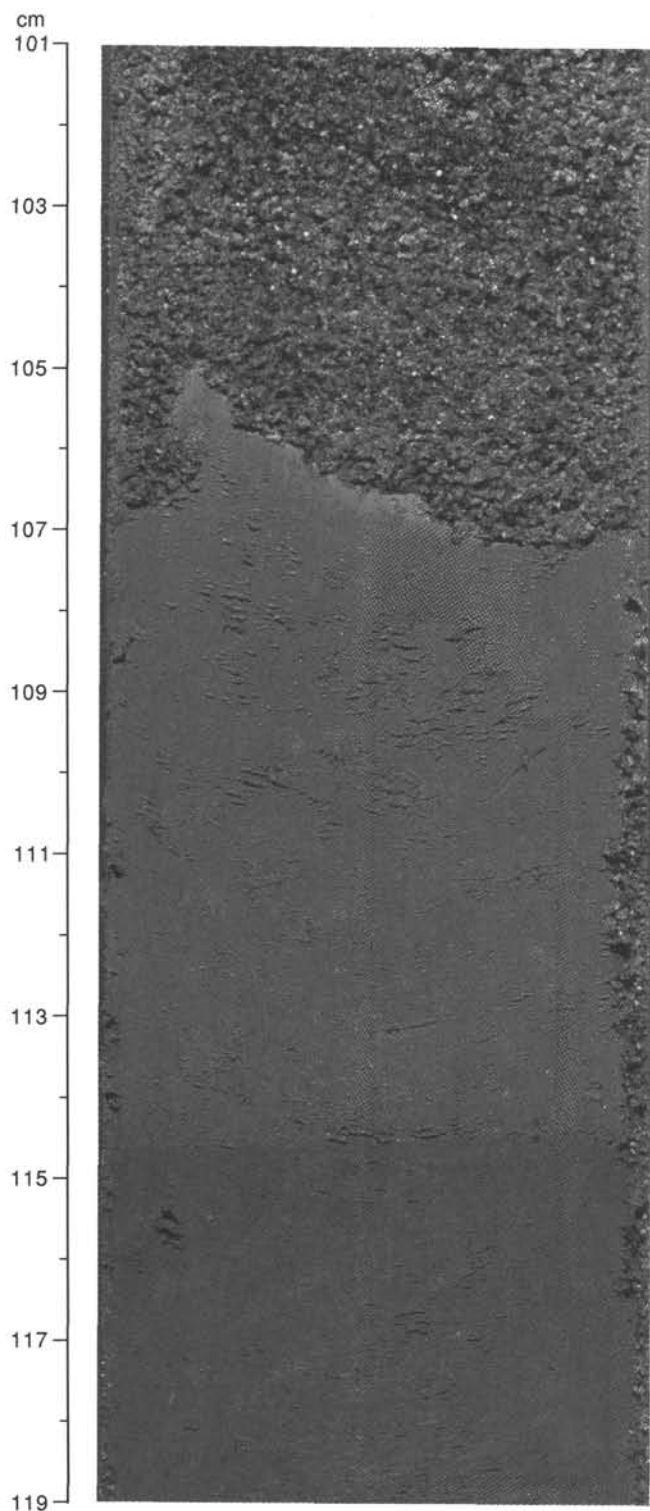


Figure 9. Eroded basal contact of lower vitric sand bed in Subunit IIA, at Section 135-838A-4H-3, 107 cm (26.77 mbsf). Note downsection darkening of the underlying clayey nannofossil ooze at 115 cm; this corresponds to a color change from yellowish brown to dark brown, which is interpreted as a redox-related chemical front.

there are scattered mudclasts up to 4 cm in diameter. The vitric sand is composed of up to 90 vol% glass shards with minor amounts of foraminifers (5 vol%) and accessory minerals (5 vol%).

Subunit IIC

Interval: Sections 135-838A-6H-1 through -8H-4
Depth: 41.82–66.27 mbsf

Subunit IIC is 24.48 m thick and consists of a sequence of very thick-bedded, very poorly sorted polymict gravel (46.2–66.3 mbsf) that grades upward into very thick-bedded vitric sandy gravel (43.2–46.17 mbsf). This is overlain by 1.4 m of brown iron-oxyhydroxide-stained, structureless clayey nannofossil ooze (41.8–46.2 mbsf).

The polymict gravel forms a 20.1-m-thick continuous sequence extending from the base of Subunit IIC and contains angular to rounded clasts of altered and fresh pumice, mafic volcanic rock, and light brown to reddish brown indurated mudclasts up to 15 cm in diameter. The gravels show an overall upward fining, although intervals of reverse grading occur. Large clasts appear scattered throughout the sediments. The polymict gravel grades upward into a light brownish gray, normally graded, 3.0-m-thick vitric sandy gravel with abundant rounded gravel-sized pumice clasts. Larger isolated pumice clasts up to 4 cm across also occur (Fig. 10). The matrix consists of 90 vol% volcanic glass, 7 vol% clay-sized material, and 3 vol% calcareous nannofossils.

Subunit IID

Interval: Sections 135-838A-8H-4 through -9H-6
Depth: 66.27–79.7 mbsf

Subunit IID is 13.4 m thick and consists of a sequence of volcanic gravels and coarse-grained vitric sands (70.2–79.7 mbsf) overlain by clayey nannofossil ooze (66.27–70.2 mbsf).

A dark yellowish brown to black, 1.2-m-thick, mud-supported volcanic gravel, at 77.7–78.9 mbsf, forms the basal bed of the subunit (between 78.9 and 79.7 mbsf, the same lithology was recovered in the core catcher). The gravel shows an overall upward fining trend, with the maximum clast size decreasing from 3 cm at the base to 0.5 cm near the top of bed. Clasts consist mainly of pumice and clayey nannofossil ooze, although isolated larger clasts of crystal-rich tuff also occur. The mud-supported gravel is overlain by 1.6 m of dark reddish brown, iron-oxyhydroxide-stained clay. Smear slide analysis shows that this comprises about 85 vol% clay-sized material and minor amounts of feldspar (10 vol%) and accessory minerals (5 vol%). Within the clay there are pebbly intervals. The uppermost 14 cm is mottled and yellowish red in color.

The clay is overlain by a 5.22-m-thick sequence of fine- to coarse-grained vitric sands, sandy clays, and rare clay bands (70.91–76.13 mbsf). Two beds of black vitric sand occur at the base of this sequence. They are 20 and 23 cm thick respectively and are separated by a 20-cm-thick band of olive brown sandy clay. The upper sand bed contains diffuse laminae of altered silicic ash. These beds are overlain by 4.54 m of poorly sorted, fine- to very coarse-grained vitric sand containing a polymict assemblage of greenish-brown and reddish brown, isolated clasts of altered pumice and basalt pebbles (up to 10 cm in diameter), with less frequent mudstones and claystones (Fig. 11). Grain mounts show that the sand consists of 85 vol% glass shards of basaltic andesite composition and minor amounts of angular, anhedral to subhedral feldspar (5 vol%) and up to 10 vol% accessory minerals, mainly orthopyroxene (see "Volcaniclastic Sediments" section, below). Overlying this sand, from 70.91 through 70.2 mbsf, there is a sequence of dark reddish brown clay (23 cm thick), overlain by black fine vitric sand (14 cm thick),

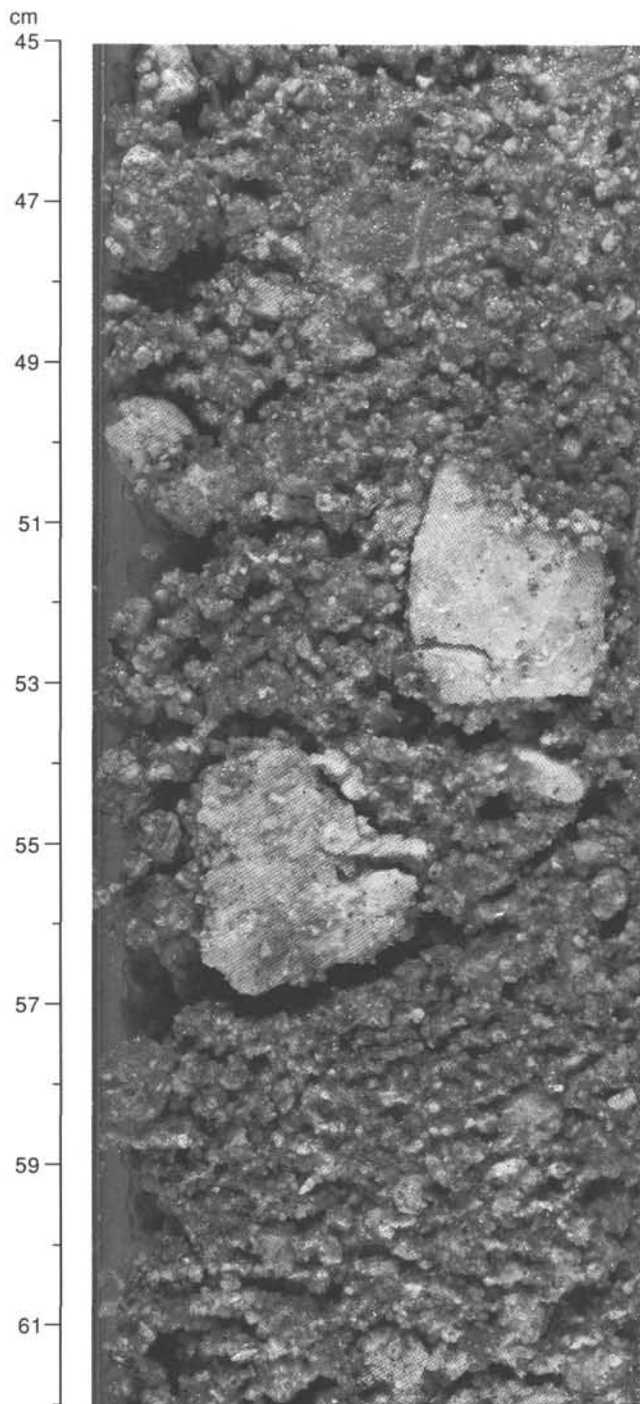


Figure 10. Large isolated pumice clasts in matrix-supported volcanic gravel of Subunit IIC, Section 135-838A-7H-4, 45–62 cm (56.15–56.32 mbsf). Matrix consists of 90% volcanic glass, with minor amounts of clay-size material and calcareous nannofossils.

dark brown to black clay (17 cm thick), and dark brown to black mud-supported gravel containing subangular mafic clasts (17 cm thick). These beds are overlain by a 3.9-m-thick sequence of brown, clayey nannofossil oozes. The oozes consist of about 30 vol% clay and up to 60 vol% calcareous nannofossils. Pale brown volcanic glass (about 7 vol%) and foraminifers (up to 3 vol%) occur in minor quantities. The oozes appear to be homogeneous, except for slight mottling attributed to bioturbation, and sporadic

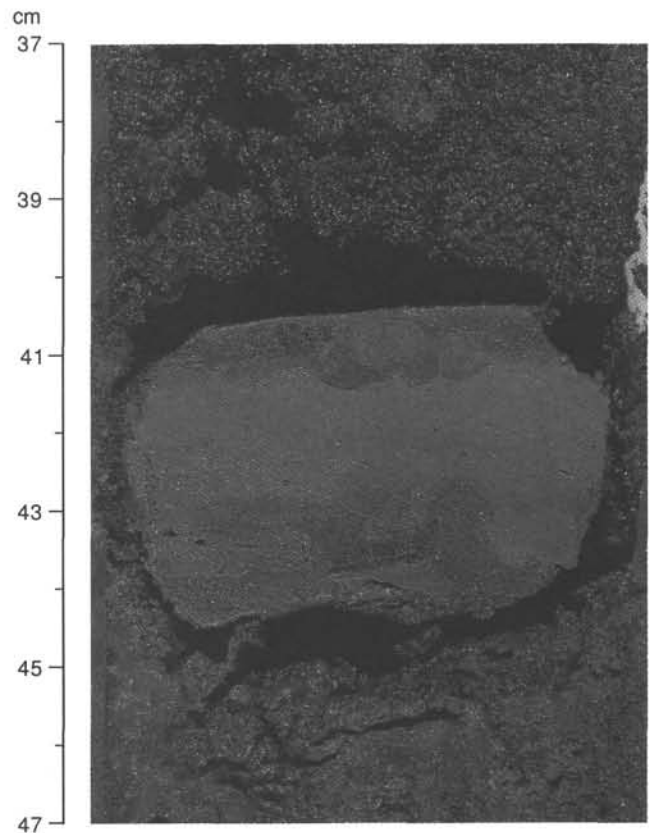


Figure 11. Indurated pelagic interval and base of a vitric sand turbidite in Subunit IID, Section 135-838A-9H-4, 37–47 cm (75.07–75.17 mbsf). Note the scoured basal contact of the vitric sand.

pumice and mud clasts (up to 5 cm across). The clayey nannofossil oozes contain up to 53% CaCO_3 . A 27-cm-thick bed, interpreted as a turbidite, occurs within the clayey nannofossil oozes between 68.77 and 69.04 mbsf (Fig. 12). The lowermost 10 cm of the sequence consists of very angular to subrounded volcanic gravel which shows reverse grading and a scoured basal contact. The gravel is composed predominantly of pumice clasts, with lesser amounts of basaltic material. The remaining 17 cm comprises a fining upward, well-sorted, planar laminated layer of vitric sand and vitric silt grading into clayey nannofossil ooze.

Subunit IIE

Interval: Sections 135-838A-10H-1 through -11H-CC

Depth: 79.7–98.7 mbsf

Subunit IIE is 19 m thick and consists of a thin (79.7–79.92 mbsf) vitric clayey silt overlying a graded sequence of pebbly, coarse-grained vitric sand (79.92–84.37 mbsf), which in turn overlies a vitric sandy gravel (84.37–98.7 mbsf). The unit shows an overall fining-upward trend, although internally the beds are generally structureless.

A dark gray, poorly sorted gravel, containing pumice and fragments of hyaloclastite (see “Volcaniclastic Sediments” section, below), forms the basal part of Subunit IIE between 96.05 and 98.7 mbsf. The sequence is strongly affected by drilling disturbance and appears structureless. Individual gravel clasts are angular to subrounded and show no preferred orientation. The upper part of this gravel fines upward into a 85-cm-thick sequence (95.2–96.05 mbsf) of very coarse sand containing a 25-cm-thick gravel interbed which comprises pumice and fragments of hyaloclastite.

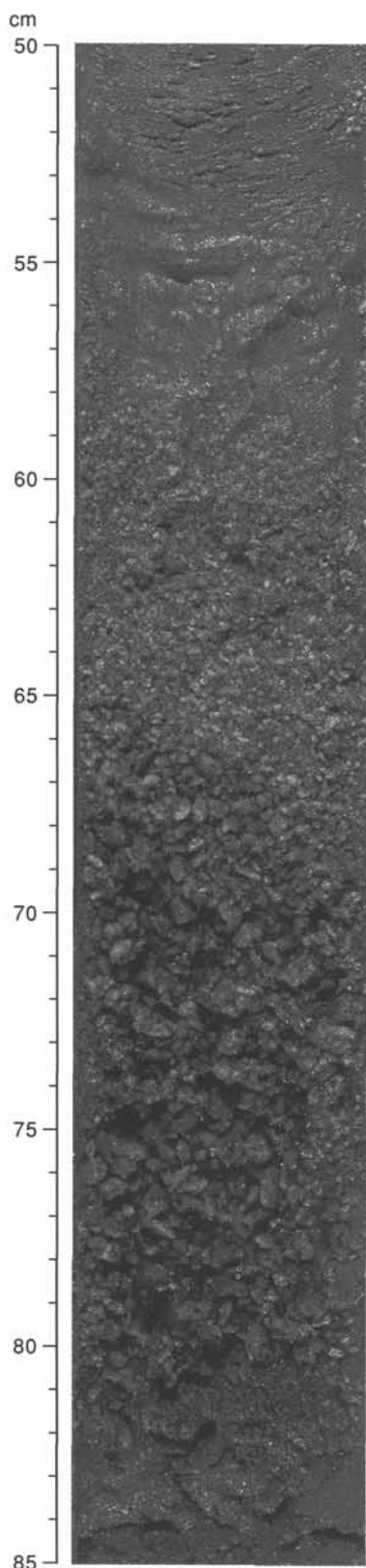


Figure 12. Thin graded bed of angular gravel, interpreted as a turbidite, in Subunit IID, Section 135-838A-8H-6, 50–85 cm (68.70–69.05 mbsf). Note the reverse grading, immediately above the base of the bed, reaching a maximum grain size at 69–77 cm, beneath normal grading from 58 to 69 cm.

A 10.83-m-thick interval of gray to dark gray, poorly sorted, vitric sandy gravel overlies the coarse-grained sands, between 84.37 and 95.2 mbsf (Sections 135-838A-10H-4, 17 cm, through -11H-4, 150 cm). Sedimentary structures are rare, and the vitric sandy gravel shows no discernible grading, although there are slightly finer-grained intervals within the sequence in Sections 135-838A-10H-6, 0–13 cm, -10H-5, 68–113 cm, and -10H-4, 73–95 cm. Individual gravel clasts, which mainly consist of angular to rounded pumice, are up to 1 cm across and are generally held in a finer grained matrix, the grains of which measure up to 0.5 cm in diameter. The matrix consists of 95 vol% volcanic glass with small amounts of clay, feldspar, accessory minerals and foraminifers (5 vol%). Toward the base of the bed, vitric sand is mixed with abundant pumice granules and scattered, angular to rounded pumice clasts up to 6 cm in diameter. The pumice clasts show random size variation throughout the bed. However, the gravel-sized material within this sequence shows normal grading.

This vitric sandy gravel is overlain by 4.5 m of olive gray, poorly sorted pebbly coarse vitric sand (Sections 135-838A-10H-1, 0 cm, through -10H-4, 17 cm [79.92–84.37 mbsf]). The sequence shows an overall upward-fining trend. Bedding planes can be observed within individual beds, which vary in thickness from 1 to 15 cm.

Unit III

Interval: Cores 135-838A-12X through -19X and -20H and
Cores 135-838B-1R through -13R
Depth: 98.7–153.8 and 0.0–259.2 mbsf

Unit III consists of sediments and sedimentary rocks recovered from 98.7 to 259.2 mbsf in Holes 838A and 838B. The stratigraphic control is poor on account of the low recovery (2.8%). Four lithologies occur: volcanic gravel interbedded with very coarse-grained granular vitric sand, volcanic conglomerate, vitric sandstone, and vitric clayey siltstone.

Volcanic Gravel and Very Coarse-grained Granular Vitric Sand

Black volcanic gravel occurs in Sections 135-838A-20H-1 through -20H-CC (152.1–153.8 mbsf), with an intervening very coarse-grained, granular, dark gray, structureless vitric sand at 153.32–153.62 mbsf.

The 1.22-m-thick volcanic gravel is composed predominantly of moderately to well-sorted, angular to well-rounded granules and pebbles of basalt (up to 90 vol%), with minor amounts of pumice, angular black glass fragments, calcareous vitric siltstones, and siltstone. The gravel overlying the sand (Section 135-838A-20H-1) has a sharp basal contact, and shows a fining-upward trend, with the maximum clast size decreasing from 3 cm in the basal part to <0.5 cm toward the top of the bed. The coarsest volcanic gravel is found in the core catcher, with clasts up to 4 cm in diameter.

The lithologies described here are similar to those found in Subunit IIE and represent the only unlithified sediments recovered below 98.7 mbsf. Such unlithified gravels and sand have proved difficult to recover using RCB and XCB coring techniques (Core 135-838A-20H was cored with the APC), and it is possible that much of the sedimentary section below 98.7 mbsf comprises this type of coarse, unconsolidated sediment.

Volcanic Conglomerate

Volcanic conglomerate was recovered in Sections 135-838A-16X-1 through -17X-CC (123.1–142.4 mbsf). This bed consists of indurated, olive brown, grain-supported, fine gravel with individual basalt clasts up to 1 cm in diameter and reaches 63 cm in thickness. In Core 135-838A-17X, thin layers of medium- to coarse-grained vitric sandstone occur within the conglomerate. In

Core 135-838A-16X, a 4-cm-thick layer of dark olive, vitric clayey siltstone with thin planar laminae occurs within the conglomerate. The bed shows a sharp basal contact with an underlying vitric clayey siltstone.

Vitric Sandstone

Interval: Core 135-838A-15X, 0–9 and 16–32 cm

Between Section 135-838A-15X, 0–9 cm, the vitric sandstone is medium-grained and shows faint, planar lamination. In Section 135-838A-15X, 16–32 cm, the vitric sandstone is massive, very coarse-grained and granular. Both intervals are olive brown in color and are separated by a 7-cm-thick vitric clayey siltstone.

Vitric Clayey Siltstone

Interval: Cores 135-838A-14X, -15X, and -16X; Cores 135-838B-9R, -10R, -11R, 12R, and -13R

Sedimentary structures found in the vitric clayey siltstones include both thick and thin planar lamination, ripple cross-lamination, load casts, normal grading, and mottling caused by bioturbation. However, massive and structureless intervals also occur. The beds show a wide variety of colors, including black, dark olive, olive brown, light olive gray, light olive green and greenish gray. Black dendrites, probably of manganese oxide, occur in Section 135-838A-16X-1, 67 cm.

Volcaniclastic Sediments

Units I and II

In Hole 838, volcaniclastic sediments constitute about 65% of the recovered sedimentary sequence (Table 3) and 80–90 vol% volcanic material. All volcaniclastic sediments are of epiclastic origin, with the exception of two inferred pyroclastic layers 2 cm and <1 cm thick that occur in Unit I at 8.18 mbsf and 22.6 mbsf, respectively.

Within the epiclastic deposits four major types are distinguished: (1) vitric turbidites, (2) thin turbidites with vitric-rich bases, (3) pumiceous gravels, and (4) proximal reworked (slump)-facies.

Vitric Turbidites

Normally graded vitric turbidites occur in the upper part of Hole 838 in Unit I and Subunits IIA and IIB (Sections 135-838A-3H-2, -3H-5, -4H-1, -4H-3, and -4H-5). Most silicic turbidites contain abundant colorless, clear shards comprising varying proportions of angular, conjugate shards, fibrous pumiceous shards and pumiceous shards with tubular vesicles. Maximum grain-sizes are typically about 1 mm. Individual turbidites range in thicknesses from 6 cm to 3.55 m. Refractive index studies (for analytical procedures see "Lithostratigraphy" sections, "Site 834" and "Site 835" chapters) show that most shards are rhyodacite in composition with SiO₂ concentrations of around 70 wt% (Fig. 13

Table 3. Characteristics of ash layers, ash turbidites, and volcanic gravels in Hole 838A.

Core, section, depth	Depth to top (mbsf)	Depth to base (mbsf)	Smear slide	Interval thickness (cm)	Type of unit	Description
135-838A-						
2H-3, 148	8.16	8.18	X	2	P, H	Primary tephra
3H-2, 130	15.79	16.30	X	51	E, G	Vitric turbidite
*3H-5	19.22	19.28		6	E, G	Vitric turbidite
3H-7, 40	22.60	22.60	X	<1	P, G	Primary tephra
4H-1, 100	23.04	25.09	X	205	E, G	Vitric turbidite
4H-3, 80	25.09	26.77	X	168	E, G	Vitric turbidite
4H-4, 35	27.47	27.56	X	9	E, G	Turbidite with vitric-rich base
*4H-4	27.84	27.85		1	E, G	Turbidite with vitric-rich base
*4H-4	27.85	27.87		2	E, G	Turbidite with vitric-rich base
*4H-4	27.89	27.89		2	E, G	Turbidite with vitric-rich base
*4H-4	28.18	28.22		4	E, G	Turbidite with vitric-rich base
*4H-5	28.76	28.84		8	E, G	Turbidite with vitric-rich base
*4H-5	28.84	28.89		5	E, G	Turbidite with vitric-rich base
*4H-5	28.89	28.92		3	E, G	Turbidite with vitric-rich base
4H-5, 60	28.92	29.42	X	50	E, G	Vitric turbidite
*4H-6	30.34	30.35		1	E, G	Turbidite with vitric-rich base
4H-6, 74	30.90	30.95	X	5	E, G	Turbidite with vitric-rich base
5H-1, 110	32.90	38.09	X	519	E, G	Mafic vitric turbidite
5H-5, 100	38.27	41.82	X	355	E, H	Mafic vitric turbidite
6H-2 to *6H-7	43.20	50.84		764	E, G	Pumiceous vitric grain-flow
7H-1 to 8H-2	51.20	63.62	2	1242	E, G	Pumiceous vitric grain-flow
8H-3 to *8H-4	63.99	66.27		228	E, G	Proximal reworked
*8H-6	68.77	69.04		27	E, G	Vitric ash turbidite
*9H-1	70.20	70.37		17	E, H	Proximal reworked
*9H-1	70.54	70.68		14	E, H	Mafic grain-flow(?)
9H-1 to 9H-4	70.91	75.45	2	454	E, H	Mafic vitric turbidite (top reworked?)
*9H-4	75.50	75.70		20	E, H	Proximal reworked?
*9H-4	75.90	76.13		23	E, H	Proximal reworked
9H-6, 110	77.70	78.90	X	120	E, H	Proximal reworked
10H-1, 10	79.70	79.92	X	22	E, H	Proximal reworked
10H-1 to *11H-6	79.92	97.92		1800	E, H	Pumiceous vitric grain-flow

Notes: Core, section, depth to smear slide sample (cm); an asterisk (*) indicates ash layer from which no smear slide was made, and only the core and section in which the ash layer occurs are indicated. Type: P = pyroclastic, E = epiclastic, H = homogeneous, and G = graded. Glass (vol%): Glass content normally indicates maximum mode estimated from smear slides; however, glass content may be highly variable in individual units, especially in the graded sequences.

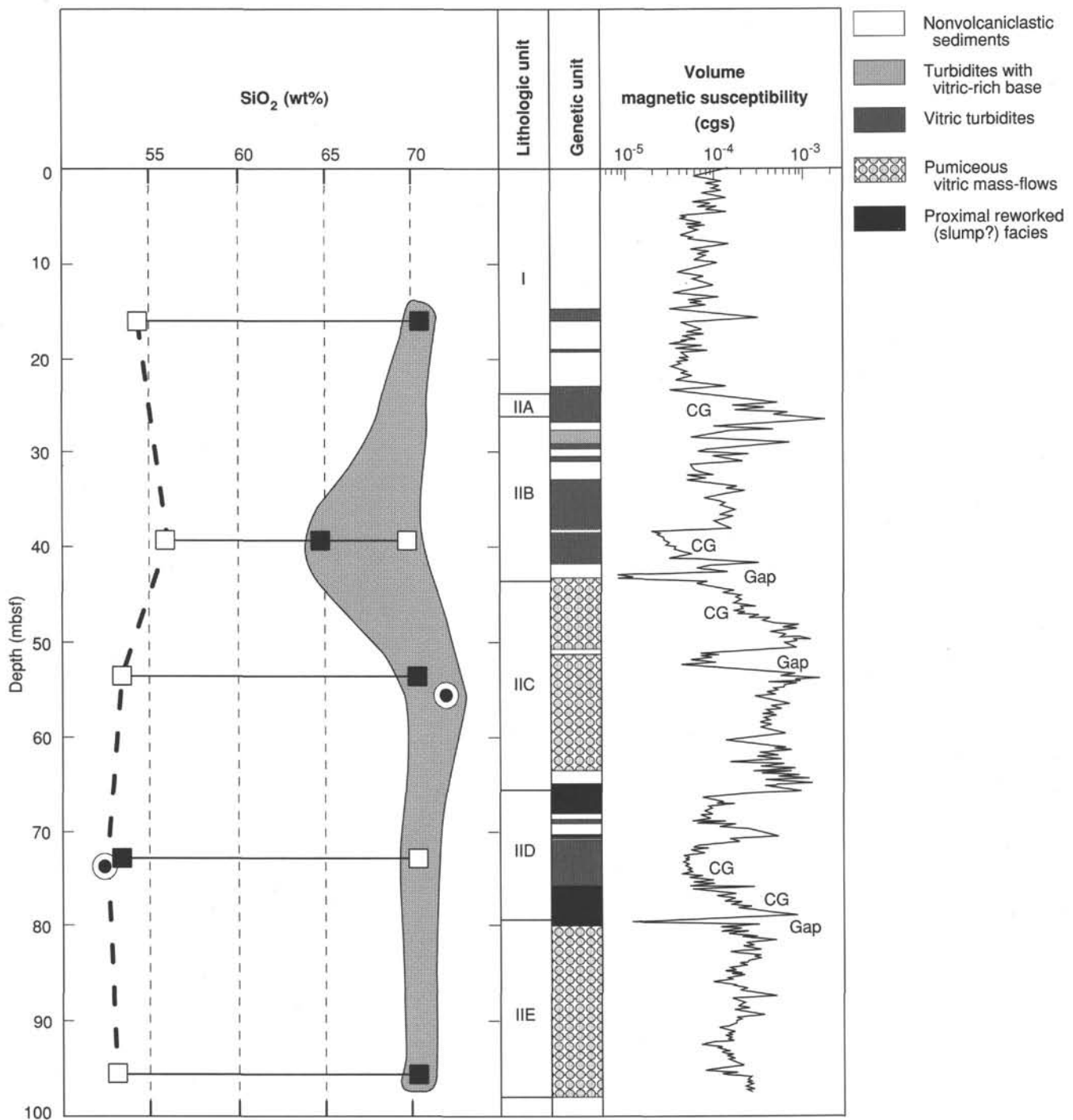


Figure 13. Plot showing the variation in silica content of glass shards and the sediment volume magnetic susceptibility vs. depth, Hole 838A. Filled squares = major glass groups and open squares = minor glass groups. Dots within open circles = X-ray fluorescence (XRF) analyses of major glass groups. The enclosed shaded region represents the downcore range of composition in the high silica field, and the dashed line represents the downcore trend of the low silica field. Note the strongly bimodal chemistry.

and Table 4). In Subunit IIB (Sections 135-838A-5H-5 to -5H-7) a 3.55-m-thick vitric turbidite is composed mainly of medium brown, angular and nonvesicular glass shards of dacite composition (66 wt% SiO_2). Colorless, clear fibrous shards and pumiceous shards of rhyodacite composition (70 wt% SiO_2) with tubular vesicles, and deep brown andesite shards (56 wt% SiO_2) are minor constituents in this turbidite. The silicic composition of this bed

is confirmed by the overall low magnetic susceptibility (Fig. 13), reflecting the small proportion of ferromagnesian minerals present. A systematic increase in magnetic susceptibility downward through this turbidite may, however, indicate compositional grading, with increasing amounts of ferromagnesian minerals toward the base. In the other more silicic turbidites, pale brown shards are a minor constituent, normally <5 vol%. Based on a single

Table 4. Refractive indices (*n*) and SiO₂ concentrations (estimated after Church and Johnson [1980] and Schmincke [1981]) of vitric shards (36–63 μm size fraction) from turbidites in Hole 838A.

Core, section, interval (cm)	Depth (mbsf)	Comments	<i>n</i>	SiO ₂ (wt%)
135-838A-				
3H-2, 147	16.17	Clear	1.508	70.5
3H-2, 147	16.17	Brown/green	1.573	54.4
5H-5, 119	39.39	Clear	1.511	69.7
5H-5, 119	39.39	Brown/green	1.529	64.8
5H-5, 119	39.39	Deep brown	1.566	55.9
7H-2, 89	53.59	Clear	1.509	70.3
7H-2, 89	53.59	Brown/green	1.578	53.4
9H-2, 108	72.78	Clear	1.509	70.3
9H-2, 108	72.78	Brown/green	1.578	53.4
11H-5, 30	95.50	Clear	1.509	70.3
11H-5, 30	95.50	Brown/green	1.579	53.2

refractive index determination they are probably mainly basaltic andesite in composition, with SiO₂ concentrations around 54 wt%.

The thickness of these flow deposits and the relatively large maximum diameters of the silicic volcanic shards within them suggest a proximal source for the turbidites, as at Sites 834 and 835. Although the general N-S trending tectonic fabric of the Lau Basin would seem to favor transport of material parallel to this direction, two of the potential sources for the input of silicic volcanic detritus, the Tofua Arc and the Tonga Ridge to the east, are relatively proximal to Site 838. An east-west flow of debris from these sources may thus have occurred. However, a more local source for these turbidites cannot be ruled out.

In Subunit IID (Sections 135-838A-9H-1 to -9H-4), a 4.5-m-thick vitric turbidite consists mainly of glass shards of basaltic andesite composition. Silica concentrations in these shards, estimated from refractive index studies, are 53 wt% SiO₂ and are in agreement with XRF data of 52.1 wt% SiO₂ (Fig. 13). The chemical composition of these glasses (Table 10, "Igneous Petrology" section, this chapter) resembles that of the basaltic andesites recovered from the basement of Hole 836A (see Table 8, "Igneous Petrology" section, "Site 836" chapter), in particular by the slightly enhanced Ba/high-field-strength element ratios and similar SiO₂, MgO, Cr, Ni, CaO, and K₂O concentrations. However, distinctly lower TiO₂, Zr, and Y concentrations indicate a mantle source more depleted in these elements. Shards, ranging in diameter from several millimeters to 100 μm, are mainly light to medium brown in color and are dominated by blocky, angular to subangular shapes (Fig. 14). Vesicularity is generally <10 vol%. Large euhedral to subhedral phenocrysts of plagioclase are common, with orthopyroxene phenocrysts occurring less frequently. Slight alteration of the volcanic glass is evident from birefringent perlitic cracks. The blocky nature and low vesicularity of many shards in this deposit suggest that the shards are hyaloclastites which formed from spalling of glassy rinds of pillow lavas and/or sheet lava flows in a deep submarine environment. The angular to subangular shard shapes, large grain size and thickness of this sequence suggest a proximal source. The homogeneous chemical and petrological composition of the glass shards suggests an origin from a single eruptive event.

The thickest vitric turbidite (5.2 m) occurs in Subunit IIB (Sections 135-838A-5H-1 to -5H-4). It is dark grey to black in color and normally graded, with centimeter sized clasts at its base. The darker color and higher magnetic susceptibility compared to the dacite flow immediately below suggests that the dominant shard population has a more mafic composition, presumably ba-

saltic andesitic to andesitic, with a higher concentration of ferromagnesian minerals. Shard size and inferred chemical composition indicate that the flow may well be a proximal hyaloclastite similar to those in Sections 135-838A-9H-1 to -9H-4.

Thin Turbidites with Vitric-rich Bases

Turbidites with vitric-rich bases grading upward into clayey nanofossil oozes are usually <0.5 m in thickness. The vitric-rich base rarely exceeds 10% of the total thickness. These turbidites are restricted to Sections 135-838A-4H-4 and -4H-5, and cover a narrow age range from 1.10 to 1.14 Ma, based on the sedimentation rate curve for this interval of Hole 838 (see "Sedimentation Rates" section, this chapter).

Pumiceous Gravels

Three pumiceous gravel (PG) deposits, ranging in thickness from 7.6 to 18.0 m, contain large amounts of lapilli-sized pumice. These occur in Sections 135-838A-6H-2 to -6H-7 (PG1), 135-838A-7H-1 to -8H-2 (PG2), and 135-838A-10H-1 to -11H-6 (PG3) and correspond to ages of about 1.5, 1.7, and 1.9 Ma, respectively (see "Sediment Accumulation Rates" section, this chapter). The three deposits constitute about 30% of the total thickness of sediment recovered at Hole 838A.

The three deposits are characterized by large clasts (a maximum size of 7 cm occurs at the base of PG2) and by their great thickness (up to 18 m). They are generally normally graded, although this is poorly defined over some intervals. Maximum diameters of pumice clasts range from 4 to 7 cm in the lower third of individual beds and range from <1 to 2 cm in the upper third of the beds. Grain-size sorting is generally poor. Within the beds, 10-cm-thick intervals with finer or coarser average grain size occur, as well as reversely graded intervals (PG3). Pumice clasts are mostly light gray and are normally well rounded to subrounded. Larger clasts are often subangular. All three gravels contain small proportions of black, angular vitric clasts which are interpreted as hyaloclastites. They are normally about an order of magnitude smaller in grain size than the pumice clasts, but reach 0.5 cm in diameter in the lowermost part of PG3 where they are most abundant and constitute about 50% of the sediment. Rare mudclasts, which are partially indurated, occur in all three gravels.

SiO₂ concentrations of pumice from PG2 and PG3, as estimated from refractive index determinations of crushed gravel, are approximately 70 wt%. This is in agreement with an XRF analysis of a pumice clast from PG2 of 72.1 wt% SiO₂ (see Table 10, "Igneous Petrology" section, this chapter). According to the FeO*/MgO ratio (where FeO* = total Fe expressed as FeO) at a given SiO₂ concentration (Miyashiro, 1974) and K₂O at a given SiO₂ concentration (e.g., Wilson, 1989), this pumice composition is likely to have evolved within a calc-alkaline magmatic series. Phenocrysts comprise plagioclase with complex zonation patterns as the dominant phase, rare subhedral green to brown amphibole, subhedral quartz with resorption textures (Fig. 15), and euhedral to subhedral Fe-Ti oxides. Angular hyaloclastites, which occur in varying proportions (particularly in PG2 and PG3), are basaltic andesite in composition, with approximately 53 wt% SiO₂ (determined by refractive index measurements).

The pumice clasts in the gravels may originate from Plinian subaerial or shallow submarine eruptions from the margins of the Lau Basin (the Lau Ridge or Tofua Arc) or from seamounts (or former islands which are now submerged) within the Lau Basin. It is probable that they were initially deposited close to their eruptive center (average and maximum grain sizes of the deposits suggest deposition within 5 to 10 km) on the upper part of a steep, high submarine slope with subsequent redeposition. The thick-

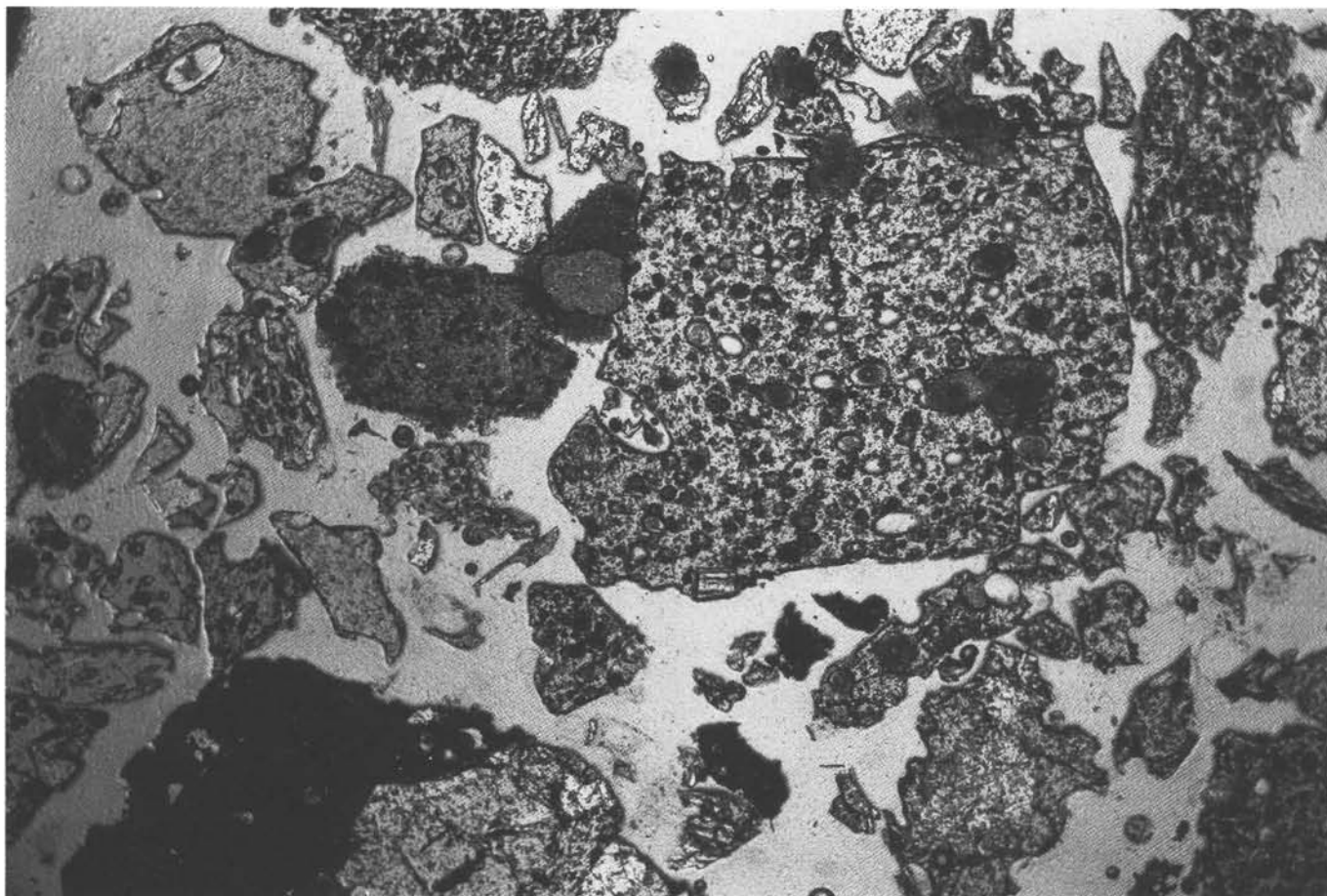


Figure 14. Photomicrograph of nonvesicular to medium-vesicular blocky, angular shards of basaltic andesite composition (Sample 135-838A-9H-2, 95–117 cm); long side of photomicrograph is about 6 mm in length, plane polarized light.

ness of the deposits and the abundance of clasts in the lapilli size range suggest that these may be proximal deposits.

Igneous rock with compositions compatible with the pumice in PG2 have not been identified in any of the potential source areas for these deposits. On islands in the Tofua Arc, rhyolitic igneous rocks are very rare and lack either amphibole or quartz phenocrysts (e.g., Ewart et al., 1973). Matrix glass in dacite vitrophyre dredged from Zephyr Shoal in the Lau Basin has a similar major element composition to the pumice in PG2, but the rock has xenocrystic labradorite, augite, and bronzite and the bulk composition is dacite (Hawkins, 1985).

Proximal Reworked (Slump) Facies

In the upper and lower parts of Subunit IID (Sections 135-838A-8H-3 to -8H-4 and -9H-6), two intervals 1.2 and 2.28 m thick, respectively, contain a crudely bedded but otherwise structureless mixture of lapilli-sized pumice clasts, mafic volcanic clasts, and both soft and indurated clasts of clayey nannofossil ooze (up to 20 cm in diameter). The clasts are supported in a matrix of yellow to dark yellow and dark brown clayey nannofossil ooze. These intervals are interpreted as local slump deposits.

Unit III

Unit III comprises indurated volcanoclastic sediments with grain sizes in the silt size range. In Section 135-838A-16X-1 and Core 135-838A-17X, glass shards are completely replaced by brown and yellow clay minerals (probably smectite), whereas interstices are filled by a needle-like, colorless to dirty brown

zeolite with very low first-order birefringence (probably natrolite/thomsonite) and carbonate.

Sample 135-838A-17X-CC, 0–3 cm, is a well-sorted vitric sandstone and comprises highly altered (to clay minerals) vitric shards, igneous minerals, and some foraminifers. Maximum grain size is around 700 μm and grains <100 μm are rare. The vitric sandstone consists of (1) abundant yellow to light brown, subangular to subrounded, commonly equidimensional shards that are typically slightly vesicular to nonvesicular (interpreted as hyaloclastites); (2) abundant yellow to light brown, angular to subangular shards that are slightly elongate and contorted and have preserved fibrous pumice clast textures; (3) orange-brown to dark reddish brown fragments, often with abundant plagioclase groundmass laths; (4) igneous minerals that constitute about 10 vol% and are mainly euhedral plagioclase but include subrounded and highly irregular, fragmented plagioclase, and minor quantities of clinopyroxene, orthopyroxene, and Fe-Ti oxides, and; (5) rare, well-rounded mudclasts. The interparticle pore spaces are filled by a fibrous, colorless to dirty brown, very low birefringent zeolite (probably natrolite/thomsonite), which is oriented perpendicular to the surface of the particles.

Sample 135-838A-16X-1, 3–4 cm, differs from Sample 135-838A-17X-CC, 0–3 cm, in having a coarser grain size (mainly >1 mm in diameter), more rounding of clasts and minerals, and a higher abundance of vesicular shards and lithic fragments. Some of these lithic fragments are well crystallized and intersertal glass is replaced by smectite. Zeolite (probably natrolite/thomsonite) fills most of the pore spaces and some of the vesicles within the

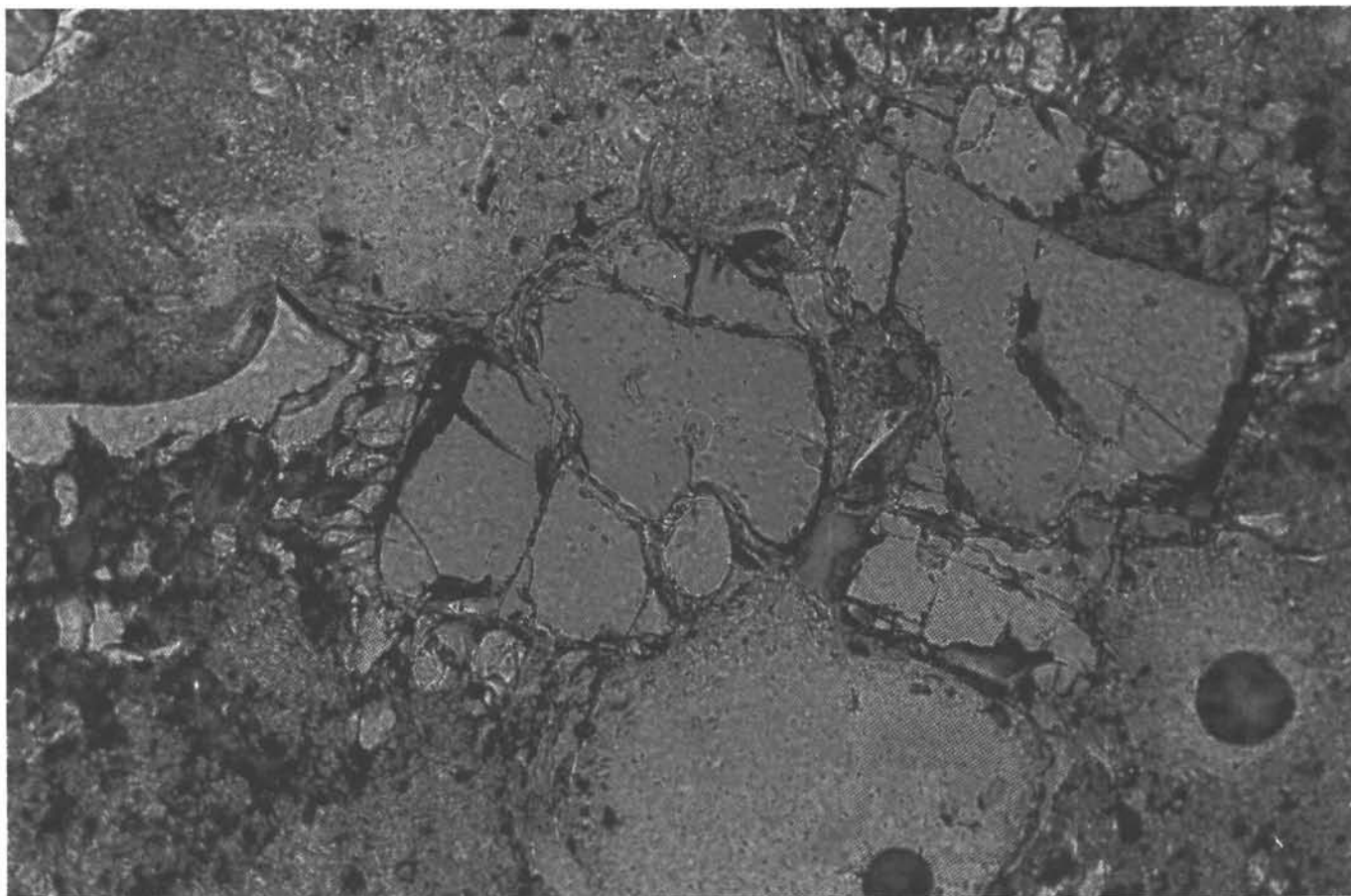


Figure 15. Photomicrograph of glomerophyric, euhedral, and slightly corroded quartz phenocrysts in rhyolitic pumice clast (Sample 135-838A-8H-1, 137–140 cm); long side of photomicrograph is about 3 mm in length, using partially crossed polarizers.

shards. Rounded carbonate globules, 20 to 50 μm in diameter, are also present (Fig. 16).

A 1.22-m-thick, black, coarse-grained, normally graded polymict gravel, containing well-rounded clasts (up to 3 cm in diameter), occurs in Core 135-838A-20H. Clasts include black vitric and lithic fragments, pumice, and green, highly altered tuffs. Three clasts, each about 1 cm in diameter, were examined in thin section. All show very pronounced fluidal textures as a result of alignment of plagioclase and clinopyroxene microlites and, in one clast, by the preferred orientation of elongate vesicles. These make up to 10 vol% of the clasts. The three clasts show variations in the abundance and size of groundmass microlites, which often show quench textures. The microlites occur in a light brown, optically fresh glass. Phenocryst modes are variable. Clast 1 is aphyric, whereas clast 2 contains plagioclase phenocrysts (<500 μm) and augite microphenocrysts, both making up <1 vol% of the clast. Clast 3 has about 10 vol% of mainly euhedral plagioclase (<1.4 mm), less abundant euhedral clinopyroxene phenocrysts (<400 μm), and euhedral magnetite microphenocrysts (<100 μm).

Depositional History

Biostratigraphic data from the lower parts of Holes 838A and 838B shows that sedimentation at Site 838 began in the late Pliocene (about 2.0 Ma). However, failure to reach basaltic basement in both holes means that we have an incomplete knowledge of the early sedimentary sequence and hence the early history of sedimentation in the basin.

The oldest sediments recovered at Site 838 consist of polymict volcanic gravel interbedded with granular coarse-grained vitric

sand, volcanic conglomerate, vitric sandstone, and vitric clayey siltstone. The composition of volcanic gravel clasts (mafic igneous rock, pumice, and tuffaceous sediments) suggests these were originally derived from hyaloclastites, fragments of broken pillow lavas, and mafic breccias. The volcanic gravels and vitric sands and silts were probably deposited by sediment gravity flows. Unit III probably contains quite thick sequences of volcanic gravel, although poor recovery makes this difficult to establish. The composition of glasses in the vitric sandstones and the vitric clayey siltstones of Unit III shows that most of the glass debris is derived from a rhyolitic to dacitic source, although there is also evidence for a basaltic andesite source.

Accumulation of coarse volcaniclastic sands, gravels, and silts continued within the sub-basin until 1.4 Ma (see "Sediment Accumulation Rates" section, this chapter). These sediments were deposited as upward-fining cycles, grading from gravels into sands and silt (Subunits IIE to IIB). They are interpreted as sediment gravity flow deposits which accumulated at the base of relatively steep submarine slopes (see "Background and Objectives" section, this chapter). Clayey nannofossil oozes, representing intervals of pelagic deposition, occur between major volcaniclastic deposits. Within Unit II, some poorly sorted gravels contain a high proportion of mudclasts intermixed with the pumice debris. These sediments were probably deposited as slumps from nearby sources.

The supply of coarse debris and turbiditic material to the sedimentary sequence at Site 838 was sharply reduced since 1.4 Ma. Sediments in the upper part of Subunit IIB and Unit I are predominantly clayey nannofossil oozes, representing pelagic

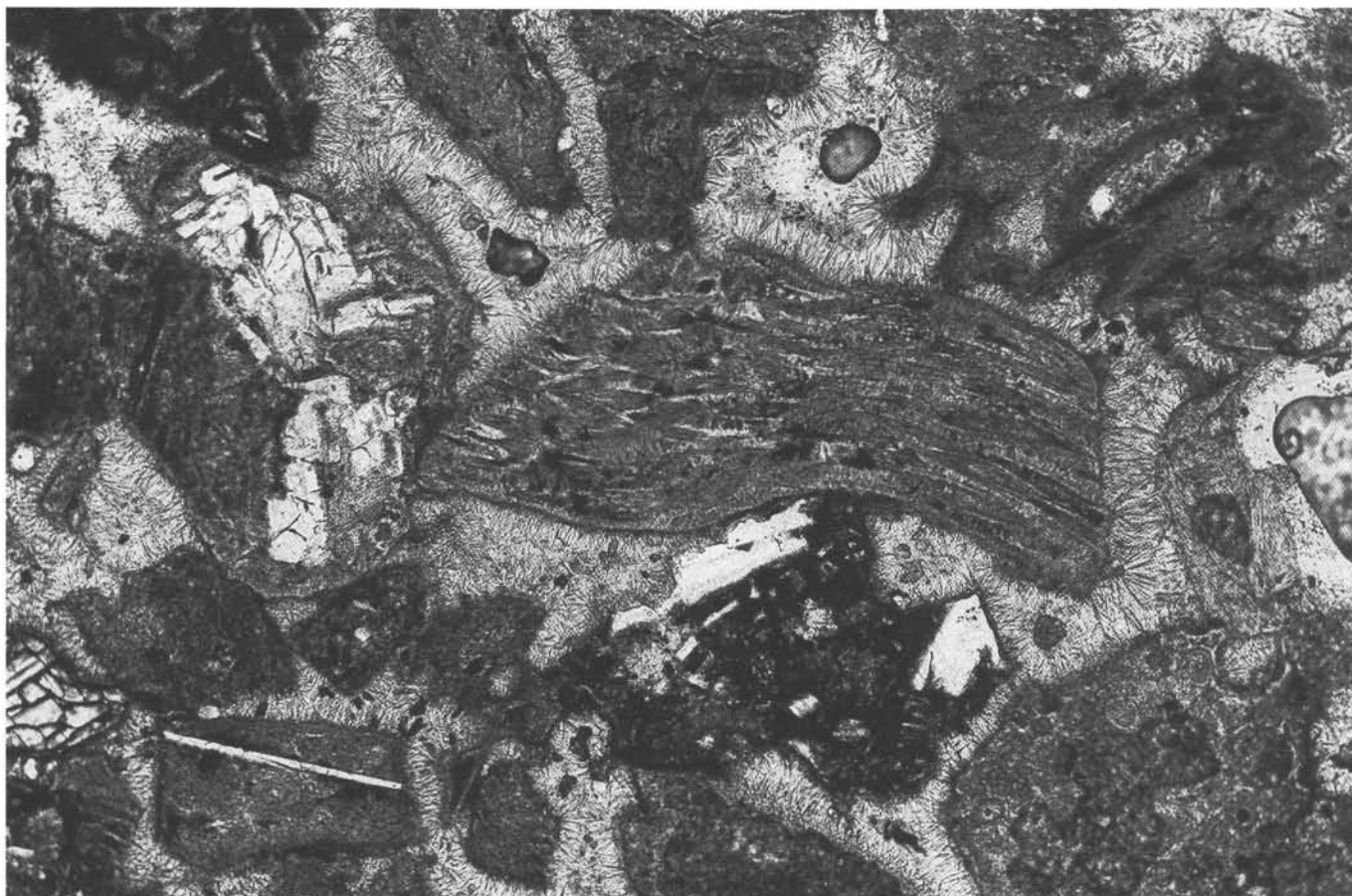


Figure 16. Photomicrograph of subangular, slightly elongate fibrous glass shard and several blocky, angular shards now completely altered to yellowish brown clay (probably smectite). Note the dark, slightly irregular clast with tachylitic groundmass, including a number of plagioclase laths. Interparticle pore space is completely occupied by fibrous, needlelike zeolite (probably natrolite-thomsonite), oriented perpendicular to the surface of the volcanic clasts. Rounded carbonate globules, 20–50 μm in diameter, occur in the central parts of the interparticle pore spaces (Sample 135-838A-16X-1, 3–4 cm); long side of photomicrograph is about 3 mm in length, plane polarized light.

sedimentation. Sporadic volcanoclastic turbidite deposits and two thin pyroclastic fine ash layers occur in these sediments. The occurrence of small fragments of weathered pumice throughout Unit I reflects continued arc volcanism within the region. Staining of the clayey nannofossil oozes in Units I and II by iron-oxhydroxides suggests a continuous hydrothermal input to these sediments during their deposition.

STRUCTURAL GEOLOGY

Hole 838A is situated at the south-facing flank of a broad northeast-tapering wedge-shaped basin (see “Background and Objectives” section, this chapter). It lies about 15 km to the southwest of Site 839 and approximately 87 km to the west of the ELSC. Single-channel seismic reflection data show that the two holes drilled at Site 838 were sited on a narrow 1-km-wide terrace which interrupts a slope otherwise dipping gently (approximately 2°) southward. Near-surface reflectors on either side of the terrace also gently dip southward, if slightly irregularly. However, beneath the terrace itself, seismic reflectors below 0.3 s TWT are difficult to resolve and are locally confused.

Dip Measurements on Cores

The attitude of sedimentary bedding in the recovered core from Hole 838A was measured following the procedures described in the “Structural Studies” section, “Explanatory Notes” chapter

(this volume). Twelve dip readings were taken in the range from 19.3 to 76.2 mbsf, most from the bases of turbiditic horizons, either from their contacts with underlying nannofossil oozes or from sedimentary laminae within the finer grained portions of turbidite flows. No bedding was visible in the coarser grained volcanoclastic horizons or in uniform areas of nannofossil ooze.

The multishot orientation tool was used for Cores 135-838A-4H to -8H, inclusively; however, no data were obtained from Cores 135-838A-7H and -8H because the film in the tool apparently failed to advance. Application of the multishot data from the remaining cores (given in Table 6; see “Paleomagnetism” section, this chapter) to the eight bedding planes in Cores 135-838A-4H to -6H (from the interval 27.5–50.6 mbsf) apparently restores them to a consistent northwest dip direction (Fig. 17, although see discussion below). A slight increase of dip with depth is suggested, although the data are insufficient in number to demonstrate this unequivocally. The steeper dips (e.g., $>30^\circ$) occur below approximately 50 mbsf (i.e., within or beneath the 20-m-thick deposit of massive, poorly sorted polymictic volcanic gravels that form lithostratigraphic Subunit IIC; see “Lithostratigraphy” section, this chapter).

The gravels are interpreted as mass-flow deposits; their textural and compositional immaturity suggests that they are derived from an extremely proximal source. We speculate that their deposition could have been initiated by local faulting, perhaps on the northwest-striking lineament that flanks the basin immediately to

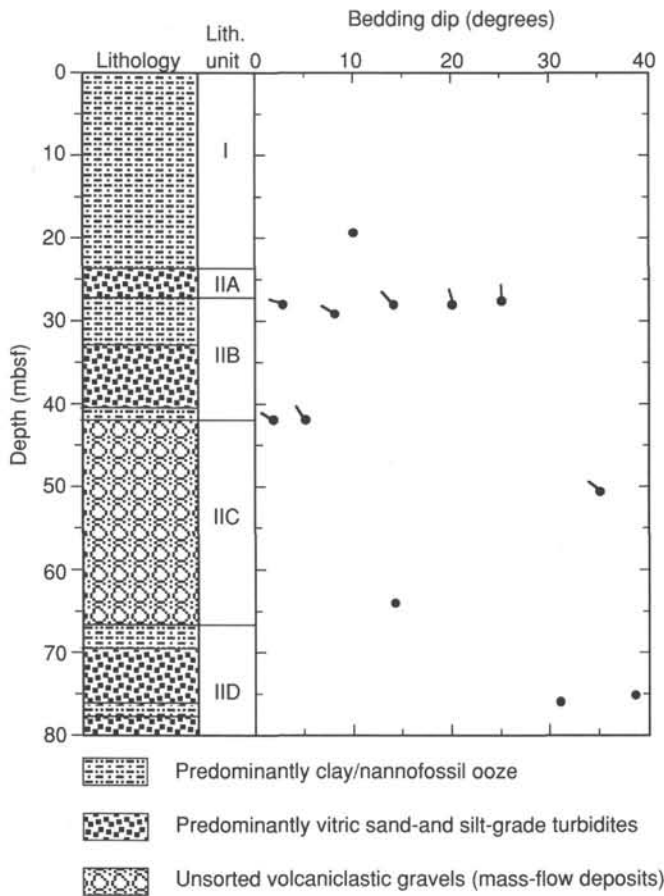


Figure 17. Dip of sedimentary bedding vs. depth, Hole 838A, reoriented to geographical coordinates (true north) using the multishot orientation tool, with a summary lithologic log for reference. Note the general increase of dip with depth in Subunit IIC, with steeper dips below approximately 50 mbsf. See text for discussion.

the north and northwest of Site 838. The steeper dips beneath the gravel deposit could possibly be syntectonic.

Dipmeter Measurements from Logs

Dip data from the core were augmented by bedding inclination and orientations calculated from mean square dip (MSD) dipmeter processing of formation microscanner (FMS) logging data (Schlumberger, 1986; see "Downhole Measurements" section, this chapter, and "Explanatory Notes" chapter, this volume) over the interval 60.9–225.6 mbsf in Hole 838B. MSD-derived dips were verified by the recalculation of dips over the same interval by the continuous side-by-side (CSB) dipmeter processing technique (Schlumberger, 1986). The core-derived and representative FMS dipmeter data are presented and compared in Figure 18. Surprisingly, there is little correlation between the two data sets; in fact, there is a marked anticorrelation. The core-derived data show a northwesterly dip, with a Fisher mean vector distribution of dip direction of 319° azimuth and 14° inclination, with α_{95} (95% cone of confidence) of 13.2 and concentration factor (k) of 18.3. In contrast, the MSD dipmeter data dip toward the southeast, with a Fisher mean dip direction of 134° azimuth and 22° inclination, with $\alpha_{95} = 7.2^\circ$, and $k = 14.2$ (Fig. 18). Regrettably, there is no overlap between the two sets of data.

The 180° disparity between the two sets of data presented in Figure 18 is disturbing. Either it results from an orientation error in the derivation of core-derived or FMS dipmeter measurements,

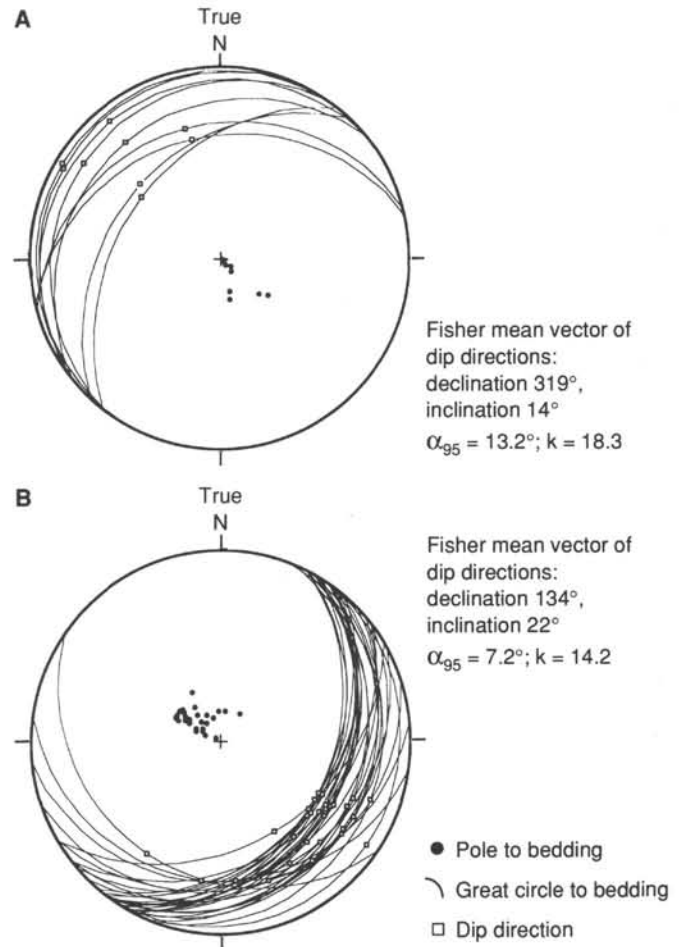


Figure 18. Lower hemisphere equal-area stereographic projection of hand-measured dips ($N = 8$) from Hole 838A (A) and representative dips ($N = 31$) derived from mean-squares-dip processing of formation microscanner (FMS) data from Hole 838B (B). Note the 180° disparity between the two sets of data. See text for discussion.

or else a geological explanation must be invoked. These possibilities are discussed below.

Possible Orientation Errors

Core-derived Measurements

The dips taken from the core recovered at Hole 838A were measured by the method of two apparent dips described in the "Structural Studies" section of the "Explanatory Notes" chapter (this volume), using the same spreadsheet routine as used at all previous sites. All data were recalculated from the raw data by hand and verified independently, and no errors in the process were found.

The multishot orientation tool, used to orient the dips calculated in the described manner, has occasionally been proven unreliable in use, both on previous ODP legs and during Leg 135. At Site 834, a 30°–40° mismatch between the expected and calculated magnetic declinations was discovered, and this was later found to have resulted from a combination of the breakage of a bolt in the sinker bar assembly and the misalignment of one of the two compasses used (compass B: see "Paleomagnetism" section, "Explanatory Notes" chapter, this volume). A correction factor of +13° was subsequently calculated to account for the compass misalignment. However, a further complication was

encountered at Site 835, with apparent reverse polarity declinations encountered in samples from Cores 135-838A-11H and -12H that otherwise displayed normal polarity inclinations (see "Paleomagnetism" section, "Site 835" chapter, this volume). It is thought that the multishot tool was probably installed backward on the sinker bar assembly, which implies that the declination values for those two cores are in error by 180° .

This error was noticed at Site 835 because of inconsistencies that came to light upon the restoration of the paleomagnetic data using the multishot orientations. At Site 838, however, remanent magnetization induced by drilling does not appear to have been removed at the maximum 15-mT level of demagnetization possible onboard ship, so the magnetization vectors isolated at this level of cleaning rarely yielded reliable indicators of declination in sediments from Core 135-838A-4H and below (see "Paleomagnetism" section, "Site 838" chapter, this volume). It is not possible, therefore, to confirm with any degree of certainty the validity of the multishot data from Cores 135-838A-4H to -6H.

The paleomagnetic data could not be used as an independent check on the multishot tool orientations, not only because of the drill string overprint, but also because the magnetic declination data were scattered. Furthermore, application of the multishot corrections to these paleomagnetic measurements did not restore them to north or south directions; rather, the partially cleaned magnetic vectors appeared to be declined predominantly westerly or easterly. This may indicate an error in the multishot tool orientation.

FMS/Dipmeter

Dipping planar features appear as sinusoidal traces on the FMS plots, which show an unwrapped view of the borehole wall, oriented relative to true north (Fig. 46, "Downhole Measurements" section, this chapter). The dip direction of any plane corresponds to the azimuth of the maximum depth of the sinusoid. The southeasterly dips picked by MSD processing of the FMS data from Hole 838B, using standard selection parameters, match reasonably closely those visually selected from the FMS images; therefore it appears that the MSD dipmeter software is functioning correctly. CSB dipmeter data, however, which are derived from the raw Schlumberger tapes and processed on the Schlumberger Cyber Service Unit (CSU) system, show a similar southeasterly dip overall, suggesting that no systematic orientation error can have been introduced during processing.

A further possibility is that a malfunction of the FMS tool occurred, or that it was miscalibrated. The FMS tool used at Site 838 is the same as that used at all previous sites of Leg 135, at which no such orientation errors have been suspected. Input of calibration parameters by the Schlumberger engineers was the same as for all other sites. A test run of the FMS tool on the rig floor showed that the azimuth of the number 1 pad arm of the tool indeed had the same orientation as the number 1 pad azimuth reading on the CSU monitor. No malfunction or miscalibration of the FMS tool can therefore be invoked.

Geological Phenomena

In the discussion above, no systematic errors were found, either in the method of measuring bedding planes from cores, or in the calculation of dipmeter information from the FMS data. It cannot be shown with certainty that the 180° mismatch in dip directions is a result of operating difficulties with the multishot orientation tool, because the paleomagnetic data were not completely demagnetized. However, the partially cleaned magnetic data do suggest (though cannot prove) that some problems with the tool may have been occurring.

There is some justification, therefore, for ignoring the azimuthal component of all of the core-derived bedding data shown

in Figures 17 and 18. However, the magnitudes of the dips, measured with respect to the axis of the borehole, are still valid, and the discussion of the possible unconformity given in the previous section on "Dip Measurements on Cores" remains equally plausible.

The FMS data, supported by the single-channel seismic reflection record (see "Background and Objectives" section, this chapter), suggest that the entire sedimentary sequence at Site 838 has been tilted toward the southeast, about an axis apparently parallel to the northwest-southeast elongation of the Site 838 basin. The apparent increase of dip with depth may indicate activity on the basin-bounding faults, probably during the latest Pliocene/earliest Pleistocene. The tilting can be explained in terms of normal movement on a rotational northwest-dipping fault or fault system that flanks the basin to the southeast (Fig. 19).

A fault structure is observed on the FMS records from Hole 838B. At 113–114 mbsf in Hole 838B dark features up to 30 cm thick are clearly visible on three and possibly all four FMS pads. The features coincide with a local increase in hole diameter as recorded on the caliper log. They define a sinusoidal pattern, indicating that they form a plane with strike of 240° and dip of 75° toward the northwest. This plane separates massive volcanoclastic gravels above from regularly bedded sediments (dipping at 30° southeast) below, and we suggest that it represents a minor component of the major basin-bounding fault structure postulated above.

If, however, one accepts the multishot orientation data from Cores 135-838A-4H to -6H (Figs. 17 and 18) as valid, a change in dip direction from southeast (in the lower part) to northwest (in the upper part of the borehole) is implied. If so, the changeover in dip direction has to be sited precisely in the 10-m gap (between 50.6 and 60.9 mbsf) below the lowest multishot-reoriented stratum and above the highest dipmeter measurement, if one assumes that Holes 838A and 838B sampled identical sections. This appears unlikely and is to us an unsatisfactory explanation. Alternatively, one could propose models that, for example, invoke a substantial fault between the two boreholes and postulate that synthetic and antithetic faulting effected differential rotations between the blocks, or that a large sedimentary drape or slumped horizon was deposited over a tectonically rotated sedimentary block. Although comparison of the FMS images from Hole 838B with the lithostratigraphic column from Hole 838A (Fig. 46; "Downhole Measurements" section, this chapter) suggests that a 1:1 correlation between the sedimentary sections of the two holes cannot be made (see "Downhole Measurements" section, this chapter), and although the single-channel seismic reflection profiles are locally disturbed in the vicinity of Site 838 itself (see

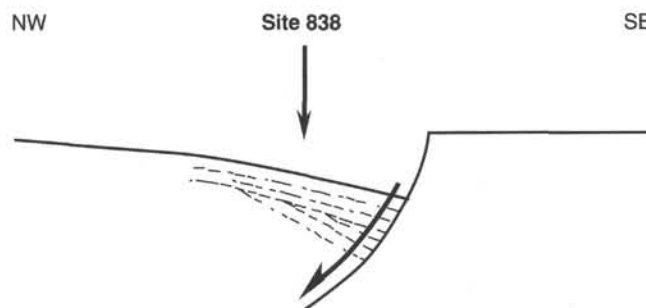


Figure 19. Sketch illustrating preferred model for the structure of Site 838. Bedding dip is toward the southeast and increases with depth, suggesting that faulting accompanied sedimentation. Tilting of the sequence is postulated about a northwest-dipping rotational normal fault bounding the basin to the southeast.

"Background and Objectives" section, this chapter), we have no other reason to suspect the existence of a fault lying in the 20-m interval between Holes 838A and 838B.

BIOSTRATIGRAPHY

The sedimentary sequence of Site 838 is divided into two stratigraphic units (see "Lithostratigraphy" section, this chapter). Unit I extends from Cores 135-838A-1H to -3H and is composed mainly of nannofossil ooze. Unit II, ranging from Cores 135-838A-4H to -11H, is characterized by nannofossil ooze and volcanic sand with gravel (Fig. 20). Calcareous nannofossils and planktonic foraminifers are abundant and well preserved from Samples 135-838A-1H-CC to -6H-CC, but the occurrence of microfossils is sporadic in the interval between Cores 135-838A-7H and -20H.

The sediments at this site range from middle Pleistocene to late Pliocene in age. The middle Pleistocene fauna occurs in Cores 135-838A-1H and -2H. The middle/early Pleistocene boundary is placed near the base of Core 135-838A-2H. The Pleistocene/Pliocene boundary (base of nannofossil Subzone CN14a of Okada and Bukry, 1980) is within Core 135-838A-7H. The sediments at the bottom of this hole (Core 135-838B-13R) contain a late Pliocene flora and fauna which indicates nannofossil Subzone CN12a of Okada and Bukry (1980) and the planktonic foraminiferal *Globigerinoides quadrilobatus fistulosus* Zone of Chaproniere (1991).

The biostratigraphic results for Holes 838A and 838B are summarized in Figures 20 and 21.

Calcareous Nannofossils

Pleistocene

Sample 135-838A-1H-CC was found to contain a flora that includes *Gephyrocapsa oceanica* and *Pontosphaera indoceanica* and not *Emiliania huxleyi* or *E. ovata*. For this reason it has been assigned to Subzone CN14b.

Samples 135-838A-2H-CC through -6H-CC yielded floras containing *Emiliania ovata* and *Gephyrocapsa oceanica*. On this basis, these samples have been referred to Subzone CN14a.

Pliocene

Sample 135-838A-8H-CC contains a flora including *E. ovata*, *Pseudoemiliania lacunosa*, and *Calcidiscus macintyreii* but not *Gephyrocapsa caribbeanica* or *G. oceanica*. Therefore, the sample has been assigned to Subzone CN13a. This sample also includes several overgrown discoaster fragments which could not be identified to species. If these are in place the age assignment could be slightly older (Zone CN12).

Samples 135-838A-11H-CC and -15X-CC yielded sparse, poorly preserved floras, including *C. macintyreii* and *Discoaster brouweri*. These samples are tentatively assigned to Subzone CN12d.

Sample 135-838B-2R-CC was found to contain a sparse, poorly preserved flora, including *P. lacunosa*, *E. ovata*, *C. macintyreii*, overgrown 5- and 6-ray discoasters, and a single identifiable *Discoaster pentaradiatus*. On this basis, the sample is probably best assigned to Subzone CN12c.

A poorly preserved flora, including *P. lacunosa*, *E. ovata*, and *C. macintyreii*, overgrown 5- and 6-ray discoasters, and questionable *Discoaster asymmetricus*, *D. surculus*, and *D. brouweri*, was found in Sample 135-838B-9R-CC. On this basis it is assigned to Zone CN12.

Sample 135-838A-17X-CC contained a common, poorly preserved flora, including *P. lacunosa*, *C. macintyreii*, and overgrown specimens of *Discoaster brouweri*, *D. asymmetricus*, *D. pentaradiatus*, and *D. tamalis*. The sample is thereby assigned to Subzone CN12a.

Samples 135-838B-11R-CC through -13R-CC contain abundant, well-preserved floras, including *P. lacunosa*, *E. ovata*, *C. macintyreii*, *D. asymmetricus*, *D. brouweri*, *D. surculus*, and *D. tamalis*. These samples are assigned to Subzone CN12a.

Sample 135-838A-20X-CC contains a very sparse, poorly preserved flora without age-diagnostic taxa.

Samples 135-838A-7H-CC, -9H-CC, -10H-CC, -12X-CC through -14X-CC, -18X-CC, and Sample 135-838B-10R-CC are barren of calcareous nannofossils.

Planktonic Foraminifers

A total of 26 core-catcher samples were examined for planktonic foraminifers at Site 838. Six samples that were taken from the interval between Cores 135-838A-1H and -6H contain abundant and well-preserved planktonic foraminiferal faunas ranging in age from early to middle Pleistocene. Within the interval between Cores 135-838A-9H and -20H these assemblages, however, are less diverse and poorly preserved; some are barren.

Four samples were taken in Hole 838B. These samples yielded late Pliocene foraminiferal faunas ranging from the *Globorotalia viola* Subzone to the *Globigerinoides quadrilobatus fistulosus* Subzone.

Middle Pleistocene

Samples 135-838A-1H-CC and -2H-CC are assigned to the middle Pleistocene *Globorotalia (Truncorotalia) crassaformis hessi* Subzone, based on the occurrence of *Gr. (Tr.) truncatulinooides*, together with *Globorotalia (Globorotalia) tumida tumida*, *Gr. (Globoconella) inflata*, *Pulleniatina obliquiloculata* (dextrally coiled), *Gr. (Gr.) cultrata menardii*, *Gr. (Gr.) cultrata neoflexuosa*, *Globigerinoides conglobatus*, and *Neoglobobularina dutertrei*. *Gr. (Tr.) tosaensis* is absent from these samples.

Lower Pleistocene

The interval between Samples 135-838A-3H-CC and -6H-CC is early Pleistocene (*Globorotalia (Truncorotalia) crassaformis viola* Subzone) in age on the basis of the co-occurrence of *Gr. (Tr.) tosaensis* and *Gr. (Tr.) truncatulinooides*, together with *Gr. (Gr.) tumida tumida*, *Gr. (Globoconella) inflata*, *Globigerinoides conglobatus*, *Gds. ruber*, *Gds. elongatus*, *Sphaeroidinella dehiscentis*, and *Pulleniatina obliquiloculata* (dextrally coiled).

Upper Pliocene

Samples from Sections 135-838A-8H-CC and -11X-CC and Cores 135-838A-14X and -15X yielded late Pliocene planktonic foraminiferal assemblages that are correlated with the lower part of the *Globorotalia (Truncorotalia) crassaformis viola* Subzone. These assemblages are characterized by the absence of *Globigerinoides quadrilobatus fistulosus*. Core 135-838A-20X is tentatively assigned to the *Globigerinoides quadrilobatus fistulosus* Subzone based on the co-occurrence of *Gr. (Tr.) truncatulinooides*, *Gr. (Tr.) tosaensis* and *Gds. obliquus extremus*. Other representative species in this interval are *Gr. (Gr.) multicamerata*, *Gr. (Tr.) crassaformis crassaformis*, *Sphaeroidinella dehiscentis dehiscentis*, *Gds. conglobatus*, *Gds. ruber*, and *Gds. elongatus*.

Samples 135-838B-11R-CC and -13R-CC lack *Gds. quadrilobatus fistulosus* but contain the dextrally coiled *Gr. (Gr.) cultrata* group (which generally accompany *Gds. quadrilobatus fistulosus*); in addition, Sample 135-838B-12R-CC contains *Globigerinoides quadrilobatus fistulosus*. These three samples are, therefore, assigned to the *Gds. q. fistulosus* Subzone.

SEDIMENT ACCUMULATION RATES

Both biostratigraphic and paleomagnetic data indicate that the age of the sediments at Site 838 ranges from the middle Pleisto-

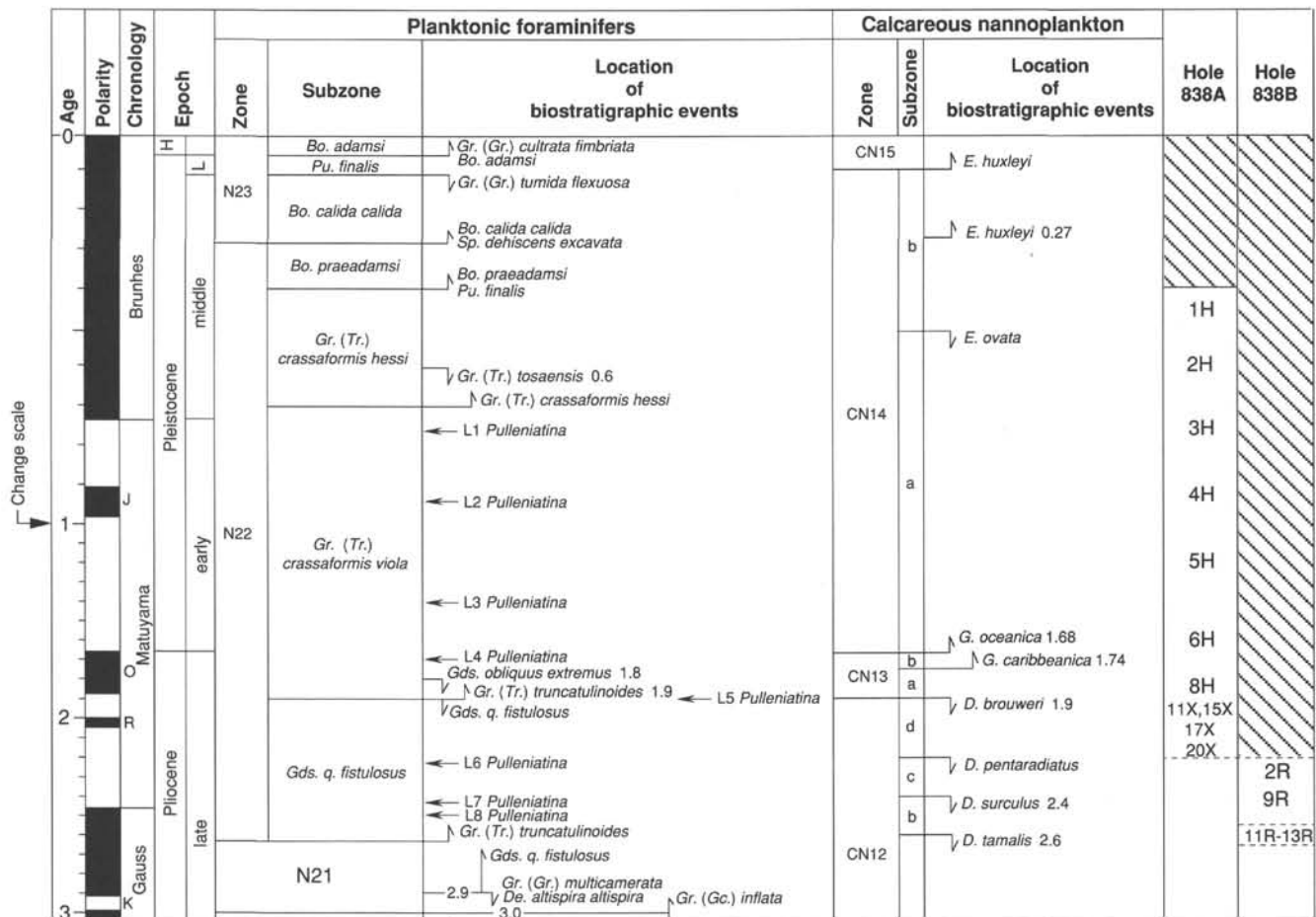


Figure 21. Paleontology summary chart, Site 838. See Figure 1 caption for an explanation of the symbols and abbreviations used.

cene to the latest Pliocene (Brunhes and Matuyama chrons). The sediment sequence consists largely of tuffaceous sands with some interbedded calcareous ooze horizons. The amount of volcaniclastic material greatly increases downcore, and is concentrated from the base of Core 135-838A-7H to within Core 135-838A-11H, an interval with little paleontologic control. Overall, the preservation and diversity of the planktonic assemblages are good, but moderate to poor faunal assemblages and barren intervals occur below approximately 55 mbsf.

Figure 22 is a graphic presentation of depth and biostratigraphic data from Site 838, with the bioevents used to construct this figure given in Table 5. Two sets of biostratigraphic data have been used: one based on an extinction level (LAD) of *Gr. (Tr.) tosaensis* set at 0.6 Ma (Berggren et al., 1985a, 1985b), and the other with this extinction event placed at 0.9 Ma (based on the relationship between this event and the paleomagnetic data at Sites 834 and 837). In addition, paleomagnetic data, which are available for only the top 20 m of the core, have also been plotted with the biostratigraphic data.

As was noted for Site 837, the biostratigraphic data using the LAD of *Gr. (Tr.) tosaensis* at 0.9 Ma most closely fits the curve based on the paleomagnetic data, and we have used this plot to calculate the sediment accumulation rates.

The sediment accumulation curve can be divided into three sections, illustrating changes in the rates of accumulation. The lowermost part (A), between 260 and 55 mbsf, shows very rapid sedimentation rates of about 177 mm/k.y., coinciding with the level where the main ash beds are found. Between 55 and 18 mbsf

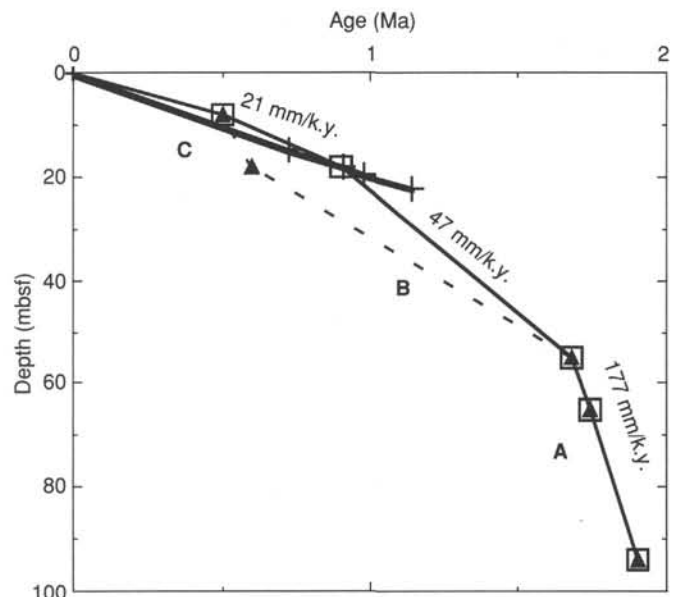


Figure 22. Graphic representation of age vs. depth data illustrating the sedimentation rates at Site 838 by means of the bioevents and depths given in Table 5. A plot of the paleomagnetic data is also included for comparison. Filled triangles = biostratigraphic data, open squares = biostratigraphic data with modified age for *Globorotalia (Truncana) tosaensis*, and plus signs = paleomagnetic data.

Table 5. Depths and ages of bioevents used to plot accumulation rates for Site 838.

Depth (mbsf)	Age (Ma)	Events
8.0	0.50	LAD <i>E. ovata</i>
18.0	0.60	LAD <i>Gr. (Tr.) tosaensis</i>
55.0	1.68	LAD <i>G. oceanica</i>
65.0	1.74	FAD <i>G. caribbeanica</i>
94.0	1.90	LAD <i>D. brouweri</i>
260.0	2.80	*Interpreted

Note: Asterisk (*) indicates age based on the interpretation that the bottom of Hole 838B is below the FAD of *D. tamalis* and above the FAD of *Gds. q. fistulosus*.

(B), the sedimentation rate decreases to about 47 mm/k.y., marking the interval over which the ash beds are thinner. From levels above 18 mbsf (C), sedimentation rates decrease to 21 mm/k.y., coinciding with levels where ash beds are very rare.

PALEOMAGNETISM

At Site 838, the magnetic measurement program followed the same format that was established at previous sites. Remanent magnetic measurements were made at 5-cm intervals on suitable archive core halves from the sedimentary section of Hole 838A. No measurements of basalts were made, either in Hole 838A or 838B, because of low recovery and the paucity of oriented pieces.

In order that the sediment measurements could be completed before sampling of the core working halves began, only two measurements were made on each section, one of the natural remanent magnetization (NRM) and one after alternating field (AF) demagnetization at 15 mT. Although intermediate steps were somewhat helpful at other sites in assessing the properties of the remanent magnetization, they consumed time and made it impossible to protect polarity reversal transitions from disruption by sampling. However, several discrete sediment samples were measured to yield details about magnetic properties.

Volume magnetic susceptibility measurements were made of whole-round core sections at 3-cm intervals using the Bartington MS-2 susceptibility meter with a 100-mm sensor loop on the multisensor track (MST). All Hole 838A APC core sections were measured as were those XCB cores with relatively full cross sections. Because of low recovery, only a few dozen susceptibility measurements were made on Hole 838B cores.

Remanent Magnetism

Sediments recovered at Site 838 have magnetic properties similar to those obtained at other Leg 135 sites. They are strongly magnetic, with NRM intensities ranging from 2 to 6500 mA/m. The large NRM intensities probably result from high concentrations of magnetic minerals derived from volcanic material. In addition, these magnetic minerals have low coercivities, with median destructive fields (MDF) typically less than 2–3 mT, so the sediments readily acquire a large upward-directed isothermal remanent magnetization (IRM) from the drill string (Fig. 23).

Most sediment samples displayed a stable characteristic remanence after the drill-string overprint was removed by AF demagnetization. However, a few were so weakly magnetic after removing the drill-string IRM that they did not yield a reliable direction when measured on the spinner magnetometer (Fig. 23). As did sediments from other Leg 135 sites, sediments at Site 838 also displayed saturation in applied magnetic fields less than 0.2–0.3 mT (Fig. 24), indicating that their magnetic minerals behave like magnetite.

Magnetic Polarity Stratigraphy

Magnetic polarity measurements were made only on sections of Cores 135-838A-1H through -6H, -8H, and -9H. Some sections of these cores, and all of the other APC cores, contained coarse-grained material that was unlikely to have recorded the magnetic field reliably during its deposition and was also frequently disturbed by coring. As a result, a reliable magnetic polarity stratigraphy was obtained only for Cores 135-838A-1H through -3H (Fig. 25). The Brunhes normal polarity chron was observed from the seafloor down to 14.7 mbsf (Table 6). Below that the Matuyama reversed polarity chron extends to the bottom of Core 135-838A-3H. Within the Matuyama Chron, two normal polarity subchrons were delineated. One is apparently the Jaramillo Subchron, whereas the other appears to be the short normal polarity event noted at Sites 834, 835, and 837 and correlated with the Cobb Mountain Event (Mankinen et al., 1978). Using the geomagnetic polarity reversal time scale (Harland et al., 1982; Berggren et al., 1985b), an age vs. depth diagram was constructed (Fig. 26) implying a middle Pleistocene sedimentation rate of 20 mm/k.y.

Below Core 135-838A-3H there were several short intervals of nanofossil ooze, similar to that in the upper three cores of Hole 838A, and these were measured to determine magnetic polarity. However, the ODP-mandated 15-mT maximum AF demagnetization for archive core halves did not allow the entire drill-string IRM to be removed from the sediments. This is evident, for example, by the lack of symmetry around zero of normal and reversed polarity magnetic inclinations (Fig. 25). Consequently, inclinations measured with the pass-through cryogenic magne-

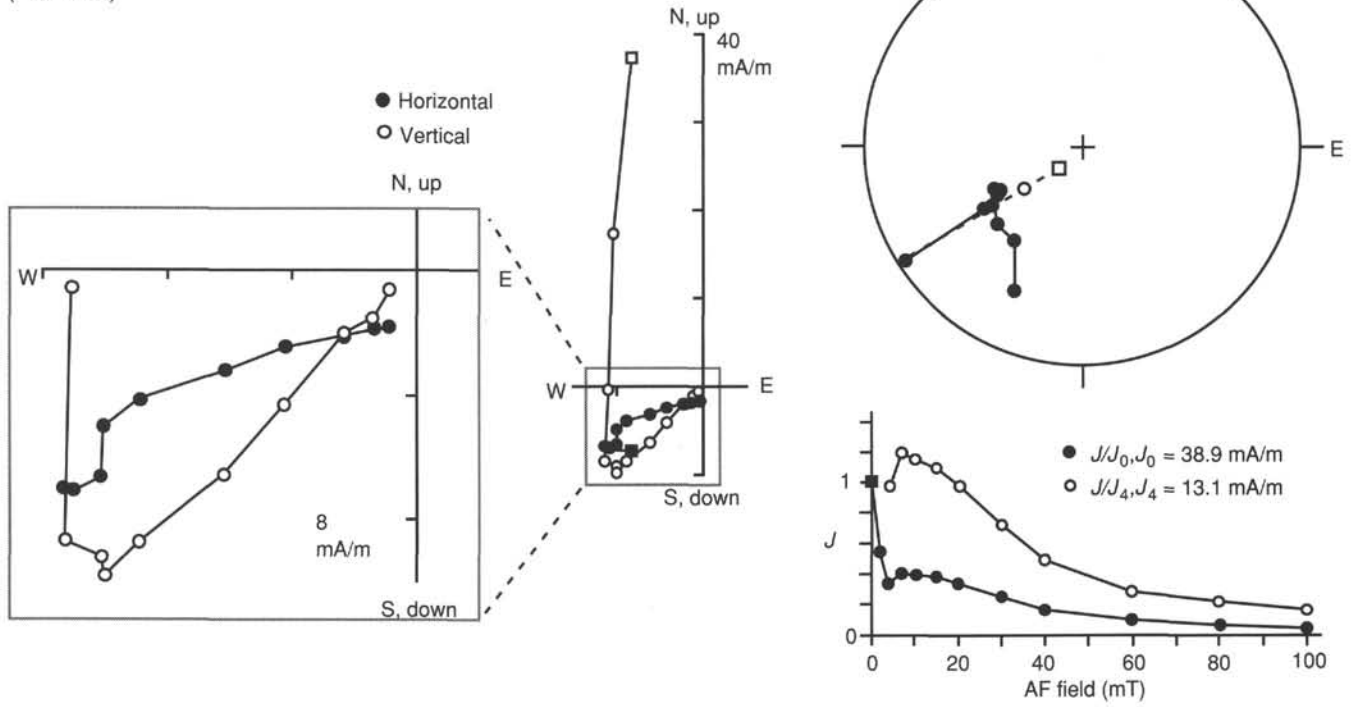
Table 6. APC-drilled core orientation data, Hole 838A.

Depth (mbsf)	Polarity (N, I, R)	Age (Ma)	Chron/subchron
0.0			BRUNHES
3.5	N		
3.7	I		
4.6	N?		
13.0	N		
13.2	I		
14.7	N	0.73	BRUNHES
18.2	R	0.91	MATUYAMA
19.8	N	0.98	Jaramillo
21.7	R		
22.1	N	1.12	Cobb Mountain
22.7	R		MATUYAMA
23.1	R?		
TD	I		

Notes: Magnetic polarity reversal time scale of Berggren et al. (1985a, 1985b), with Cobb Mountain subchron age from Clement and Robinson (1987). Chron names in capital letters, and subchrons in lowercase letters. N = normal, I = intermediate, and R = reversed. Heavy line indicates polarity chron boundary, and thin line indicates subchron boundary. TD = total depth.

A

Sample 135-838A-1H-2, 135–137 cm
(0–100 mT)



B

Sample 135-838A-4H-6, 60–62 cm
(0–30 mT)

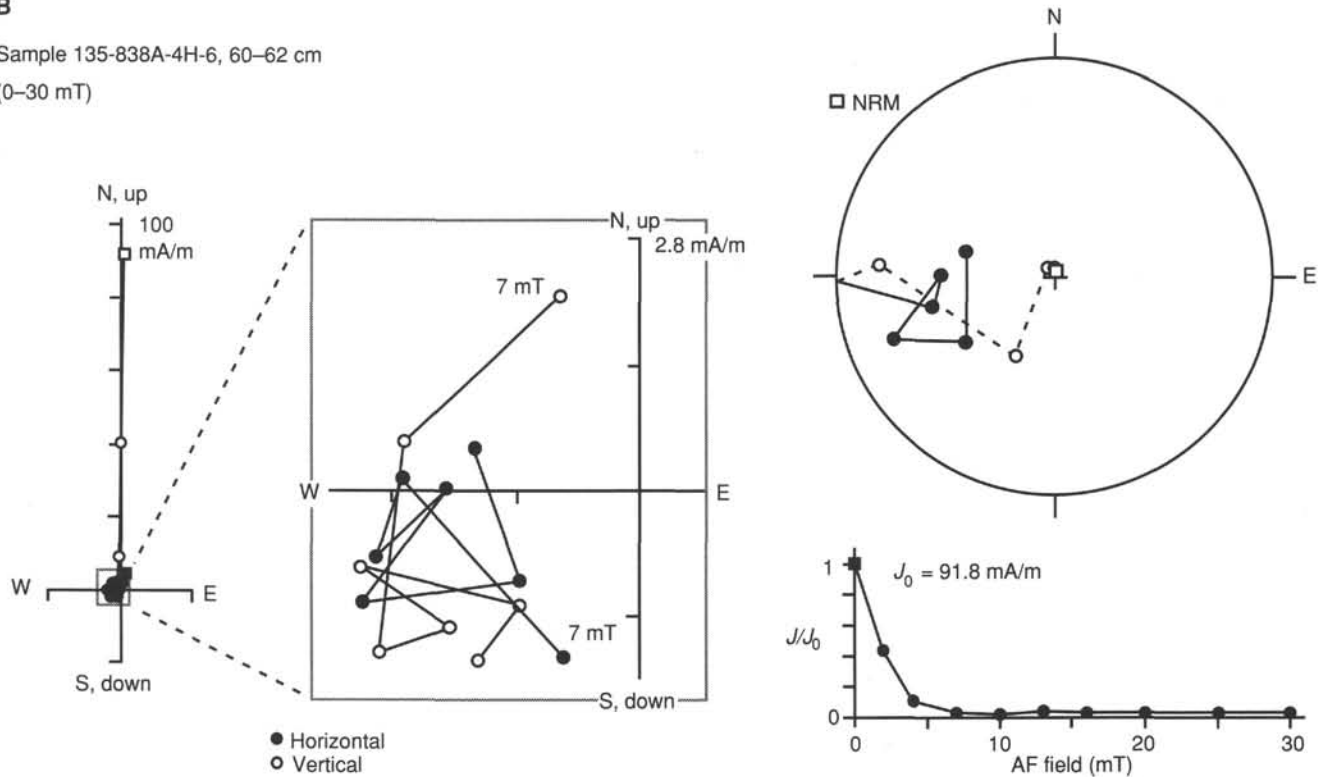


Figure 23. Behavior of Hole 838A sediment samples during AF demagnetization. **A.** Sample with stable characteristic remanence direction. **B.** Sample without stable characteristic remanence direction. For each sample, the following plots are given: upper right = equal-area stereogram of magnetization vector directions, lower right = normalized magnetization plot illustrating reduction of magnetization during AF demagnetization, and left = orthogonal vector diagrams of magnetization vector endpoints.

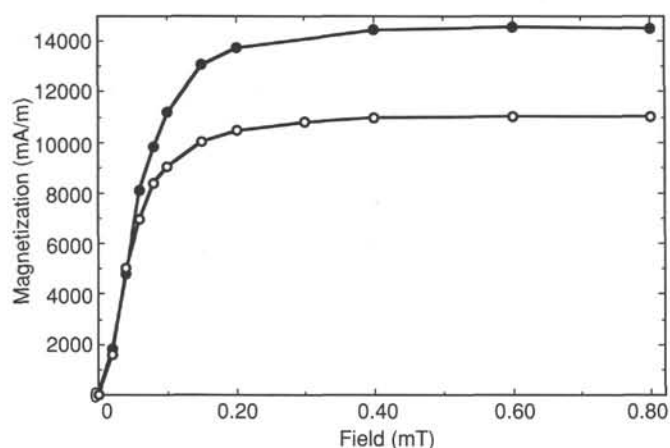


Figure 24. Acquisition of IRM for two Hole 838A sediment samples. Both display rapid, magnetite-type saturation in low applied magnetic fields. Filled circles = Sample 135-838A-4H-6, 60–62 cm, and open circles = Sample 135-838A-1H-2, 135–137 cm.

tometer by themselves were not considered reliable indicators of polarity at this site. Moreover, the magnetic declinations of the cores below Core 135-838A-3H were rarely consistent, so they also could not be used to determine polarity unambiguously.

Magnetic Susceptibility

Volume magnetic susceptibility values from Hole 838A cores ranged from about 20×10^{-6} to 2000×10^{-6} cgs and displayed complex variations downhole (Fig. 27). In general, the susceptibility displayed a good correlation with the sedimentary units (see "Lithostratigraphy" section, this chapter). In Unit I, which consists primarily of nannofossil ooze, the susceptibility is low and decreases slightly downward from 1×10^{-4} to 5×10^{-5} cgs. It displays a rapid, monotonic increase with depth to 560×10^{-6} cgs in Subunit IIA, a layer containing vitric sand. However, large and small susceptibility variations within the other units imply further subdivisions.

Within Subunit IIB there are three different susceptibility signatures: (1) high and scattered values in the upper part, associated with clayey nannofossil ooze, (2) moderate and more uniform values in the middle corresponding to the upper part of a vitric gravel layer, and (3) low values that increase downward in the lower part of the same vitric gravel layer (Fig. 27). Subunit IIC consists mainly of a single vitric sand and gravel layer, yet its susceptibility increases by an order of magnitude from 42 to 50 mbsf, perhaps implying preferential settling of the magnetic minerals (see "Lithostratigraphy" section, this chapter). From 50 to 54 mbsf, the susceptibility dips markedly, but it is relatively constant at the bottom of the unit (from 54 to 66 mbsf). Subunit IID appears to show two subunits that give downward-increasing susceptibility signatures (Fig. 27), perhaps implying two turbidites. Finally, Subunit IIE, consisting of coarse vitric sand and gravel, has relatively constant susceptibilities of about 300×10^{-6} cgs, but displays several small intra-unit variations that suggest further subtle sedimentary subdivisions.

Few susceptibility values were obtained from Unit III, the poorly recovered sedimentary section beneath that cored with the APC. Susceptibility values in this unit ranged from 50×10^{-6} to 600×10^{-6} cgs, similar to those in the sediments above. Likewise, poor recovery also resulted in few susceptibility readings being obtained from Hole 838B. They show a range of 11×10^{-6} to 160×10^{-6} cgs at depths of 228–250 mbsf.

Core Orientation

The multishot orientation tool was used with Cores 135-838A-4H through -8H. No data were obtained for Cores 135-838A-7H and -8H because the film in the multishot camera failed to advance. Orientations for the other cores are given in Table 7.

INORGANIC CHEMISTRY

Sediments recovered from Hole 838A are characterized by two main lithologies: clayey nannofossil oozes and volcanic turbidites comprising vitric sand and vitric gravel (see "Lithostratigraphy" section, this chapter). Only four interstitial waters samples were collected in Hole 838A; three of them were sampled in the uppermost 32 mbsf of clayey nannofossil ooze (Cores 135-838A-2H, -3H, and -4H), and the fourth was collected in Core 135-838A-8H from an interbedded clayey nannofossil ooze layer in volcanic turbidites. Standard ODP squeezing techniques were used for the removal of water samples (see "Explanatory Notes" chapter, this volume). Results are summarized in Table 8 and the variation of porewater chemistry with depth is shown in Figure 28.

In Hole 838A, dissolved major constituents (chloride, sodium, calcium, magnesium, potassium, and sulfate) were determined. Subsequent charge balance calculations yielded sodium concentrations. Ammonia, phosphate, silica, strontium, and manganese were also conducted using colorimetric methods and flame atomic adsorption spectrophotometry.

Chemical Components

In Hole 838A, porewater chloride, sodium, sulfate, and strontium concentrations are indistinguishable from the average seawater concentration (Broecker and Peng, 1982; Fig. 28). Na^+ concentrations were obtained from charge balance calculations. Values of dissolved ammonia and phosphate concentrations in pore waters from Hole 838A are comparable to those obtained in samples from the other Leg 135 sites and are consistent with the sulfate data (Fig. 28).

The concentration-depth profiles of dissolved calcium and magnesium show slight deviations with depth from the average seawater composition (Broecker and Peng, 1982; Fig. 28). From the mudline to 67 mbsf, these deviations include a relative depletion in magnesium concentration of about -4.4 mM and an relative increase in calcium concentration of about $+4.5$ mM. This scatter of data is greater than the analytical error, and there are linearly correlated concentration changes in calcium and magnesium. These changes follow the relationship $\Delta\text{Ca}/\Delta\text{Mg} = -0.94 \pm 0.09$ (the Δ concentration used is $\Delta = \text{porewater concentration} - \text{standard seawater concentration}$). A linear $\Delta\text{Ca}-\Delta\text{Mg}$ correlation (Fig. 29) implies conservative behavior, at least over the thickness of the sedimentary column studied (McDuff, 1981). Hence, data on the distribution of the calcium and magnesium in the interstitial waters suggest that reactions involving alteration of the underlying layer 2 of the oceanic crust have been responsible for the observed concentration changes, as is also recorded at many other DSDP/ODP sites (Gieskes et al., 1975; Kastner and Gieskes, 1976; McDuff and Gieskes, 1976; Gieskes and Lawrence, 1981). The absence of a sulfate concentration gradient suggests that the slight increase in alkalinity with depth is completely independent of the bacterially mediated sulfate reduction (Fig. 28), and could also be related to the basalt hydrolysis processes. The downhole temperatures between 30 and 70 mbsf (ranging from 2.5° to 6°C ; see "Physical Properties" section, this chapter) are probably too low to consider the volcanic turbidites as the source for Ca and as the sink for Mg. However, this hypothesis has to be confirmed by $\delta^{18}\text{O}$ and $^{87}\text{Sr}/^{86}\text{Sr}$ determinations from shore-based laboratories. The nature of the dissolved potassium profile (Fig. 28) implies an

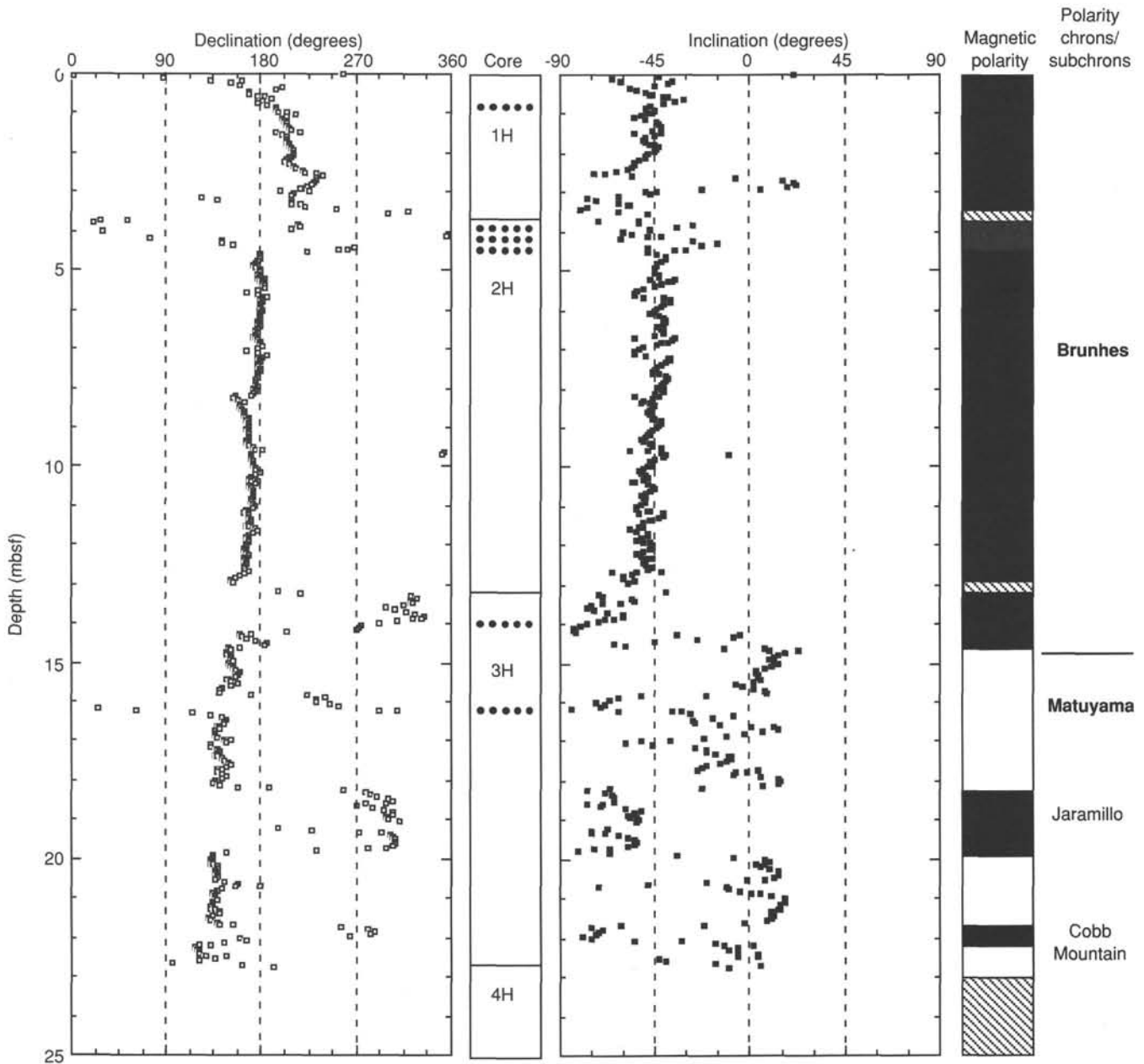


Figure 25. Magnetic polarity stratigraphy of the upper 25 mbsf of Hole 838A. Wide columns at left and middle show magnetic declination and inclination, respectively, measured with the pass-through cryogenic magnetometer after AF demagnetization at 15 mT. Column between declination and inclination plots indicates core boundaries and sections of disturbed core (filled circles). Columns at right indicate magnetic polarity interpretation (black = normal, dark stipple = probably normal, hachure = indeterminate, and white = reversed); see Table 6. At far right, interpreted magnetic polarity chrons and subchrons are indicated. Bold type denotes polarity chron names and lines show polarity chron boundaries. Plain type indicates subchron names.

almost linear $\Delta Ca-\Delta K$ relationship, and is probably also related to the alteration of volcanic material in the upper crust.

Dissolved silica concentrations increase gradually with depth to reach a maximum value of about $610 \mu M$ at 28.7 mbsf (Fig. 28). This Si concentration is the highest value yet determined for Leg 135. The silica concentration remains constant, toward the bottom of the hole, in the ooze interbedded with the volcanoclastic sediments. The increase in silica with depth, therefore, could be related to the occurrence in this hole of thick vitric sands and gravels (see "Lithostratigraphy" section, this chapter).

The manganese concentration-depth profile for Hole 838A (Fig. 28) shows an increase with depth. From the mudline to 66.7 mbsf, however, the Mn maximum (about $55 \mu M$) was reached at 19 mbsf in the upper nannofossil ooze unit, and as mentioned for the previously studied holes, suggests a release of manganese by diagenetic processes in the sedimentary column. Below this depth, a slight decrease is observed in the vicinity of the volcanic turbidite unit. Mn decreases to low values near the boundary between hemipelagic sediment and basalt, and within volcanoclastic sediments. This is a general pattern which has also been

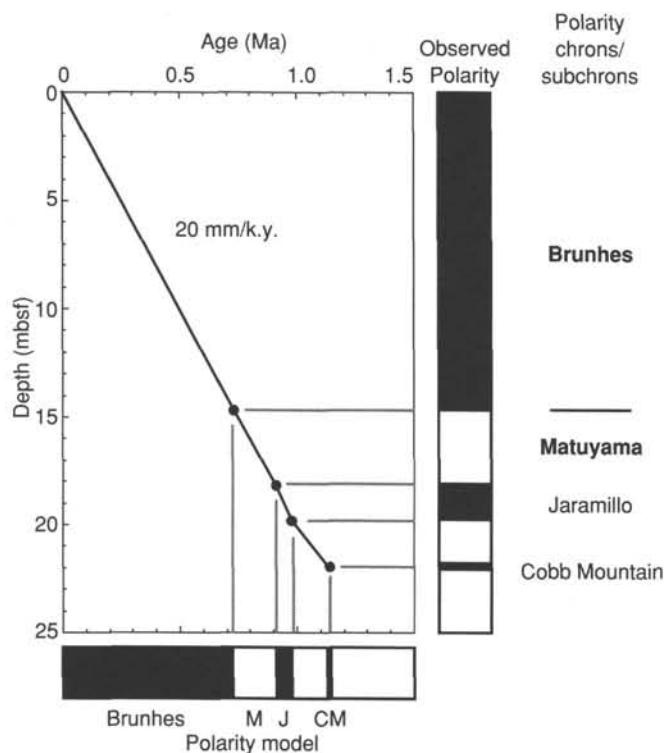


Figure 26. Age vs. depth, Hole 838A, derived from magnetic polarity stratigraphy. Polarity reversal model is derived from Berggren et al. (1985a, 1985b) with the addition of the Cobb Mountain Event at 1.12 Ma taken from Clement and Robinson (1987).

Table 7. Magnetic polarity zones, Hole 838A.

Core no.	Camera no.	Compass	Inclination		Declination
			Direction	Drift	
135-838A-					
5H	3250	B	N25°E	0.8°	295°
6H	3250	B	330°	0.5°	95°
7H	3209	A		No data	
8H	3209	A		No data	

Notes: Magnetic inclination at the site was 13°E. Compass B was misaligned; to correct its declination values, add 13°. Inclination is the off-vertical angle of the core; drift and direction are the dip angle and dip direction measured clockwise from north of a plane perpendicular to the core axis. Declination is the angle between the double line on the core liner and magnetic north (measured clockwise).

observed in Holes 834A, 835A, and 836A. This feature could be related to advection of seawater to the basalt below the sediment cover. The temperature gradients observed in Hole 838A (see "Physical Properties" section, this chapter) suggest that low

Table 8. Interstitial water chemistry data, Hole 838A.

Core, section, interval (cm)	Depth (mbsf)	pH	Alkalinity (mM)	Salinity	Ca ²⁺ (mM)	Mg ²⁺ (mM)	K ⁺ (mM)	Cl ⁻ (mM)	SO ₄ ²⁻ (mM)	NH ₄ ⁺ (μM)	PO ₄ ³⁻ (μM)	Si ⁴⁺ (μM)	Si ²⁺ (μM)	Mn ²⁺ (μM)	Na ⁺ (mM)
135-838A-															
2H-4, 140-150	9.0	7.58	2.588	35.2	10.5	53.8	11.6	548	27.9	15	2.7	291	98.3	23.2	464
3H-4, 140-150	19.0	7.44	2.943	35.2	11.6	52.7	9.8	548	28.4	15	2.2	358	101.5	55.3	466
4H-4, 140-150	28.7	7.37	2.959	35.5	13.5	50.3	10.4	551	28.1	16	2.0	610	99.8	49.2	467
8H-4, 140-150	66.7	7.52	3.084	35.8	15.0	49.6	9.2	553	28.9	16	1.6	608	97.3	54.3	470

amounts of seawater circulate throughout the sedimentary column. During this time, the circulating fluid undergoes only minor changes in major element concentration, such as seen in the Ca and Mg concentrations. Trace metals such as Mn are more useful than the major elements for discriminating between dilution effects and porewater-solid phase exchange. Therefore, the elevated Mn concentrations with depth imply a Mn source below the sediments, most likely in the unsampled basement. This hypothesis must be tested by further analyses of trace elements and isotopes in shore-based laboratories.

Conclusions

In Hole 838A, the interstitial water chemistry shows a low gradient in the concentration-depth profiles of dissolved calcium and magnesium which can be related to a diffusive exchange with the basement rock assumed to be the underlying layer 2 of the oceanic crust. This conclusion is also supported by the Mn distribution. In addition to indicating a source of Mn, plausibly located in layer 2 of the oceanic crust, the scatter in the Mn data also reveals a feature shown at previous sites, namely a downwelling flow of bottom seawater to the hemipelagic sediment-basement boundaries. At Hole 838A, however, the flow rate could be lower than that predicted at the previously studied sites. This is supported by the higher temperature gradient measured in Hole 838A ($\Delta T = 87^\circ\text{C}/\text{km}$; see "Physical Properties" section, this chapter).

ORGANIC GEOCHEMISTRY

Shipboard organic geochemical analysis of samples from Hole 838A consisted of four determinations of volatile hydrocarbons in sediments using the Carle gas chromatograph, nine determinations of total nitrogen, carbon, and sulfur using the Carlo Erba NCS analyzer, and 23 determinations of total inorganic carbon using the Coulometrics 5011 coulometer equipped with a System 140 carbonate/carbon analyzer. Details of the analytical procedures used are outlined in the "Organic Geochemistry" section, "Explanatory Notes" chapter (this volume) and are described in detail by Emeis and Kvenvolden (1986).

The volatile hydrocarbon gases were obtained from the bulk sediment using the headspace sampling technique and were routinely monitored for methane, ethane, and propane. One sample was taken from each of Cores 135-838A-2H to -4H and from Core 135-838-8H. Methane concentrations in all of the samples were between 2 and 3 ppm, which is very low and at the laboratory background level. Ethane and propane were not detected. The extremely low concentration of methane indicates that methanogenesis is not occurring in these sediments. As was the case at Site 837, a significant contributing factor could be the very low levels of organic carbon (see below) in these sediments, which are probably not enough to sustain microbial activity.

Determinations of inorganic carbon (IC) contents were performed on the samples used for physical properties and on additional samples selected by the sedimentologists. The percentage of CaCO₃ is calculated according to the equation:

$$\text{CaCO}_3 = \text{IC} \cdot 8.334.$$

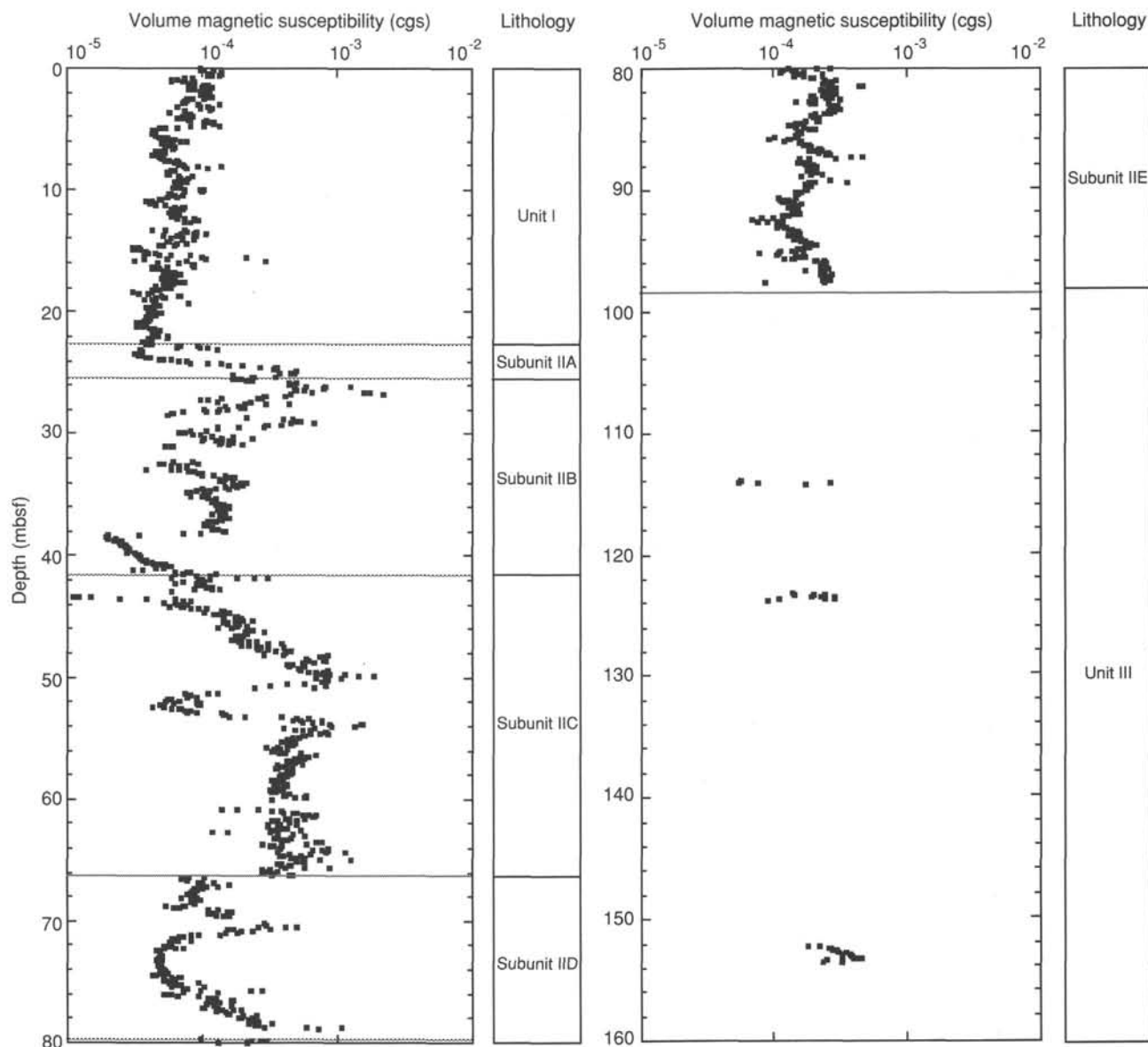


Figure 27. Volume magnetic susceptibility vs. depth, Hole 838A. Susceptibility is plotted on a logarithmic scale to highlight small variations. Lithologic units are shown in right-hand column (see “Lithostratigraphy” section, this chapter).

This equation assumes that all the carbonate is present as calcite. The data from these analyses are presented in Table 9. Carbonate values range from less than 0.2% to 62.1%. Lithologic Unit I shows values between 37% and 62%, whereas lithologic Unit II, which is dominated by vitric volcanic sands, shows much lower carbonate values except where the occasional interval of nannofossil ooze was present. This is discussed in more detail in the “Lithostratigraphy” section (this chapter).

Also shown in Table 9 are the percentages of total carbon and sulfur for the samples measured. The nitrogen content was also measured but not detected in any of the samples analyzed. Sulfur was detected in only two of the samples analyzed and then in very low amounts. Total organic carbon (TOC) is defined here as the difference between the total carbon and the inorganic carbon values. The sediments from Site 838 have organic carbon contents between 0.00% and 0.11% and hence were considered too low for analysis by the Rock-Eval instrument. These are the lowest set of values obtained for any hole to date on Leg 135 and reflect the

very high contribution of volcanoclastic material to the sediments recovered from Site 838A.

IGNEOUS PETROLOGY

Although igneous basement was not reached at Site 838, a variety of igneous materials were recovered as clasts and grains in sedimentary deposits. The most prominent of these sedimentary occurrences were 1.7 m of volcanic gravel recovered from Hole 838A and four relatively large (to 4 × 8 cm) angular pebbles of aphyric to sparsely phyrlic clinopyroxene-plagioclase basaltic andesite from Core 135-838B-4R. Sediments were recovered in cores above and below Unit I, but the four cores immediately below were empty.

The downhole logging results in Hole 838B show no pronounced discontinuities in density, resistivity, or chemistry, as might be expected for basaltic flows or sills interlayered with sediments. Core 135-838B-4R is only 8 m below the basaltic gravel recovered in Core 135-838A-20H; these data and the log-

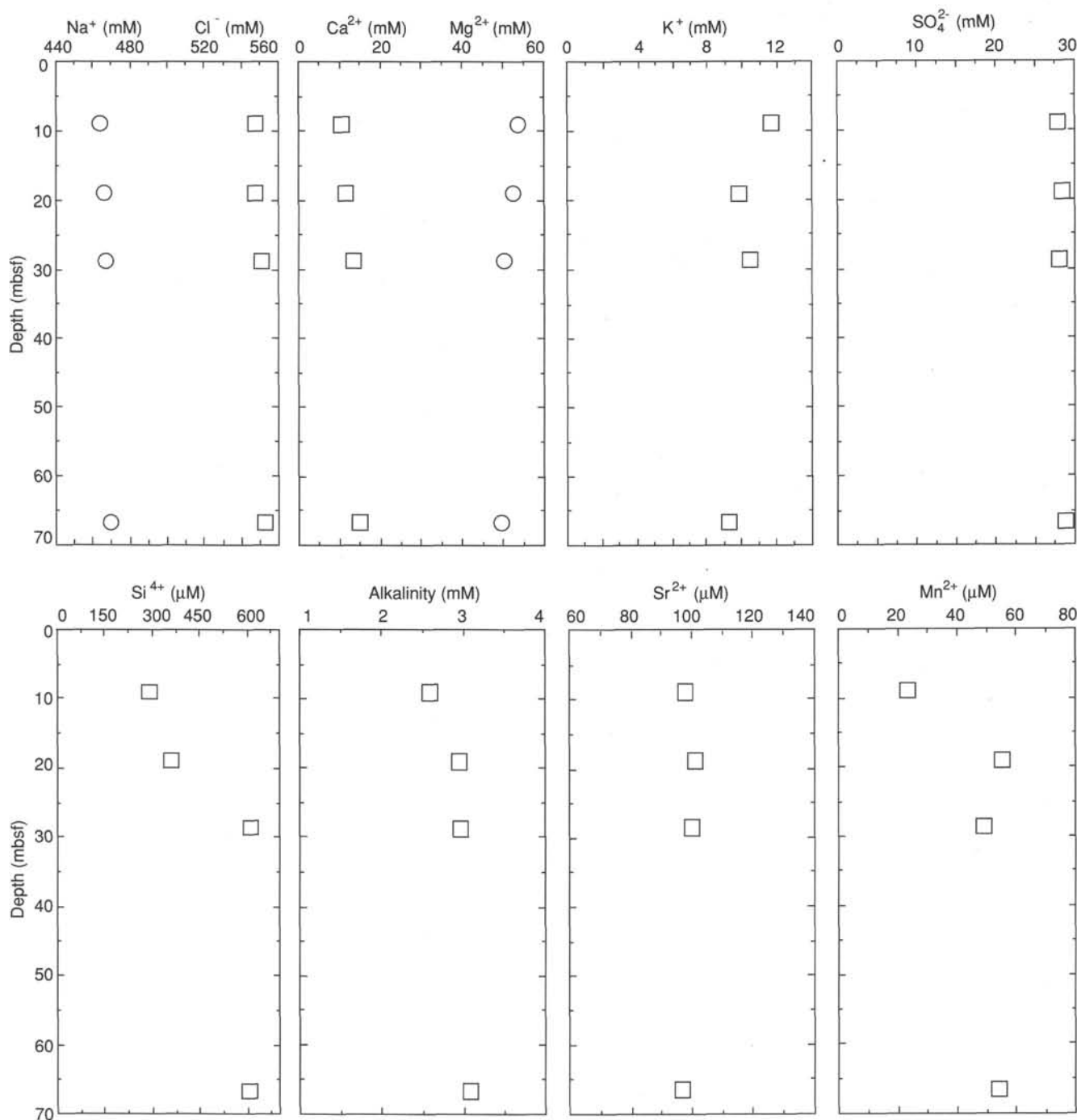


Figure 28. Concentration vs. depth profiles for chloride and sodium, calcium and magnesium, potassium, sulfate, silica, alkalinity, strontium, and manganese, Hole 838A.

ging results suggest that the larger basalt clasts may be derived from that gravel or from a similar deposit. We have concentrated our analytical efforts on these clasts because of their larger size.

Lithology and Petrography

The volcanic pebbles from Core 135-838B-4R are highly vesicular, aphyric to sparsely phyric clinopyroxene-plagioclase basaltic andesites. The four pieces vary significantly in their vesicularity, from spongy, finely vesicular samples (40%–60% vesicles)

to samples with only 10% vesicles (up to 2.5 mm in diameter). All are quite fresh except for various surface coatings and vesicle fillings.

Thin sections of two of the highly vesicular pieces have 1%–2% small (<1 mm) plagioclase phenocrysts as individual crystals and forming phenocrysts. Melt inclusions are common in the plagioclase. Clinopyroxene occurs as small (<0.5 mm) single crystals and in glomerocrysts with plagioclase. One of these phenocrysts has a large melt inclusion. The samples have a cryp-

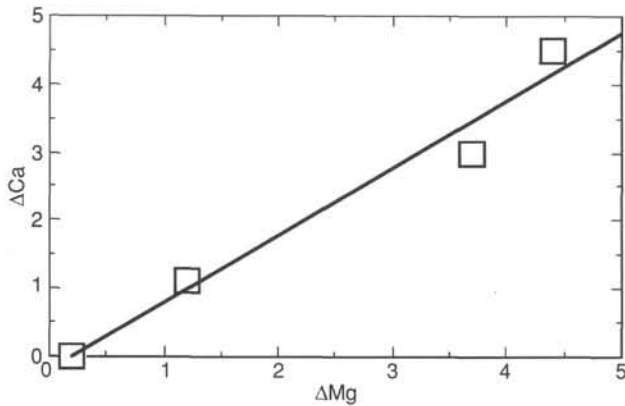


Figure 29. Relationship between Mg losses and Ca gains. The Δ concentration used is Δ = pore-water concentration/standard seawater concentration. The regression line equation is $y = -0.19 + 0.98x$, with a correlation coefficient $R = 0.971$.

to crystalline to variolitic mesostasis which is fresh to partially altered fine-grained aggregates of clay.

The most notable feature of the samples is the occurrence of lithic inclusions in the largest of the basaltic andesite pieces from Core 135-838B-4R (Fig. 30). These inclusions are angular, from 1 to 10 mm in size, and constitute 1%–2% of the rock. The included fragments are aphyric with intergranular to intersertal textures, abundant interstitial magnetite, and have a mesostasis partially to extensively replaced by clays.

Volcanic clasts from the sedimentary units recovered from Hole 838A include pumice with sparse plagioclase phenocrysts (Sections 135-838A-6H-4, 13–15 cm, and -8H-1, 137–140 cm), moderately phyrlic olivine-plagioclase basalt (Section 135-838A-9H-2, 95–117 cm), and sparsely phyrlic clinopyroxene-plagioclase basalt with pilotaxitic textures and traces of magnetite and olivine (Section 135-838A-20H-CC, 0–10 cm). The pumice from Section 135-838A-8H-1 has trace amounts of quartz (≤ 0.5 mm) and amphibole phenocrysts (< 0.6 mm).

Alteration

The outer surfaces of all hand specimens in Core 135-838B-4R have vesicles filled with coarse-grained, slightly brownish white quartz. Some of the quartz has a striated, cleaved form. The X-ray diffraction pattern of material hand-picked from the vesicles shows peaks characteristic of quartz as well as some weak plagioclase peaks. Quartz has also been identified optically in cavities. The plagioclase identified from the X-ray diffraction pattern is thought to be a contamination from the whole-rock sample.

Brown to yellowish calcite occurs in a fracture together with a harder, brittle, yellow mineral and, rarely, with clear zeolite crystals. In addition, in two places on the outer surfaces of samples, there is a thin layer of a white amorphous mineral or mineraloid. A similar material occurring as round patches (about 3 to 4 mm in diameter), also observed on the outer surface of samples, may consist of amorphous silica (opal?). The presence of cryptocrystalline silica is indicated by the broad hump appearing in the X-ray diffractogram at 20° – 30° 2θ .

Geochemistry

Three samples were analyzed for major and trace elements by XRF. These are a plagioclase-phyric basaltic andesite from Section 135-838B-4R-1, a representative mix of cleaned pumice clasts from Section 135-838A-7H-4, and a mix of hand-picked glassy grains from a coarse vitric sand in Section 135-838A-9H-2. The analyses are given in Table 10.

All of the samples have low Ni and Cr, TiO_2 less than 1%, and high ratios of incompatible large-ion-lithophile to high-field-strength elements. Ba/Zr, for example, is quite constant for the three samples (about 2) and is higher than other samples from Sites 834 to 837 (Fig. 31A). The Site 838 Ba/Zr is much higher than Ba/Zr in the transitional type (Ba/Zr = 0.3 to 0.9) and arc-type (Ba/Zr = 0.7–0.9) Lau Basin basalts identified by Hawkins and Melchior (1985).

The pumice is a low-potassium rhyolite (Table 10) and is similar in major element chemistry to rhyolitic glasses described from Metis Shoal in the Tonga Arc and Zephyr Shoal in the Lau Basin (Fig. 31B; Hawkins, 1985). The Site 838 pumice has,

Table 9. Concentrations of inorganic and organic carbon and total sulfur, Hole 838A.

Core, section interval (cm)	Depth (mbsf)	Total carbon (%)	Inorganic carbon (%)	TOC (%)	CaCO_3 (%)	S (%)	OrgC/S
135-838A-							
1H-1, 78–79	0.78	4.56	4.53	0.03	37.7		
1H-1, 100–101	1.00		5.08		42.3		
1H-2, 74–76	2.24	5.67	5.64	0.03	47.0	0.14	0.21
1H-3, 17–18	3.17		6.81		56.7		
2H-2, 71–72	5.91		6.86		57.1		
2H-2, 86–87	6.06	6.26	6.20	0.06	51.6		
2H-4, 55–56	8.75		6.76		56.3		
2H-4, 70–71	8.90		6.06		50.5		
2H-6, 72–73	11.92		7.12		59.3		
2H-6, 84–85	12.04	6.92	6.84	0.08	57.0	0.29	0.27
3H-1, 74–75	13.94		7.46		62.1		
3H-4, 74–75	18.44		5.70		47.5		
3H-6, 70–71	21.40	7.45	7.45	0	62.1		
4H-4, 30–31	27.50		0.68		5.7		
4H-4, 75–76	27.95		3.59		29.9		
4H-6, 48–49	30.68	3.79	3.75	0.04	31.2		
6H-1, 65–66	42.35	7.05	7.00	0.05	58.3		
7H-2, 71–72	53.41		0.07		0.6		
7H-4, 69–70	56.39		0.03		0.2		
7H-6, 79–80	59.49		0.03		0.2		
8H-3, 6–7	63.76	1.13	1.12	0.01	9.3		
8H-4, 115–116	66.35		6.35		52.9		
8H-6, 100–101	69.20	2.32	2.21	0.11	18.4		

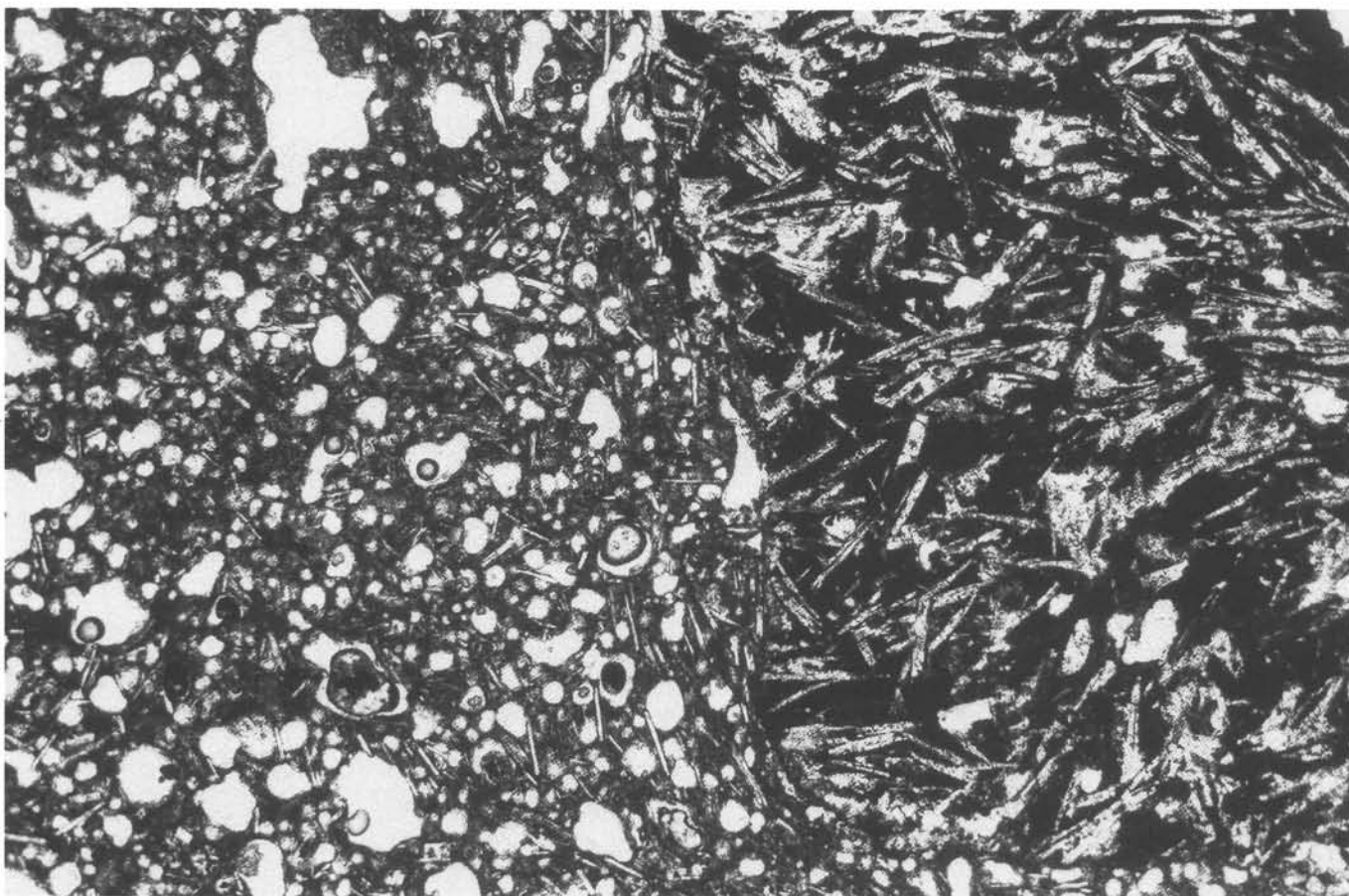


Figure 30. Basaltic lithic fragment (less vesicular area with dark, altered mesostasis) enclosed in a basaltic andesite pebble, Sample 135-838B-4R-1, 0–2 cm; field of view = ~3 mm, plane polarized light.

however, much lower Ba and higher Zr and Y than the Metis Shoal dacites (Ewart, 1979); its trace element abundances are more similar to pumices dredged from the Tonga Ridge (254 ppm Ba, 170 ppm Sr, 49 ppm Y, 145 ppm Zr; Hawkins, 1985). It should be noted that there is a large range reported for trace element concentrations in siliceous glasses from the Tonga Ridge (for example, Ba from 250 to 600 ppm, Zr from 47 to 90 ppm; Hawkins, 1985) and single analyses may not be particularly representative.

The glass-rich sand from Section 135-838A-9H-2 is derived from a moderately fractionated basalt (Table 10) with low concentrations of Y and Zr (17 and 40 ppm, respectively) and Ba/Zr of 1.9. These abundances are as low as those reported for lavas from the active Tonga and Kermadec arcs (Fig. 31C).

Sample 135-838B-4R-1, 0–4 cm, is a basaltic andesite. It has incompatible element ratios similar to those of the basalt from Section 135-838A-9H-2. These two samples have very low Ce abundances and high Ba/Ce, both of which are characteristic of lavas from the active Tofua and Kermadec arcs (Ewart and Hawkesworth, 1987).

PHYSICAL PROPERTIES

A full suite of standard ODP physical properties measurements was made at Site 838. Index properties on sediments and sedimentary rocks from Holes 838A and 838B were determined by using a pycnometer and balance, and include bulk density, grain density, porosity, water content, and void ratio. Bulk density was also measured using the continuous gamma-ray attenuation porosity evaluator (GRAPE) on full APC cores from Hole 838A.

Compressional wave velocities were measured both on whole cores using the continuous *P*-wave logger and on discrete samples using the Hamilton Frame apparatus. Velocities of unconsolidated sediments that could not be removed from the core liner were measured in only one direction. Velocities were measured in both horizontal and vertical directions when possible in unconsolidated sediments and on many of the consolidated sedimentary rocks.

Vane shear strength was measured on selected undisturbed intervals of fine-grained sediments from Hole 838A until the sediment became too stiff for valid measurements (when cracking of the sediment indicated that the assumption of uniform shear by the vane was no longer valid).

Thermal conductivity was measured on undisturbed sediment cores from Hole 838A. Temperature measurements were obtained at two locations in the hole during drilling to measure the geothermal gradient and allow an estimate of heat flow.

The lithostratigraphic units referenced in this section are those described in the "Lithostratigraphy" (this chapter). Results from laboratory measurements are listed in Tables 11 and 12 and plotted in Figures 32 through 40.

Index Properties

Wet-bulk density, grain density, porosity, water content, and void ratio for sediments and sedimentary rocks from Holes 838A and 838B are plotted vs. depth in Figure 32 and listed in Tables 11 and 12.

For all the index properties, large variations are seen in the measured values for the upper 100 m of the hole; this variation is

Table 10. Major and trace element analyses for representative samples from Site 838.

Hole	838A	838A	838B
Core	7H-4	9H-2	4R-1
Interval (cm)	0-57	95-117	0-4
Depth (mbsf)	55.70	72.65	163.20
Major elements (wt%):			
SiO ₂	72.08	52.14	57.01
TiO ₂	0.58	0.81	0.94
Al ₂ O ₃	13.12	16.23	16.15
Fe ₂ O ₃	3.45	11.31	10.29
MnO	0.14	0.22	0.19
MgO	0.94	5.63	3.48
CaO	3.02	11.13	7.63
Na ₂ O	4.27	1.54	3.23
K ₂ O	1.52	0.30	0.46
P ₂ O ₅	0.12	0.10	0.18
Total	99.21	99.42	99.54
LOI	5.29	0.62	3.33
Mg#		49.6	40.1
Trace elements (ppm):			
Nb	3	1	1
Zr	145	40	74
Y	49	17	33
Sr	176	199	191
Rb	22	6	5
Zn	56	74	97
Cu	10	147	41
Ni	1	18	7
Cr	0	21	0
V	29	373	229
Ce	33	13	4
Ba	270	76	147
Ba/Ce	8.2	5.8	36.7
Ba/Zr	1.9	1.9	2.0
Y/Zr	0.34	0.43	0.45

Notes: Mg# represents $100 \cdot [\text{Mg}/(\text{Mg} + \text{Fe}^{+2})]$, where $\text{Fe}^{+3}/\text{Fe}^{+2}$ is assumed to be 0.2. Mg# was not calculated for samples with $\text{SiO}_2 > 65\%$. LOI = loss on ignition.

caused by interbedded lithologies which range from nannofossil ooze to very coarse vitric (pumiceous) gravel. However, unlike Sites 834 through 837, the index properties show trends with depth that are expected within a section undergoing consolidation. Thus, the bulk density increases, and porosity, water content, and void ratio all decrease with increasing depth. Details of the index properties in the first 100 mbsf are shown in the GRAPE data and are discussed later. Below 100 mbsf, samples were recovered only sporadically during coring and index property determinations are sparse.

The general trend of bulk density (Fig. 32) is an increase from about 1.4 g/cm³ at the top of the hole to an average value of about 1.6 g/cm³ at 100 mbsf. The few samples acquired between 100 and 150 mbsf show a sharply increasing density, to between 2.0 and 2.4 g/cm³ at 150 mbsf.

The grain density values (Fig. 32) are highly variable, reflecting the considerable variation in sediment composition. Low grain densities of 2.2 to 2.4 g/cm³ at around 50 and 90 mbsf were measured from the vitric sand and gravel, grain densities in the range of about 2.5 to 2.7 g/cm³ were measured on nannofossil ooze and clayey nannofossil oozes, and grain densities around 2.7 g/cm³ and above were obtained from black vitric sands, especially around 70 mbsf. Grain density values measured on vitric

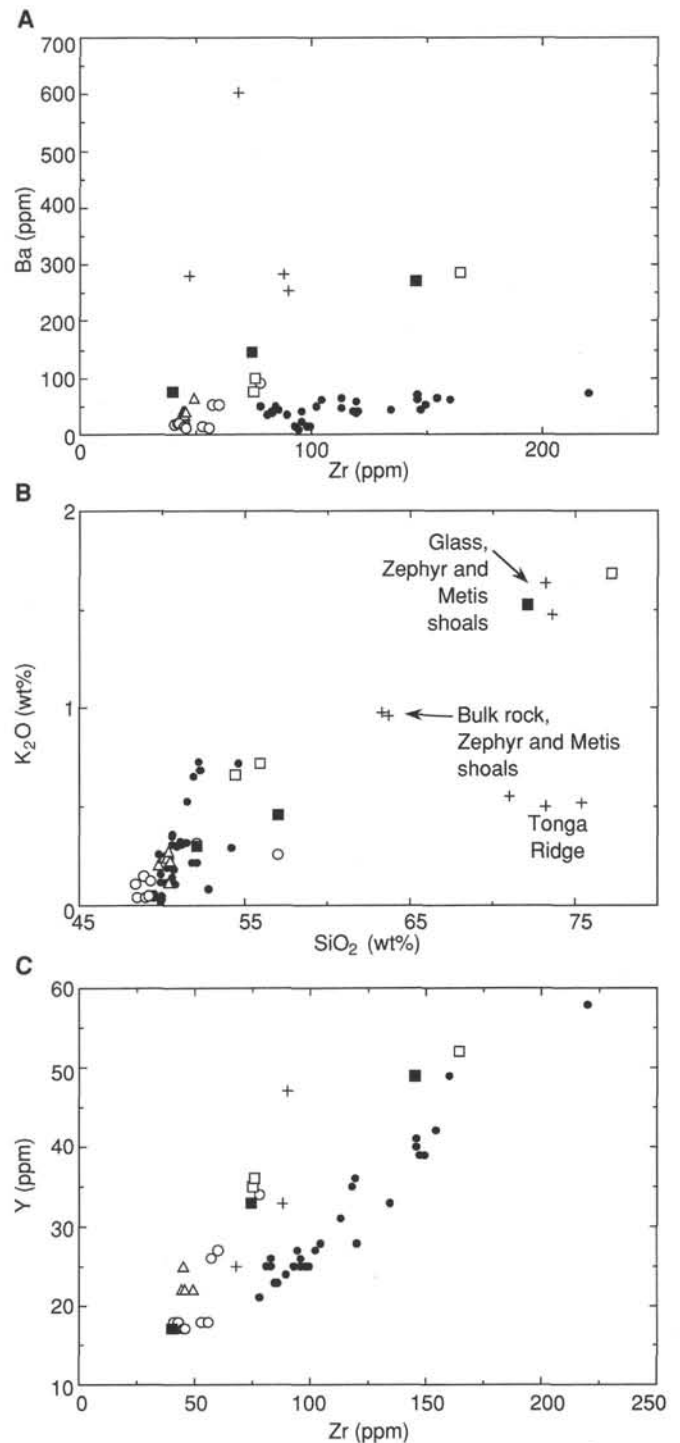


Figure 31. A. Ba vs. Zr for volcanic rocks from Leg 135. Pumice data include analyses from Metis Shoal, the Tonga Ridge, Fonualei, and an average for southwest Pacific rhyolitic pumices from Ewart (1979). B. K₂O vs. SiO₂ for Leg 135 samples. Pumice analyses for comparison are from the Tonga Ridge and Metis and Zephyr shoals (bulk rock and glass analyses) from Hawkins (1985). C. Y vs. Zr for Leg 135 samples. Pumice samples for comparison are for Tonga Ridge, Metis Shoal, and the average southwest Pacific low-K rhyolite from Hawkins (1985) and Ewart (1979). Plus signs = pumices, filled circles = Site 834 samples, open triangles = Site 835 samples, open circles = Site 836 samples, open squares = Site 837 samples, and filled squares = Site 838 samples.

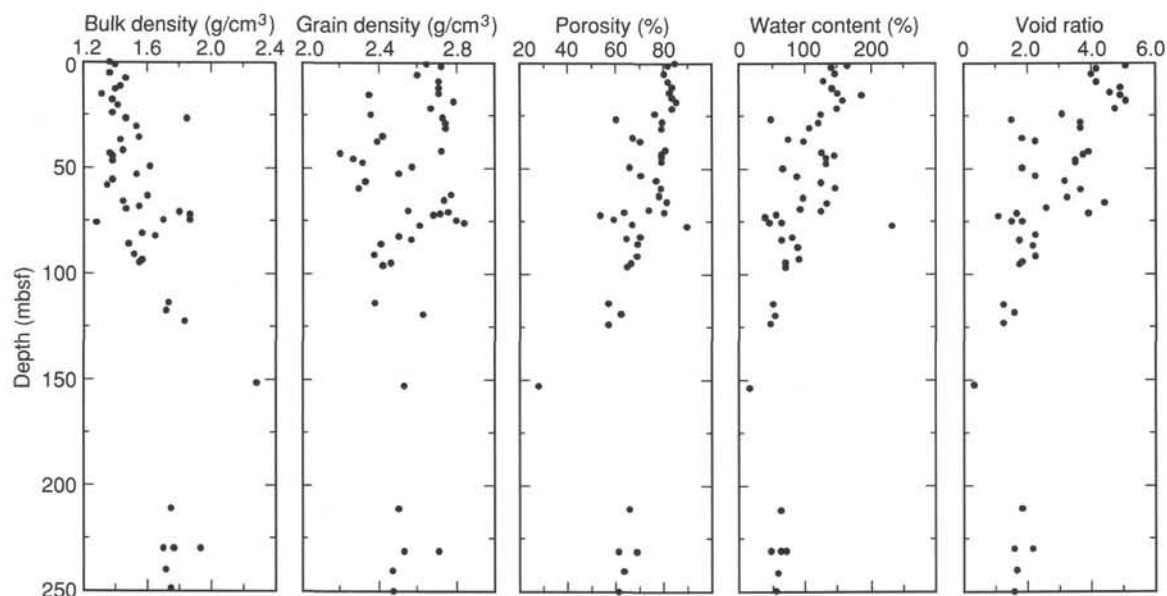


Figure 32. Index property data (bulk density, grain density, porosity, water content, and void ratio) vs. depth for the sedimentary section from Hole 838A.

siltstone, claystone, and conglomerate recovered between 150 and 250 mbsf are within the range of 2.45 to 2.7 g/cm³, comparable to the grain density range measured in the clayey nanofossil oozes from the upper part of the hole.

Porosity, water content, and void ratio (Fig. 32) all show significant decreases with depth, approaching very low values at 152.8 mbsf on the single discrete sample from that depth (to 28% porosity, 15% water content, and 0.4 void ratio; Tables 11 and 12). Below 200 mbsf, however, all three index properties increase noticeably.

All index values from the bottom of Hole 838B indicate a change in the rate of consolidation between 153 and 200 mbsf. Either little change in consolidation occurs from 153 mbsf to the base of the hole, or a decrease in the degree of consolidation occurs, as indicated by the markedly lower bulk densities, and higher porosity, water content, and void ratios below 200 mbsf as compared to values above 153 mbsf. The differences in the index properties suggest that the zone below 200 mbsf may be over-pressured, with high pore pressure preventing continued consolidation and lithification of the sediments at the bottom of the hole.

The GRAPE bulk density data (Fig. 33) have been processed and averaged at 5-cm intervals to remove spurious data points caused by core section ends and void spaces within the core. The 5-cm averaged data (Fig. 33A) have been further processed (Fig. 33B) by applying a 15-point averaging filter to the data to smooth the high variability of the initial data set. Discrete measurements of bulk density correspond extremely well with the GRAPE values (Fig. 33C) except in the upper 20 mbsf, where shipboard-measured values in the nanofossil ooze are about 0.5 to 0.75 g/cm³ lower than the GRAPE values. The marked variations in the GRAPE density values are more easily seen on the averaged data than on the original data set. The first 23 mbsf are marked by smoothly varying densities in the nanofossil ooze of lithologic Unit I. Generally high, variable density values between 26 and 42 mbsf correspond to interbedded black vitric sand and nanofossil ooze. Vitric sand and vitric gravel have slightly lower overall density values between 42 and 66 mbsf and between 80 and 95 mbsf. The high peak at about 71 to 76 mbsf corresponds to indurated clay and interbedded black vitric sand. The highest

measured densities in the upper 100 m of the section, between 1.8 and 1.9 g/cm³, are all from black vitric sand.

Compressional Wave Velocity

Compressional wave velocity data measured with a Hamilton Frame device and the *P*-wave logger are shown in Figures 34 and 35A–C and are listed in Tables 11 and 12.

The compressional wave velocity, like the index properties, increases with depth and exhibits a similar high degree of variability caused by the different lithologies (Fig. 34). The velocity in the upper part of the hole is around 1500 m/s, increasing to about 1800 m/s by 100 mbsf, and to around 2400 m/s by 123 mbsf. Velocity values below 200 mbsf, however, drop markedly to around 1900 to 2000 m/s. The decreasing velocity, as with the change in index properties, suggests that the lower part of the hole is underconsolidated.

The velocity variation in the upper part of the hole is shown in more detail in the *P*-wave logger data (Fig. 35A–C). The discrete velocities match the *P*-wave logger data well above 40 mbsf (Fig. 35C) and match *P*-wave values measured between 65 and 77 mbsf in nanofossil oozes. The high velocities (above 1650 m/s) of the discrete data set below 50 mbsf were all measured on samples of vitric sand and gravel. No values were measured for these units using the *P*-wave logger unit.

The velocities may be separated into fields of low and high velocity. Regions of nanofossil ooze have relatively low velocities (1500 to around 1600 m/s), particularly in the intervals from about 20 to 45 mbsf and 65 to 77 mbsf. Regions of vitric ash and gravel between 25 and 27 mbsf, 35 and 42 mbsf, and 50 and 60 mbsf have relatively high velocities (1600 to 1800 m/s with increasing depth). Thus, the nanofossil ooze behaves very much as seen at Sites 834–837, with only a slight increase in velocity downhole, whereas the vitric sand and ash respond with much more pronounced velocity increases with depth. The vitric sand and ash are commonly matrix-supported (see “Lithostratigraphy” section, this chapter); the increasing velocity is a result of increasing grain-to-grain contact with increasing overburden overpressure. The highest values from both *P*-wave logger and discrete sample velocity data sets occur between 72 and 76 mbsf; this

Table 11. Physical properties data, Hole 838A.

Core, section, interval (cm)	Depth (mbsf)	Su (kPa)	TC (W/[m · °K])	Bulk density (g/cm ³)	Grain density (g/cm ³)	Porosity (%)	Water content (%)	Void ratio	V _p (m/s)	V _p dir.
135-838A-										
1H-1, 60	0.60		0.8692							
1H-1, 99-100	0.99			1.37	2.63	84	167	5.1	1450	C
1H-1, 100-100	1.00	4.7								
1H-2, 60	2.10		0.8465							
1H-2, 73-74	2.23			1.41	2.72	81	142	4.2	1446	C
1H-2, 75-75	2.25	5.1								
1H-3, 25	3.25		0.8670							
2H-2, 60	5.80		0.8273							
2H-2, 70-72	5.90			1.38	2.60	80	146	4.0	1468	C
2H-2, 75-75	5.95	6.7								
2H-3, 60	7.30		0.9447							
2H-4, 60	8.80		0.8780							
2H-4, 70-72	8.90			1.47	2.70	81	129	4.2	1484	C
2H-4, 75-75	8.95	6.1								
2H-6, 60	11.80		0.9125							
2H-6, 70-72	11.90								1479	A
2H-6, 70-72	11.90								1456	A
2H-6, 70-72	11.90			1.45	2.70	83	143	4.9	1468	C
2H-6, 75	11.95	20.3								
3H-1, 70-72	13.90			1.41	2.70	82	148	4.6	1480	C
3H-1, 75	13.95	33.1								
3H-2, 60	15.30		0.8361							
3H-2, 75-77	15.45								1514	C
3H-2, 125-126	15.95			1.32	2.34	83	184	4.9	1543	C
3H-3, 60	16.80		0.9500							
3H-4, 60	18.30		0.8966							
3H-4, 70-72	18.40			1.40	2.77	84	159	5.1	1489	C
3H-4, 80	18.50	45.0								
3H-6, 60	21.30		0.9221							
3H-6, 70-71	21.40			1.42	2.66	83	149	4.8	1497	
3H-6, 75	21.45	52.3								
4H-2, 60	24.20		0.7733							
4H-2, 48-49	24.68			1.40	2.35	76	123	3.1		
4H-2, 70-73	24.90								1612	C
4H-3, 60	25.20		0.9491							
4H-4, 60	27.20		0.9042							
4H-4, 31-32	27.51			1.86	2.72	60	49	1.5	1605	
4H-4, 53-55	27.73								1503	C
4H-4, 71-73	27.91			1.47	2.73	79	122	3.7		
4H-4, 75	27.95	29.8								
4H-6, 60	30.20		0.9495							
4H-6, 50-51	30.70	100.4		1.54	2.73	79	110	3.7	1521	
5H-3, 73-75	35.93								1608	C
5H-3, 73-75	35.93								1621	C
5H-3, 74-75	35.94			1.55	2.41	66	78	1.9	1615	C
5H-4, 60	36.70		0.7585							
5H-4, 50-51	37.20			1.45	2.39	70	97	2.3	1684	
6H-1, 60	42.30		0.8503						1684	C
6H-1, 70-73	42.40			1.46	2.72	80	126	3.9	1476	
6H-1, 75	42.45	50.8								
6H-3, 60	43.80		0.6708							
6H-2, 70-73	43.90			1.37	2.20	79	144	3.8		
6H-4, 60	45.30		0.6934							
6H-3, 70-73	45.40			1.40	2.26	78	133	3.5		
6H-4, 87-90	47.07			1.40	2.30	78	133	3.5		
6H-6, 100	48.30		0.7984							
6H-6, 65-68	49.85			1.63	2.56	65	70	1.9	1693	
7H-2, 71-73	53.41			1.54	2.50	70	87	2.3	1700	
7H-4, 60	56.30		0.7773							
7H-4, 71-73	56.41			1.39	2.32	76	126	3.2	1726	
7H-5, 60	57.80		0.6168							
7H-6, 60	59.30		0.7207							
7H-6, 80-82	59.50			1.36	2.29	79	146	3.7	1739	
8H-2, 90	63.10		0.6755							
8H-3, 12-15	63.82			1.60	2.76	77	96	3.3		
8H-3, 15	63.85	79.5								
8H-3, 60	64.30		0.9750							
8H-4, 52	65.72		0.8822							
8H-4, 111	66.31	43.0								
8H-4, 111-114	66.31			1.46	2.73	81	134	4.4	1484	
8H-6, 37-39	68.57								1507	C
8H-6, 90	69.10		0.8771							
8H-6, 95	69.15	45.2								
8H-6, 97-100	69.17			1.55	2.54	73	92	2.6	1543	
9H-1, 60-62	70.80			1.47	2.70	80	124	3.9	1575	

Table 11 (continued).

Core, section, interval (cm)	Depth (mbsf)	Su (kPa)	TC (W/[m · °K])	Bulk density (g/cm ³)	Grain density (g/cm ³)	Porosity (%)	Water content (%)	Void ratio	V _p (m/s)	V _p dir.
135-838A- (cont.)										
9H-1, 139-141	71.59			1.81	2.74	63	55	1.7	1791	
9H-2, 60	72.30		0.7838							
9H-2, 80-92	72.50			1.87	2.68	53	41	1.1	1803	
9H-3, 60	73.80		0.9302							
9H-4, 41-43	75.11								2078	C
9H-4, 41-43	75.11								1909	A
9H-4, 60	75.30		0.8444							
9H-4, 64-65	75.34			1.87	2.78	59	48	1.5	1921	
9H-4, 70-71	75.40			1.70	2.83	66	66	1.9	1590	
9H-5, 95-98	77.15			1.30	2.61	89	234	7.9	1494	
9H-5, 100	77.20	40.8								
9H-6, 60	78.30		0.7061							
10H-2, 60	81.80		0.6686							
10H-2, 70-72	81.90			1.58	2.50	70	82	2.3		
10H-3, 60	83.30		0.8942							
10H-3, 65-67	83.35			1.65	2.56	64	66	1.8	1771	
10H-4, 60	84.80		0.7638							
10H-5, 68-70	86.38			1.50	2.40	69	90	2.2	1839	
10H-6, 60	87.80		0.8916							
11H-1, 60	89.80		0.7517							
11H-2, 88-90	91.58			1.52	2.37	69	88	2.3	1849	
11H-2, 100	91.70		0.8128							
11H-4, 60	94.30		0.7226							
11H-4, 74-76	94.44			1.58	2.46	65	73	1.9	1786	
11H-4, 123-125	94.93								1786	C
11H-5, 41-43	95.61			1.56	2.42	64	73	1.8	1841	
11H-6, 30	97.00		0.7663							
14X-1, 15-16	114.05			1.74	2.38	57	51	1.3	2265	
15X-CC, 2-5	118.52								2376	C
15X-CC, 15-16	118.65			1.73	2.62	62	58	1.6	2376	
16X-1, 5-6	123.20			1.84	5.68	57	46	1.3	2406	
20H-1, 70-72	152.80			2.28	2.52	28	15	0.4		

Notes: Su = undrained vane shear strength, TC = thermal conductivity, V_p = compressional (*P*-wave logger) velocity, and V_p dir. = velocity direction, where A is the vertical velocity along the core and C is the horizontal velocity perpendicular to the core face.

Table 12. Physical properties data, Hole 838B.

Core, section, interval (cm)	Depth (mbsf)	Bulk density (g/cm ³)	Grain density (g/cm ³)	Porosity (%)	Water content (%)	Void ratio	V _p (m/s)	V _p dir.
135-838B-								
9R-CC, 15-20	201.45						1921	C
9R-CC, 18-19	211.08	1.75	2.50	65.60	62.20	1.9		
11R-1, 10-11	230.30	1.70	2.52	69.20	71.60	2.2		
11R-1, 10-11	230.30	1.77	2.70	68.30	65.20	2.2		
11R-1, 15-16	230.35	1.93	2.53	61.30	48.20	1.6	1928	C
12R-1, 3-4	239.93	1.72	2.47	63.50	60.80	1.7	2008	C
13R-1, 9-10	249.59	1.75	2.47	61.40	55.90	1.6	1924	C
13R-1, 15-17	249.65						1922	C

Notes: V_p = compressional (*P*-wave logger) velocity, and V_p dir. = velocity direction, where C is the horizontal velocity perpendicular to the core face.

interval is formed of black vitric sand and interbedded, highly consolidated claystones.

Comparison of Density and Velocity with Lithology

The marked variations in density and velocity caused by the lithology can be seen in detail on the GRAPE and *P*-wave logger information above 100 mbsf, which is correlated with the lithology (Fig. 36). *P*-wave logger data is generally missing in areas where thick vitric gravel and sand were recovered (43 to 63 mbsf and below 78 mbsf), because of extreme attenuation of the sonic wave in the unconsolidated sediments. Areas of nannofossil ooze are marked by moderately low densities and velocities, whereas

the vitric gravel and sand layers are marked by intermediate densities. The high density and velocity peaks correspond to the black vitric sands at about 28 mbsf, and to interbedded black vitric sands and lithified claystones between 72 and 76 mbsf.

Undrained Vane Shear Strength

Values of undrained shear strength were obtained using the standard onboard miniature vane shear apparatus on unconsolidated sediments in Hole 838A; the results are plotted in Figure 37 and reported in Table 11. Measurements are made on representative sections of core, which means that the fine-grained matrix material is tested preferentially.

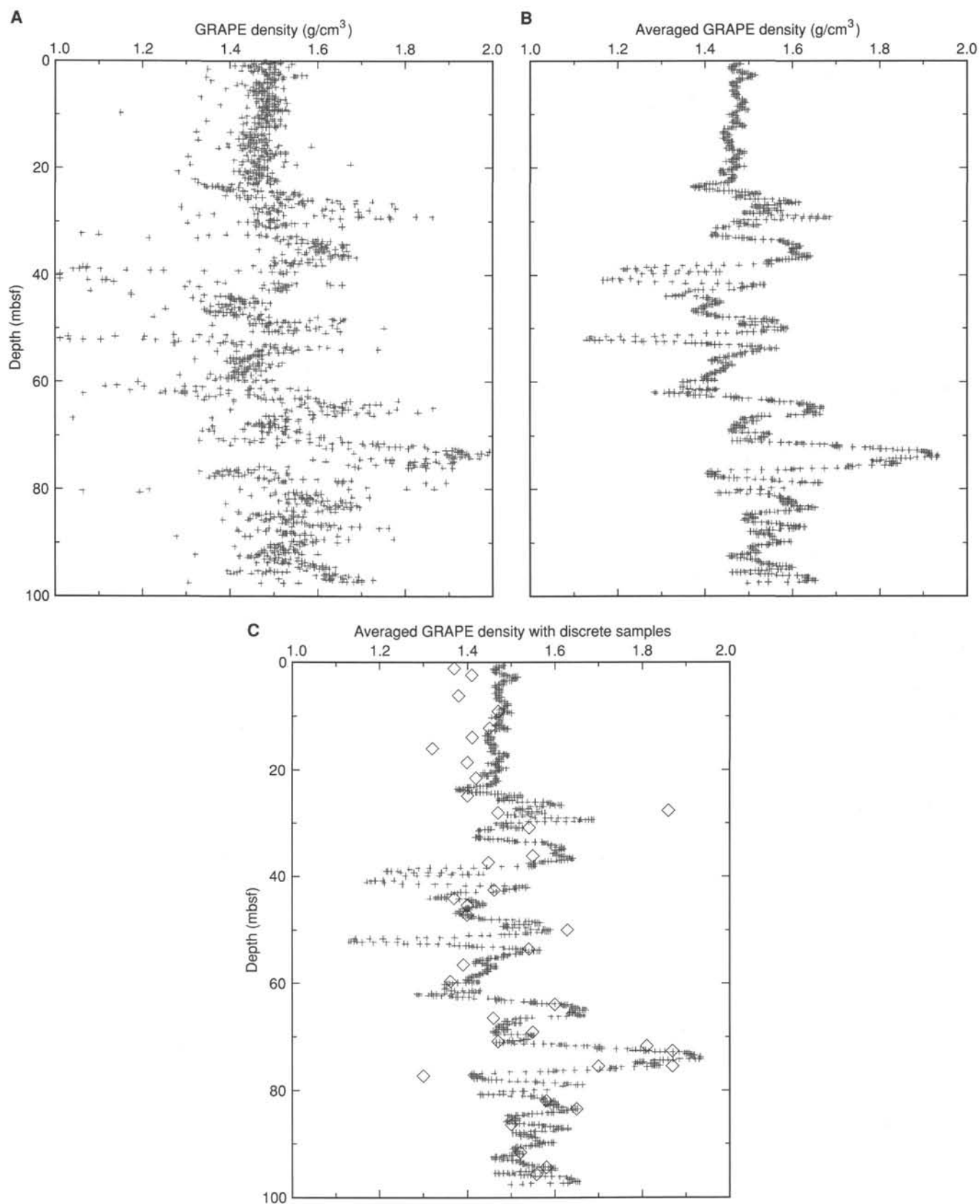


Figure 33. **A.** Grape bulk density vs. depth, Hole 838A; data are averaged over a 5-cm interval. **B.** Grape bulk density vs. depth, Hole 838A, with values averaged over 15 points, or 75 cm. **C.** GRAPE bulk density vs. depth, Hole 838A, with discrete bulk density values (open diamonds) plotted vs. GRAPE bulk density values for comparison.

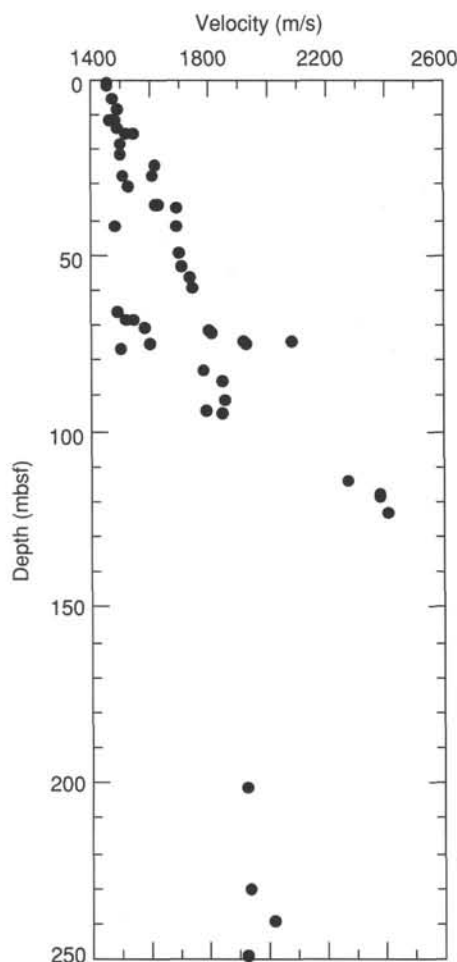


Figure 34. Compressional wave velocity vs. depth, Holes 838A and 838B.

The shear strength reflects the smoothly increasing consolidation of the fine-grained sediments in the upper 20 mbsf of the hole. Values remain low (less than 10 kPa) to 10 mbsf, then rapidly increase to about 100 kPa by 36 mbsf. Below 22 mbsf, the vane shear strength results are probably not representative of the degree of consolidation, as values are commonly lower than measured in the upper part of the hole, and the core section commonly cracked during measurement, thus reducing the measured shear strength. Samples recovered from 100 mbsf and below were all lithified and unsuitable for measurement with the vane shear apparatus.

Thermal Conductivity

In soft sediment cores, all values were obtained using needle probes inserted through core liners into full core sections. No conductivity values were acquired in the semilithified sediments; the samples would have disintegrated if measured in a water bath. The thermal conductivity results are shown in Figure 38 and tabulated in Table 11.

The conductivity results can be divided into three segments. From 0 to 33 mbsf, conductivity values average 0.89 W/(m · °K) and show little gradient with depth. This section is mainly nannofossil ooze, and the measured values are similar to values seen in nannofossil ooze at Sites 834–837. From 33 to 64 mbsf, the average values decrease, from around 0.8 to 0.67 W/(m · °K), in a section dominated by vitric sand and gravel. The negative gradient correlates with increasing grain size within the vitric

sand and gravel. At 64 mbsf, an abrupt increase in the conductivity occurs, to almost 1.0 W/(m · °K). The increase in conductivity occurs in a section of nannofossil ooze at the base of the vitric sand and gravel unit. From 64 to 95 mbsf, the conductivity gradient is again negative, with values of about 0.77 W/(m · °K) at 95 mbsf. The negative gradient correlates with the lower thick vitric sand and gravel unit, which grades downward into very coarse material at the base of the section at 98.5 mbsf.

Temperature Measurements

The water sampler temperature probe (WSTP) was used to make temperature measurements at two points in Hole 838A, at 32.2 and 51.2 mbsf (Fig. 39). The temperature history in the sedimentary section should be such that after 5 min in the sediment, the decay curve is approximated by:

$$T(t) = A/t + T_{eq},$$

where A is a constant determined experimentally, t is time, and T_{eq} is the equilibrium formation temperature (Hyndman et al., 1987).

The temperature gradient defined by these measurements is unclear. If a straight line is fit to the two data points (Fig. 40), the temperature gradient is 6.8°C/100 m, but the temperature required at the seafloor would be about 4.5°C (Fig. 40A). This is higher than the estimated seafloor temperature at previous holes and higher than the temperature that was measured during logging at this site. Alternatively, the temperature used at the seafloor at previous sites can be used as a third point (Fig. 40B). In this case, the estimated temperature gradient is 8.7°C/100 m. Our preferred gradient is the higher one. In either case, the temperature gradient is the highest measured at any of the Leg 135 Lau Basin sites; previously determined values are 2.11°C/100 m at Site 837, 1.53°C/100 m at Site 835, and 5°C/100 m at Site 834.

Thermal conductivity measurements were used to calculate thermal resistivity and integrated over depth. When the resulting thermal resistance is plotted with the temperature measurements from the WSTP temperature probe, the slope of the regression line indicates that the heat flow in the region is 50.6 mW/m², very similar to the calculated heat flow at Site 834 of 50 mW/m². For comparison, the calculated heat flow at Site 835 is 14.5 mW/m², at Site 837 it is 24.4 mW/m², and heat flow predicted by theoretical heat flow curves approaches 200 mW/m² for young crust (Anderson et al., 1977).

Discussion

Physical properties data correlate well with the lithologies sampled in the cores. Nannofossil ooze has a relatively low density and velocity profile on the GRAPE and P -wave logger data and on discrete samples. Black vitric sands and interbedded mudstones have high densities and velocities, and the two sections of thick vitric sand and gravel are distinguished by moderate densities and high velocities, with the high velocities caused by increased grain-to-grain contact of mud-supported clasts with consolidation. Thermal conductivity is also markedly affected by the grain size in the sand and gravel units, decreasing with increasing grain size.

Physical properties data are sparse from the hole below 100 mbsf. However, the data indicate that the section below 200 mbsf is underconsolidated for its burial depth. Measured index values and velocities all change markedly, with a decrease in velocity and bulk density in the deeper units, and corresponding increases in the other index properties of porosity, water content, and void ratio. Highly impermeable units, such as the well-consolidated clayey vitric sandstone, siltstone, and claystone units sampled between 113.5 and 152 mbsf, may be providing a seal that pre-

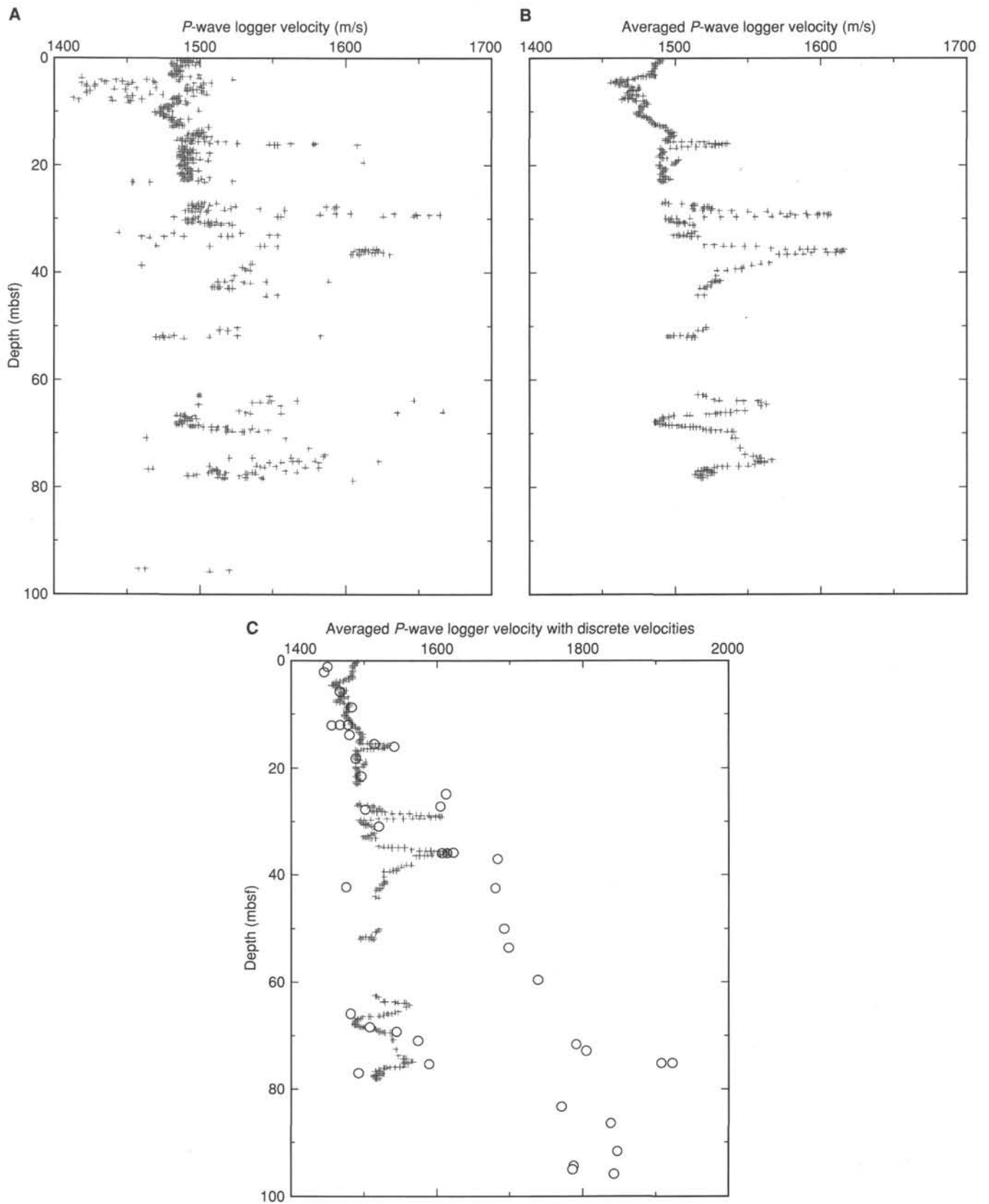


Figure 35. **A.** *P*-wave logger data vs. depth, Hole 838A; data are averaged over a 5-cm interval. **B.** *P*-wave logger data vs. depth, Hole 838A, with values averaged over 15 points, or 75 cm. **C.** *P*-wave logger velocity vs. depth, Hole 838A, with discrete velocity values (open circles) plotted vs. *P*-wave logger velocities for comparison.

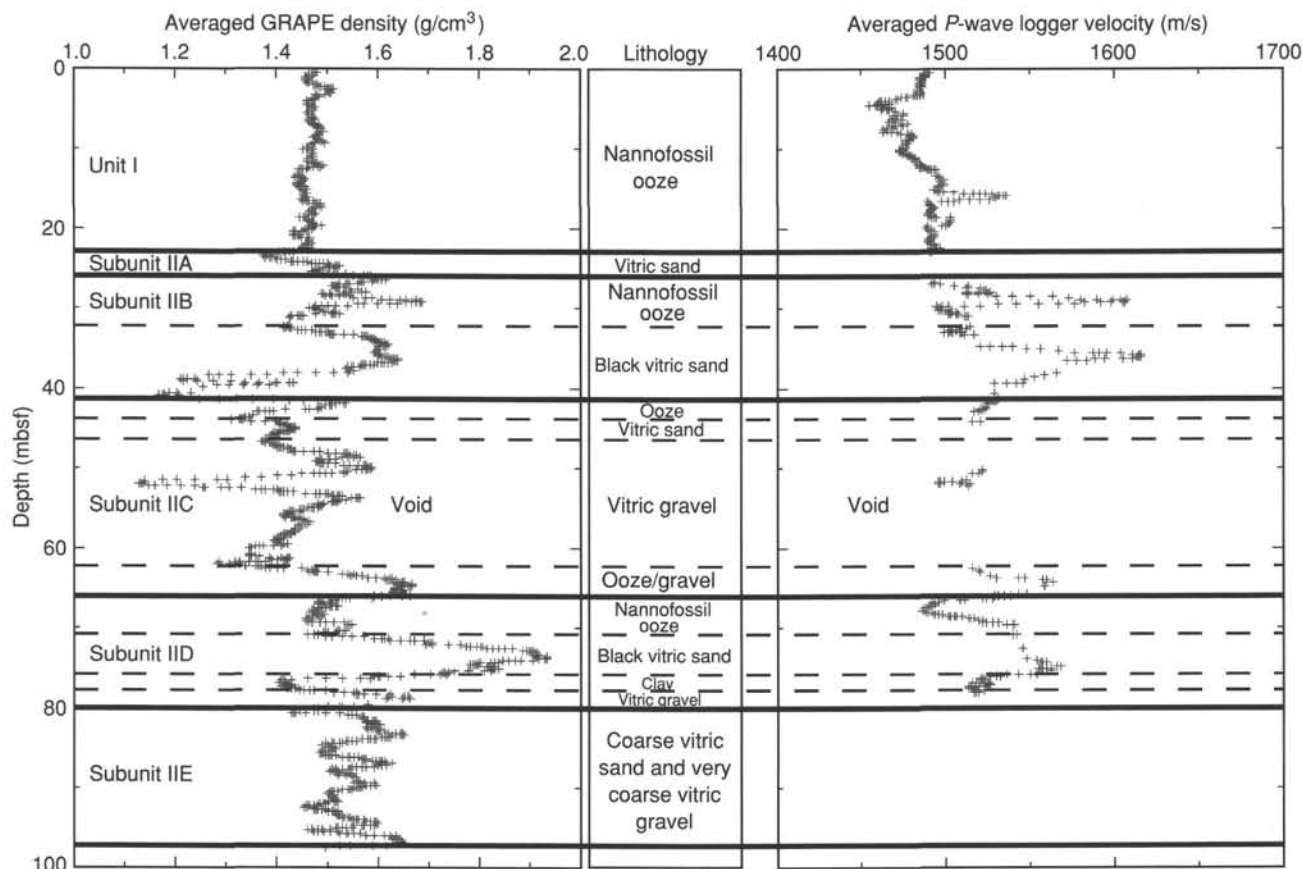


Figure 36. Averaged GRAPE bulk density and *P*-wave logger velocities vs. depth correlated to the lithology of the upper 100 mbsf of Hole 838A.

vents dewatering of the underlying section, resulting in high pore pressures and underconsolidation in the strata below 200 mbsf.

DOWNHOLE MEASUREMENTS

Operations

Logging operations at Hole 838B began at 0430 UTC on 14 January 1991 and ended at 0200 UTC on 15 January 1991. Total depth cored at Hole 838B was 259.2 mbsf. The end of the drill pipe was set at 72 mbsf except in those cases (see below) when the driller raised the pipe to the top of the rig (30 m) to give us an additional open portion of the hole. Well-logging operations at Hole 838B consisted of four logging runs using the seismic stratigraphic string, the formation microscanner (FMS) log string, the lithoporosity string, and the geochemical string.

The first logging run was made with the seismic stratigraphic string. This string consists of the long-spaced sonic, the phasor dual induction, and the natural gamma-ray tools, plus a three-arm caliper to center the tool string in the hole. The seismic stratigraphic tool combination measures compressional sound-wave velocity, resistivity, hole diameter, and the natural gamma-ray spectrum. The logging sequence with the seismic stratigraphic tool string consisted of a downlog from 72 to 212 mbsf, a main uplog from 242 to 72 mbsf openhole, and another uplog from 233 to 72 mbsf openhole. The downlog was recorded at 914 m/hr (3000 ft/hr) and the uplogs were recorded at 610 to 762 m/hr (2000 to 2500 ft/hr).

The second logging run was made with the FMS string. Pass 1 was recorded openhole from 231 to 59 mbsf (after the driller raised the pipe 30 m) and pass 2 was recorded from 229 to 58 mbsf

openhole. The logging speed for both passes was 488 m/hr (1600 ft/hr).

The third logging run consisted of a main and a repeat section with the lithoporosity tool string combination which includes a high-temperature lithodensity tool, compensated neutron porosity tool, and natural gamma-ray tool. This combination measures density, porosity, gamma ray, photoelectric effect, and borehole diameter with an 18-in. maximum diameter caliper. Two logging passes were made: the first from 229 to 64 mbsf and the repeat from 142 to 65 mbsf. The logging speed for both passes was 488 m/hr (1600 ft/hr).

The fourth logging run was made with the geochemical tool string, which consists of a combination of the aluminum clay tool, the gamma-ray spectrometry tool, the natural gamma-ray tool, and a compensated neutron tool. This tool string is run very slowly, at 183 m/hr (600 ft/hr). The main uplog was recorded openhole from 222 to 66 mbsf and a repeat section was logged from 143 to 45 mbsf openhole, then 45 mbsf up to the mudline in pipe. The openhole portion of the repeat from 128 to 45 mbsf showed evidence of irradiation in the natural gamma-ray curves and the in-pipe section will need to be corrected for the effect of the pipe during post-cruise processing.

Onboard Processing and Data Quality

Data were processed as described in the "Downhole Measurements" section of the "Explanatory Notes" chapter (this volume). Depths should be considered as uncorrected and preliminary, and may change as much as 5 m during post-cruise processing. The logging speeds were too high (greater than 274 m/hr or 900 ft/hr) on the first three runs to get reliable values for the computed gamma-ray, thorium, uranium, and potassium curves. However,

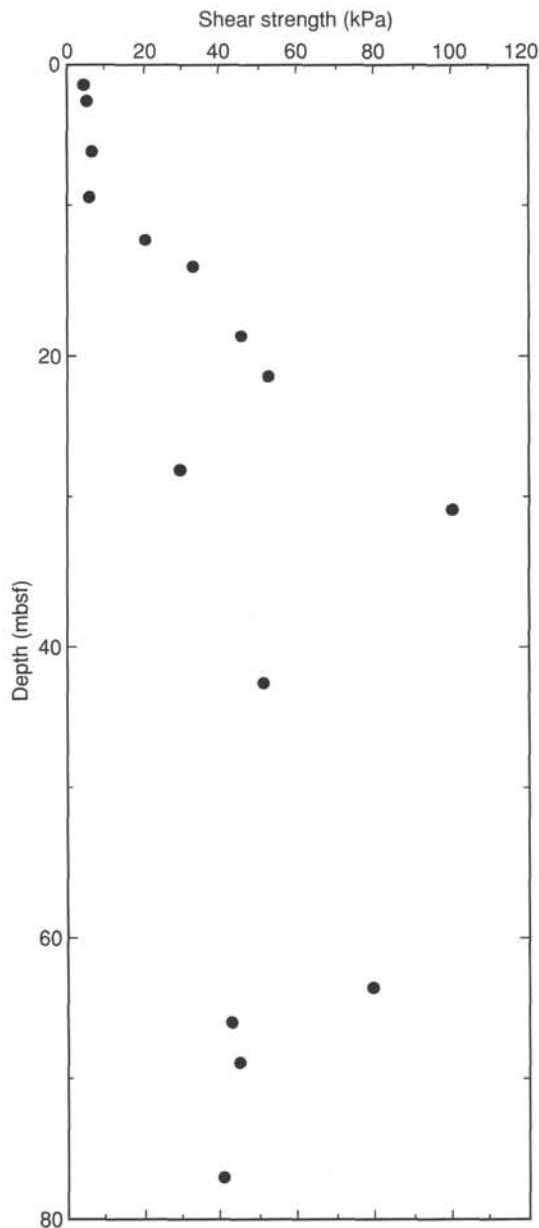


Figure 37. Undrained shear strength vs. depth, Hole 838A.

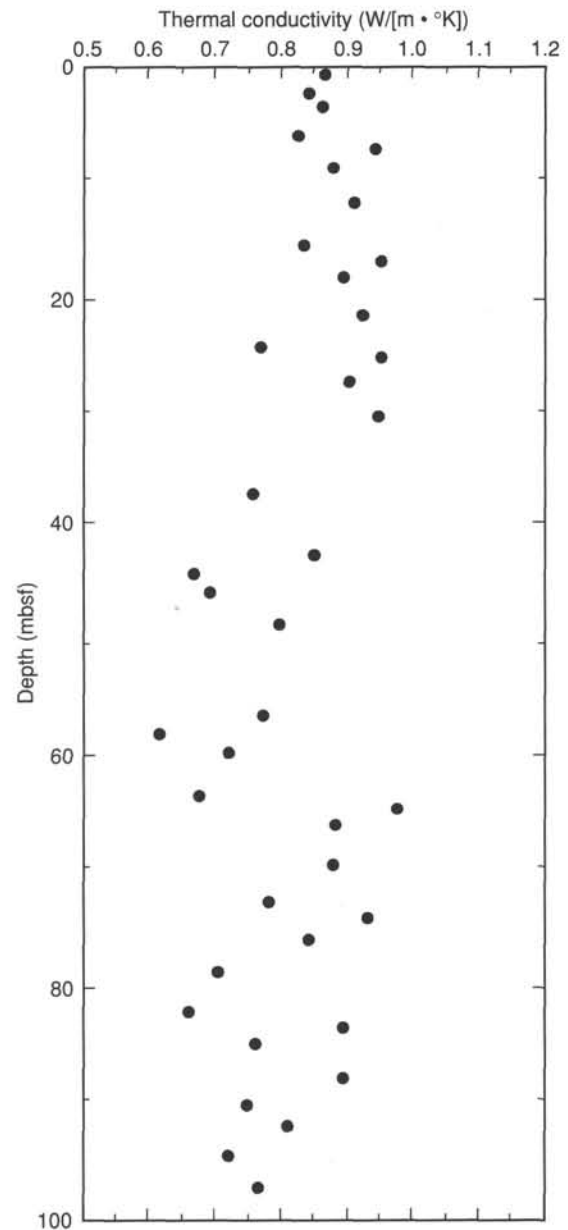


Figure 38. Thermal conductivity vs. depth, Hole 838A.

the fourth run with the geochemical tool string was logged at a speed sufficiently low to produce gamma-ray curves of good quality.

FMS processing was done onboard the *JOIDES Resolution* using a VAXstation 3200 and proprietary Schlumberger software. The data were shifted to meters below seafloor, the inclinometry computed, the speed correction applied, the data equalized and normalized, and image plots generated. The FMS pads did not make good enough contact with the borehole walls between 152 and 132 mbsf to produce images of satisfactory quality.

Results and Interpretation

The results of the logging in Hole 838B are shown in Figures 41 through 47. The lithology at the site consists of three units, of which log data is available for Units II and III. Unit I (0–23.04 mbsf) is clayey nannofossil ooze with thin volcanoclastic turbidite. Unit II is subdivided into five subunits: Units IIA and IIB

(23.04–41.82 mbsf) show increasing amounts of vitric sand in the nannofossil ooze; Units IIC and IID (41.82–79.7 mbsf) show increasing amounts of gravel in the ooze and sand; and Unit IIE (79.7–98.7 mbsf) is coarse vitric sand with pebbles and very coarse vitric sand with gravel. The recovered portions of Unit III (98.7–259.2 mbsf) comprise pumiceous volcanic gravel, conglomerate, vitric sandstone, and vitric clayey siltstone (see “Lithostratigraphy” section, this chapter).

Caliper Logs

In Hole 838B, the FMS caliper logs (Fig. 41) show that the hole diameter is less than the 15-in. minimum required and much is between 12 and 15 in. (30.5 to 38.1 cm), with the exception of the interval between 132 and 152 mbsf, where one caliper is at 15.25 in. (38.7 cm) and the other is at the maximum extension of 15.5 in. (39.4 cm). The caliper from the lithodensity tool also reaches its maximum extension of 19 in. (48.3 cm) in the same

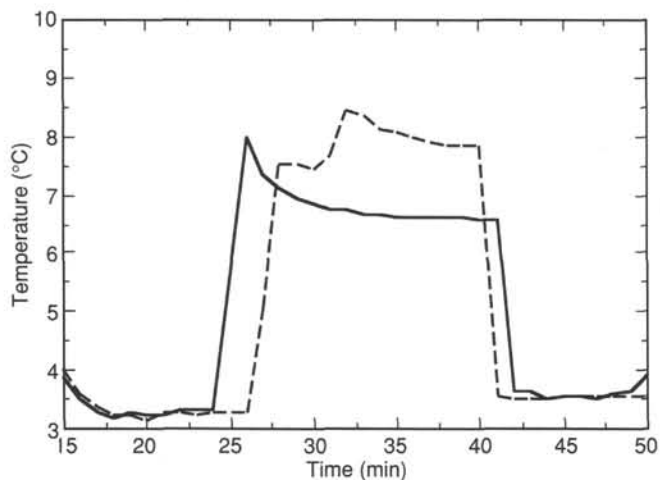


Figure 39. Heat flow measurements, Hole 838A, from various depths, based on WSTP runs. Solid line = 32.2 mbsf and dashed line = 51.2 mbsf.

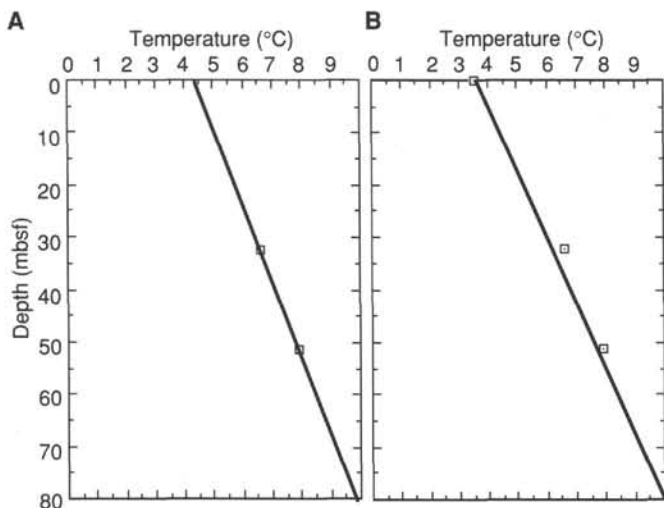


Figure 40. Temperature gradients vs. depth, Hole 838A, with lines showing geothermal gradients. A. Geothermal gradient using only temperatures measured in Hole 838A. B. Geothermal gradient assuming a seafloor temperature of 3.5°C.

interval (Fig. 42). The true size of the hole over that interval is unknown. The FMS calipers indicate that the hole is elliptical between 60 and 225 mbsf. The hole is essentially circular below 225 mbsf, with the diameter varying from 13 in. at 170 mbsf to 15.5 in. at 185–190 mbsf.

Gamma-ray Log

The gamma-ray log data (SGR in Figs. 42 and 43) are valid in Hole 838B except between 132 and 152 mbsf, where the hole size is too large to produce reliable data. The gamma-ray log commonly correlates well with clay-rich formations. The gamma-ray levels are 20 to 30 American Petroleum Institute (API) units between 65 and 85 mbsf. Between 85 and 90 mbsf there is a significant excursion in the log values to about 40 to 45 API units. This increase correlates with a volcanic gravel with interbeds of pebbly coarse vitric sand in Unit IIE. A similar change in the gamma-ray level occurs in the region between 113 and 125 mbsf. This second increase in gamma radiation occurs in Unit III in a vitric clayey siltstone and vitric sandstone, and, as recovery was

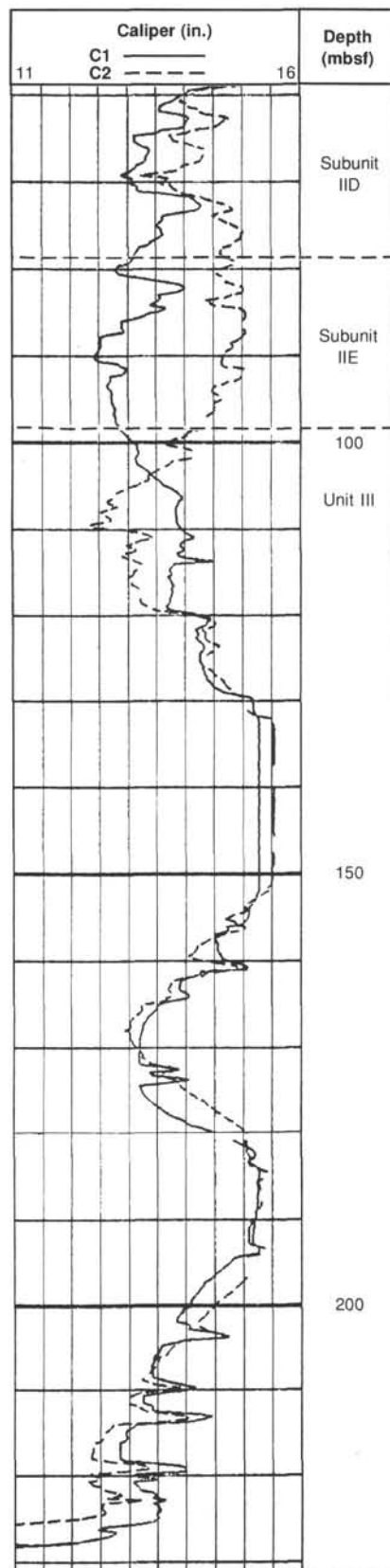


Figure 41. Caliper data for Hole 838A obtained from the formation microscanner tool. C1 (caliper 1–3) and C2 (caliper 2–4) are plotted at a scale of 11–16 in.

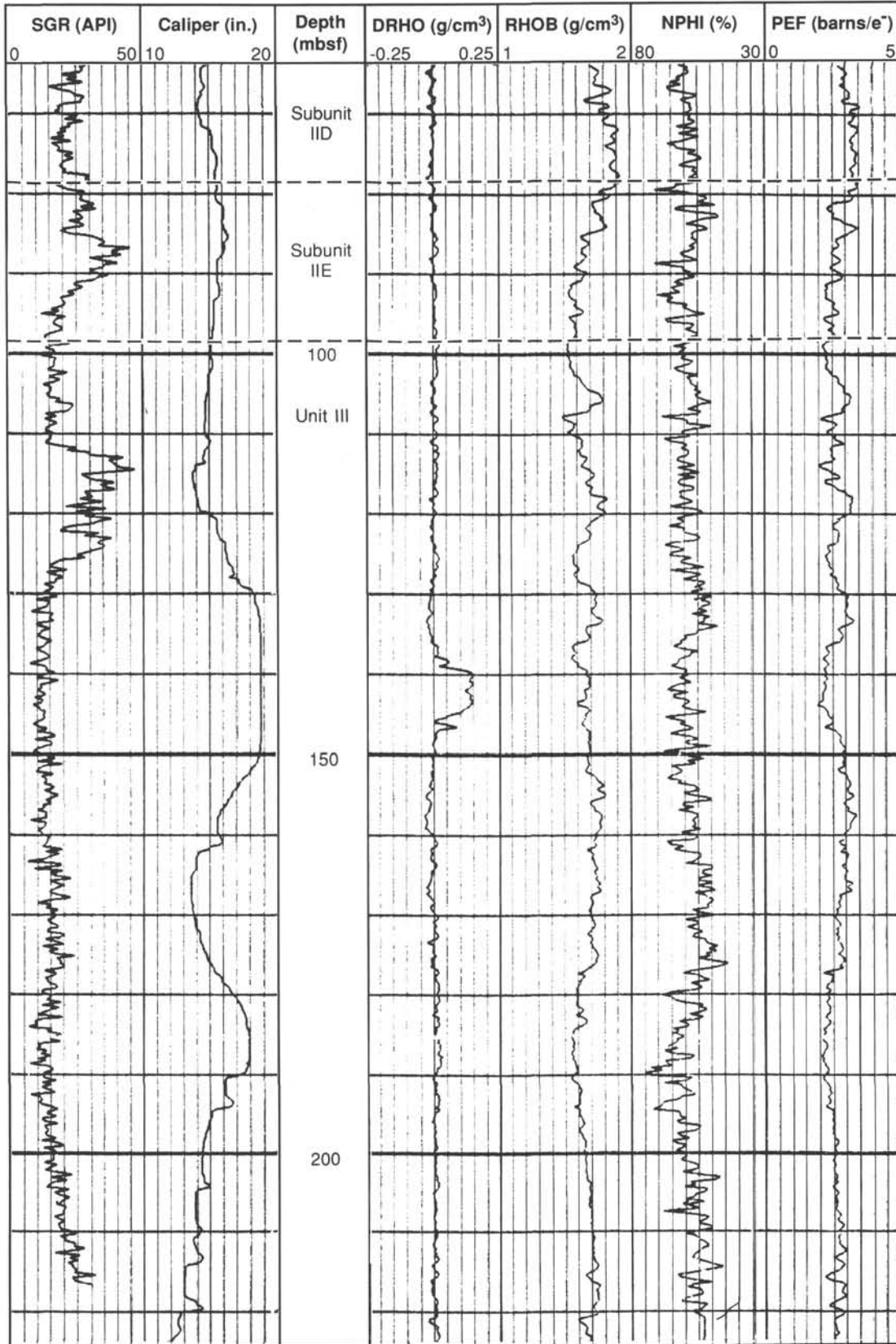


Figure 42. Lithoporosity tool-string logs vs. depth, Hole 838B. The logs illustrated are as follows: total gamma ray (SGR, in API units); caliper hole diameter (in inches); density compensation (DRHO), bulk density (RHOB), neutron porosity (NPHI), and photoelectric effect (PEF, in barns/electrons). Lithologic units are given in the center column.

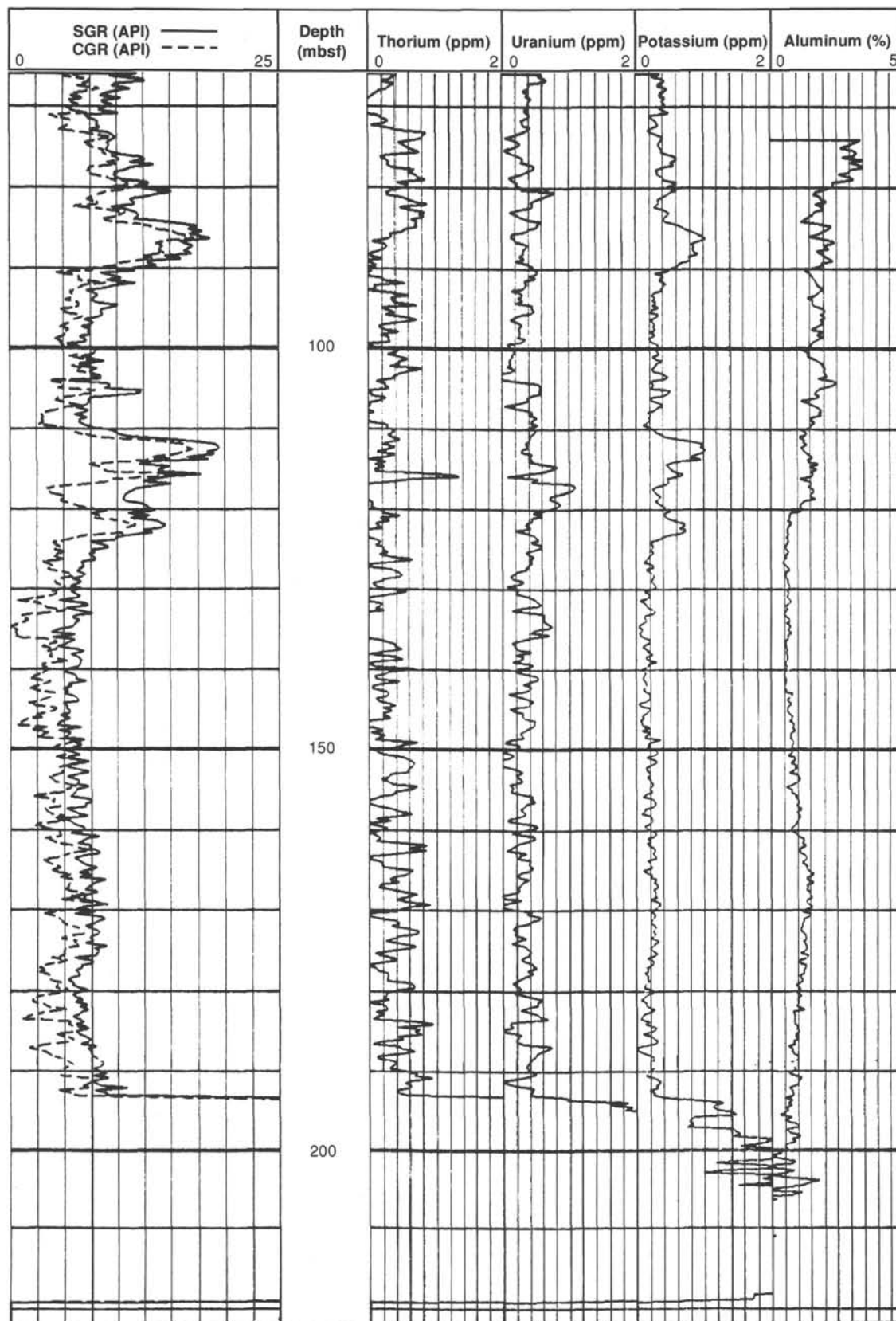


Figure 43. Geochemical tool-string natural gamma-ray logs vs. depth, Hole 838B. The logs illustrated are as follows: total gamma ray (SGR, in API units), computed gamma ray (CGR, in API units), thorium, uranium, potassium, and aluminum.

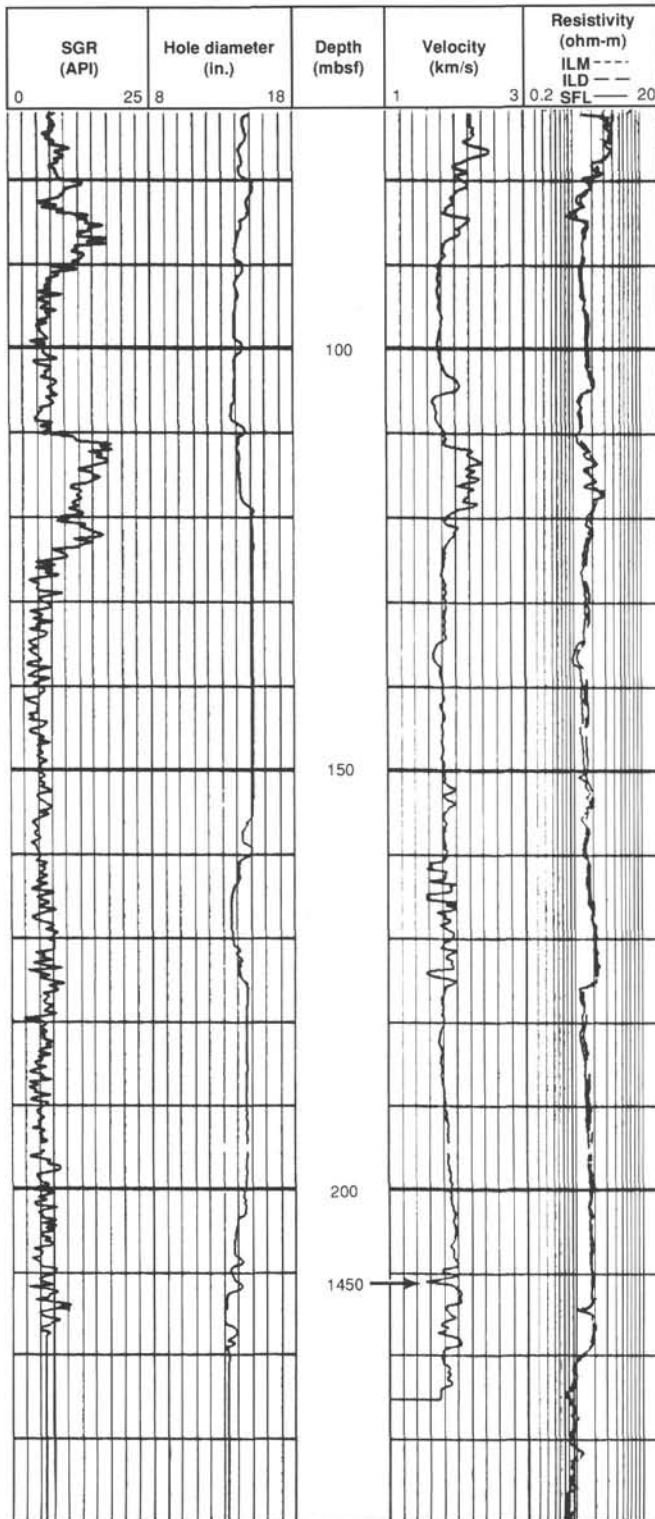


Figure 44. Seismic stratigraphic tool-string logs vs. depth, Hole 838B. The logs illustrated are as follows: total gamma ray (SGR, in API units), hole diameter (in inches); sonic velocity, and medium (ILM), deep (ILD), and spherically focused (SFL) resistivity (on a logarithmic scale).

poor, may indicate that a significant amount of clay was not recovered during drilling. Below 152 mbsf, gamma radiation levels gradually increase from about 15 to 30 API units.

Density Log

The bulk density log data (RHOB in Fig. 42) are valid except between 130 and 150 mbsf (Fig. 42). The values measured by the density log vary between 1.5 and 1.8 g/cm³ within the 65 to 220 mbsf measured section. The highest densities are recorded between 75 and 85 mbsf, within lithostratigraphic Units IID and IIE (sands and gravels in a nanofossil matrix). Below 85 mbsf, density values are commonly between 1.5 and 1.6 g/cm³, with maxima at 1.75 g/cm³. These values are typical of semilithified sediments (Hamilton, 1980). Higher values more typical of basalts (2.6 g/cm³) were not measured. Laboratory measurements of bulk density were made on APC cores (0–98.7 mbsf) using the GRAPE technique and show a close correlation (see “Physical Properties” section, this chapter).

Neutron Porosity Log

Porosity values (NPHI in Fig. 42) vary between 50% and 65%, with average values of about 60% and are relatively constant downhole. Laboratory-measured porosity values between 65 and 220 mbsf (see “Physical Properties” section, this chapter) show similar porosity variations, but with the values decreasing slightly with depth from about 60% to 55%.

Resistivity and Sonic Velocity Logs

The resistivity logs (ILM, ILD, and SFLU in Fig. 44) and the sonic velocity log (VEL in Fig. 44) have similar characteristics. The resistivity and velocity data are positively correlated. The velocity and resistivity values are high (>200 m/s and >2.2 ohm-m, respectively) in the upper part of the logged hole between 75 and 80 mbsf, reflecting the presence of gravels and sands. Both velocity and resistivity decrease between 85 and 100 mbsf (<1800 m/s and <2.1 ohm-m, respectively). Increases in velocity and resistivity between 111 and 121 mbsf near the top of Unit III correlate with the increase in gamma radiation. Compressional wave velocity increases between 152 and 155 mbsf to 2000 m/s, suggesting a change in lithology to coarser grained units or to a more consolidated unit. Between 160 and 175 mbsf and 200 and 225 mbsf, sharp alternations of velocity between 1600 and 2000 m/s suggest interbedding of different lithologic types, possibly nanofossil ooze and sands or gravels; however, examination of the FMS images (see below) does not necessarily support this hypothesis. The resistivity data displays slightly higher values in these latter zones.

Geochemical Yields

A preliminary assessment of unprocessed data identifies Ca and Fe decreasing downhole, S increasing downhole, with the remaining elements relatively constant (Fig. 45). Further analysis will be undertaken following post-cruise processing.

Formation Microscanner

FMS data were acquired from 59 to 225 mbsf in Hole 838B and potentially offer the most direct and accessible information on the lithologies present. On the basis of variations in resistivity, texture, and structure in the FMS images, five subdivisions assumed to be of lithological significance can be recognized.

From 59 to 88 mbsf: The uppermost 29 m of the FMS log displays regular, parallel, centimeter- to decimeter-scale dark (low-resistivity) and pale (high-resistivity) banding. The pale bands have sharp bases with a marked resistivity contrast but display gradational decreases in resistivity in their upper parts. These pale bands almost certainly represent normally graded sand

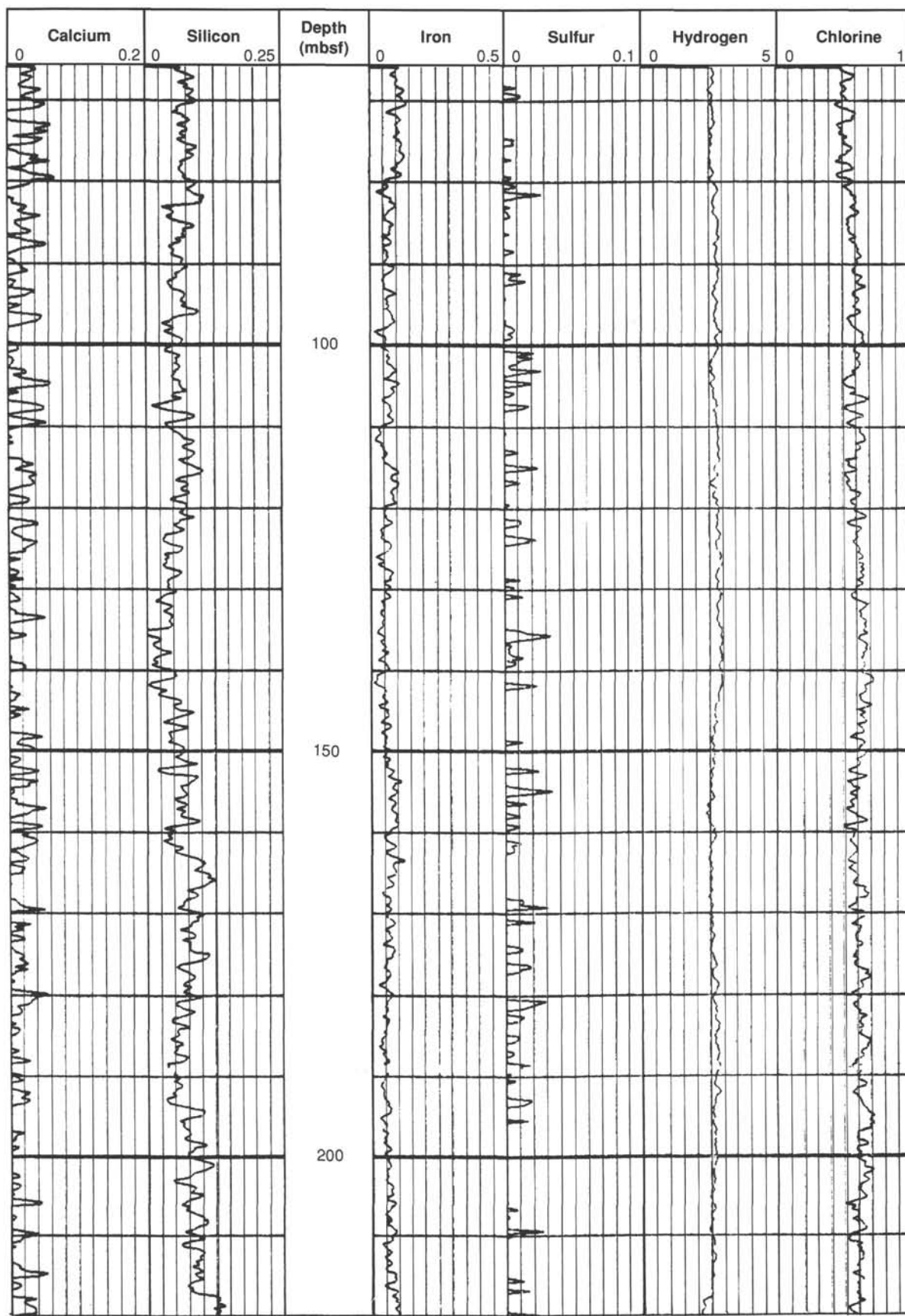


Figure 45. Geochemical yield logs vs. depth, Hole 838B. The logs illustrated are as follows: calcium, silicon, iron, sulfur, hydrogen, and chlorine.

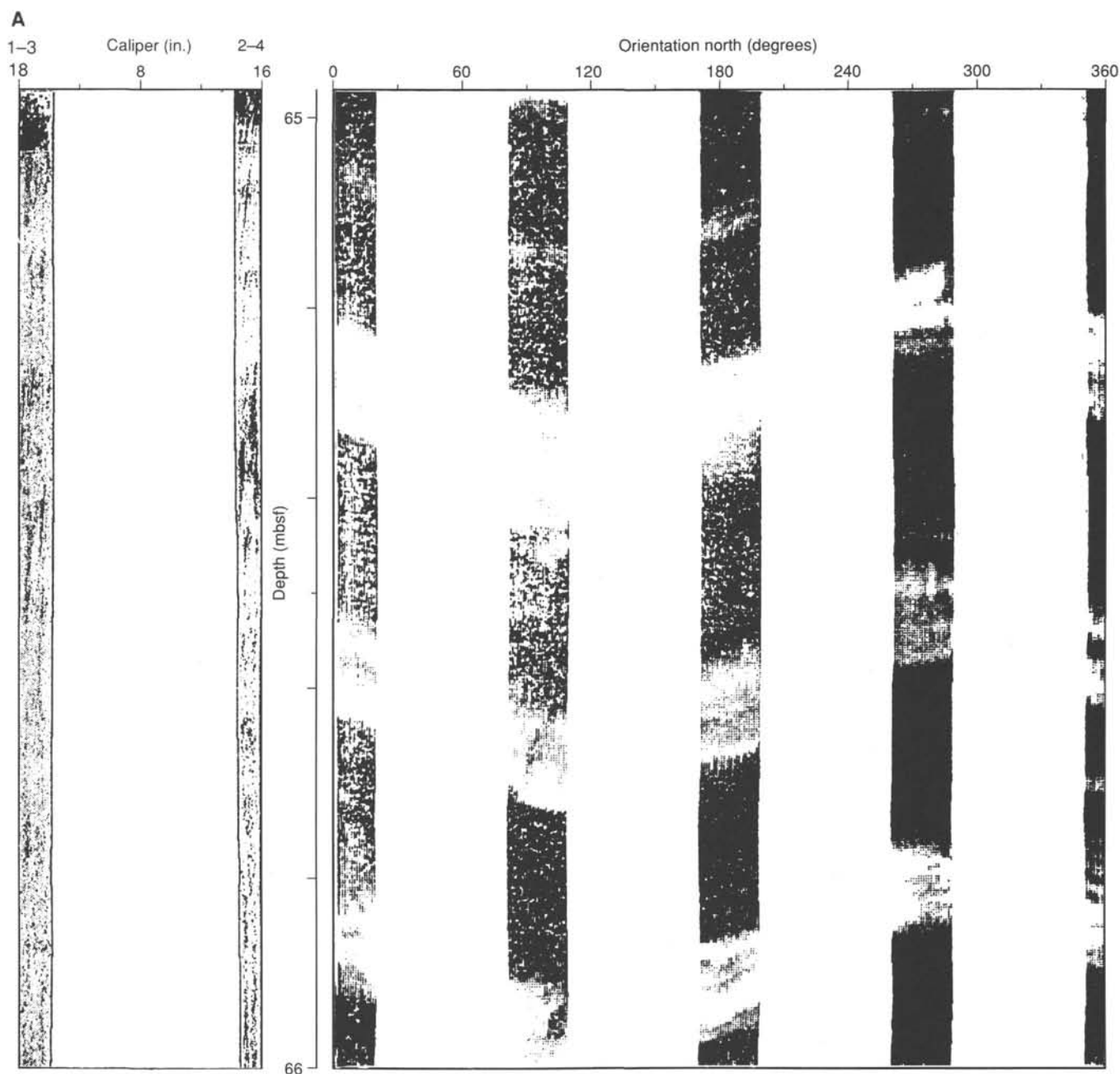


Figure 46. **A.** Formation microscanner images from 65 to 66 mbsf, which display an average dip toward the southeast of about 21° . **B.** FMS images from 88 to 89 mbsf. Note the dark gray-mottled pattern interpreted to be volcaniclastic gravels. For both figures, horizontal and vertical scales are 1:5. FMS caliper logs are illustrated on the left-hand side.

or ash turbidite deposits, contained within a background of lower resistivity nannofossil ooze. Similar interpretations have been made at previous sites (see "Downhole Measurements" sections, "Site 834" and "Site 835" chapters, this volume). The bands display a regular sinusoidal trace on the FMS images here, indicating an average dip toward the southeast of about 21° (Fig. 46A).

From 88 to 113 mbsf: Below 88 mbsf the sinusoidal banding indicative of finely bedded, inclined strata is replaced by a consistent dark grey mottled pattern (Fig. 46B). This mottling is defined by irregular spots of higher and lower resistivity, corresponding to features on the borehole wall in the order of

millimeters to a few centimeters in diameter. The pattern is very reminiscent of, and almost certainly represents, images of the volcaniclastic, often pumiceous gravels that occur frequently in Unit II of Hole 838A (see "Lithostratigraphy" section, this chapter). These are interpreted as mass-flow deposits. Between 104 and 106 mbsf an overall increase in resistivity level in the mottled texture occurs, and at 106 mbsf a change to a less resistive mottled pattern of similar texture is observed. A very dark, very low-resistivity band up to 20 cm wide, visible on two or three of the pads, may correspond to a fracture at this point. Dark mottled images interpreted as gravels occur down to approximately 113 mbsf, with slight variations of resistivity on a decimeter scale

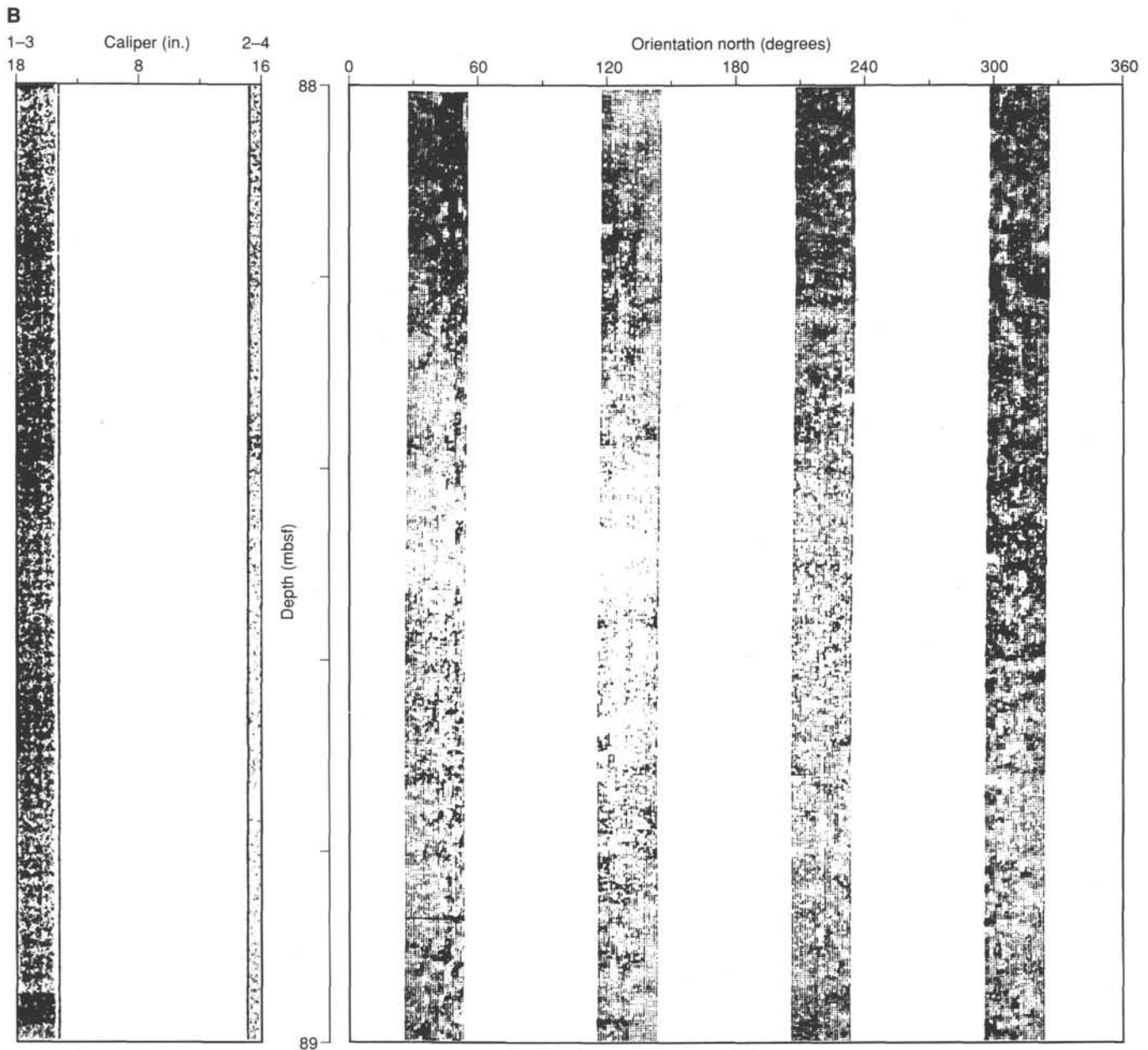


Figure 46 (continued).

within the gravels in the lowermost few meters tentatively interpreted as poorly defined sedimentary bedding.

From 113 to 123 mbsf: At 113–114 mbsf irregular areas of low resistivity up to 30 cm thick are visible. These are accompanied by an increase in caliper readings and clearly correspond to fractures. They define a general sinusoidal pattern indicating a strike of 240° and dip of 75° toward the northwest (see “Structural Geology” section, this chapter). Below the zone of fracturing, regularly bedded sediments dipping at up to 30° toward the southeast are visible. As described above, sharp changes in resistivity at the bases of units and gradual changes at their tops indicate normal grading and suggest that they are turbidites. Individual units may be up to 1.5 m thick. The change in lithology across the fractures suggests that they represent a fault zone.

From 123 to 215 mbsf: The graded turbiditic horizons described above pass downward gradually into coarse, mottled images that we suggest correspond to volcanoclastic gravels. A

monotonous sequence of this material continues for more than 90 m. A change to lower resistivities but similar mottled texture at 177 mbsf is interpreted as the contact between two flows. Between 135 and 147 mbsf the calipers are at maximum extent, the FMS tool has spun, and the FMS data are invalid.

From 215 to 230 mbsf: At 215 mbsf an abrupt contact is observed between mottled images above (possibly thick volcanoclastic gravels) and a 1-m-thick featureless stratum with very low resistivity below. The likelihood is that this unit corresponds to a clay-rich layer. At 216 mbsf mottled images that probably represent gravels are again observed. The upper and lower contacts of the low-resistivity interbed dip south-southwestward at about 15° . At 220 mbsf the mottled images pass gradually downward into very low-resistivity images that again appear very dark on the FMS images and extend all the way to the base of the section.

A hypothetical lithostratigraphic section interpreted from the above descriptions is shown schematically in Figure 47, and

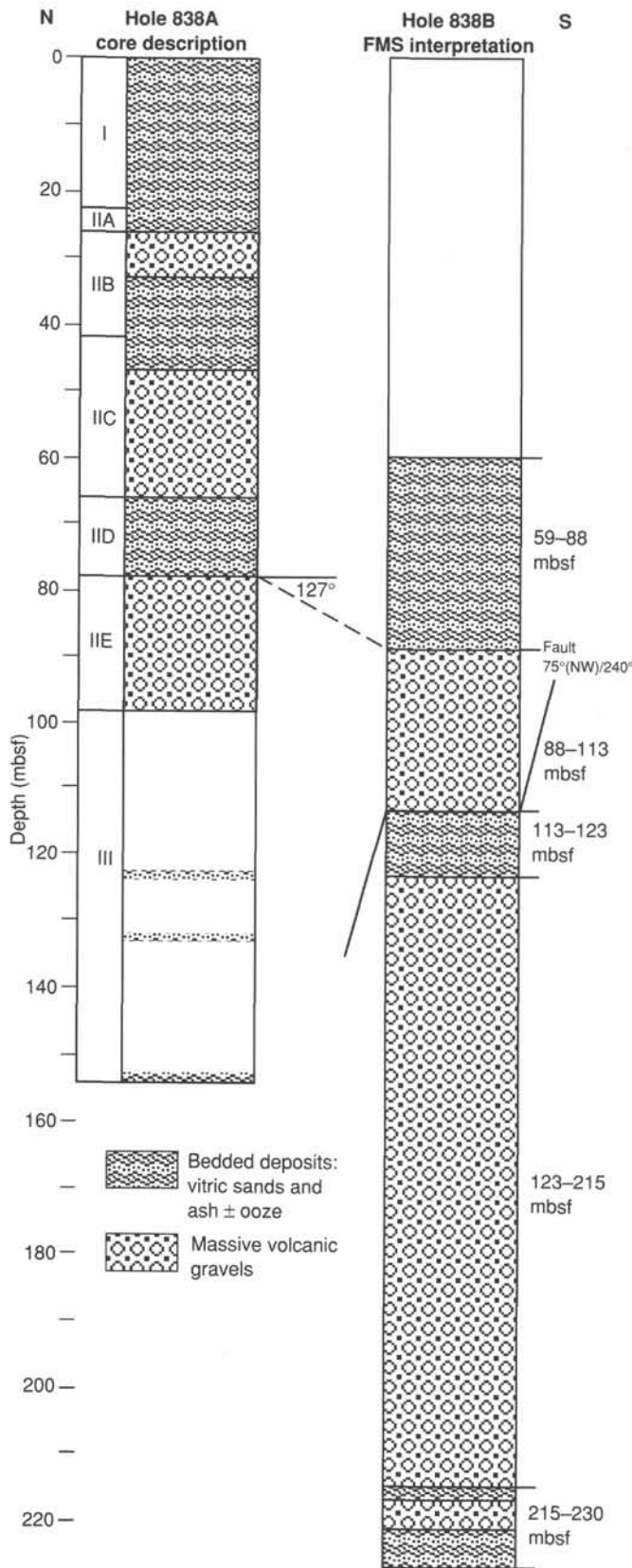


Figure 47. Formation microscanner (FMS) interpretation of Hole 838B sedimentary stratigraphy, with FMS-derived subdivisions shown to right. Hole 838A lithologic units illustrated at left.

compared with a simplified lithostratigraphic section synthesized from core observations of Hole 838A (see "Lithostratigraphy" section, this chapter). The two constructed sections overlap by 39 m (from 59 to 98 mbsf), and within this zone comparison between the two sequences should be possible. No direct correlation is evident; however, it is possible that the bedded sequence visible in the uppermost portion of the FMS image in Hole 838B (between 59 and 88 mbsf) represents the lateral equivalent of the approximately 12-m thickness of bedded vitric sand with subordinate nannofossil ooze at 66–78 mbsf in Subunit IID of Hole 838A. The bedded sediments imaged by the FMS are at least 29 m thick and possibly substantially thicker, so a significant thinning of this subunit toward the north or northwest is implied if the correlation is correct. This suggests that some at least of the sedimentary strata encountered at Site 838 may be highly laterally discontinuous.

The only other bedded sediments of comparable thickness in Hole 838A that may be compared to the banded images on the FMS from Hole 838B (between 59 and 88 mbsf) are interbedded ash turbidites and nannofossil oozes at depths of 0–46 mbsf. It is considered highly unlikely that these bedded sediments correspond to the FMS images, as a substantial fault would need to be inferred between Holes 838A and 838B to account for the difference of stratigraphic level.

If the correlation between the bedded portion of Subunit IID of Hole 838A and the FMS image between 59 and 88 mbsf is accepted, then the base of the subunit must dip toward the south (or, more probably, southeast). The dip of this horizon is calculated at approximately 27°, based upon a 20-m horizontal distance between Holes 838A and 838B. This dip estimate is almost exactly the same as MSD dipmeter measurements of the bedded turbiditic sediments in Hole 838B at about 88 mbsf. Bedding in Subunit IID dips southeastward by this amount, and therefore appears to be overlying the gravels of Subunit IIE conformably. As the FMS images do not continue above 59 mbsf, the nature of the upper contact of the equivalent of Subunit IID and the overlying Subunit IIC in Hole 838B is unknown.

DISCUSSION

The principal objectives for Site 838 were the same as those for Sites 836 and 837. In particular, a deep penetration (>200 m) of the volcanic basement section was the intended goal. A thicker than anticipated sedimentary section was encountered, the base of which was not reached. A number of small andesitic clasts were recovered from breccias and very coarse clastic layers in the overlying sediment section. They have compositional affinities to lavas erupted from the active Tonga and Kermadec arcs. A late Pliocene age was determined for the deepest sediments sampled, which comprise extensive mass-flow deposits consisting of gravels, mixed andesitic, and pumiceous conglomerates, vitric sandstones, and siltstones. These sediments suggest a proximal source. Turbidites overlain by nannofossil ooze in the upper units indicate a restoration of a more stable depositional system by the lower Pleistocene. As was also demonstrated at Site 839, the transition from high-energy sedimentation conditions (as shown by the coarse clastic sediments) to pelagic-dominated sedimentation during the lower Pleistocene may coincide with the establishment of true seafloor spreading conditions to the east at the ELSC. The northward-dipping floor of the Site 838 basin, which is linear and trends north-northeast, indicates a sediment transport direction toward Site 839 (north-northeast).

REFERENCES

Anderson, R. N., Langseth, M. G., and Sclater, J. G., 1977. The mechanisms of heat transfer through the floor of the Indian Ocean. *J. Geophys. Res.*, 82:3391–3409.

- Berggren, W. A., Kent, D. V., Flynn, J. J., and Van Couvering, J. A., 1985a. Cenozoic geochronology. *Geol. Soc. Am. Bull.*, 96:1407-1418.
- Berggren, W. A., Kent, D. V., and Van Couvering, J. A., 1985b. The Neogene: Part 2. Neogene geochronology and chronostratigraphy. In Snelling, N. J. (Ed.), *The Chronology of the Geological Record*. Geol. Soc. London Mem., 10:211-260.
- Bouma, A. H., 1962. *Sedimentology of Some Flysch Deposits*: Amsterdam (Elsevier).
- Broecker, W. S., and Peng, T.-H., 1982. *Tracers in the Sea*: Palisades, NY (Eldigio Press).
- Chaproniere, G.C.H., in press. Pleistocene to Holocene planktic foraminiferal biostratigraphy of the Coral Sea, offshore Queensland, Australia. *BMR J. Aust. Geol. Geophys.*
- Church, B. N., and Johnson, W. M., 1980. Calculation of the refractive index of silicate glasses from chemical composition. *Geol. Soc. Am. Bull.*, 91:619-625.
- Clement, B. M., Hall, F. J., and Jarrard, R. D., 1989. The magnetostratigraphy of Ocean Drilling Program Leg 105 sediments. In Srivastava, S. P., Arthur, M., Clement, B., et al., *Proc. ODP, Sci. Results*, 105: College Station, TX (Ocean Drilling Program), 583-595.
- Clement, B. M., and Robinson, F., 1987. The magnetostratigraphy of Leg 94 sediments. In Ruddiman, W. F., Kidd, R. B., Thomas, E., et al., *Init. Repts. DSDP*, 94, Pt. 2: Washington (U.S. Govt. Printing Office), 635-650.
- Emeis, K.-C., and Kvenvolden, K. A., 1986. Shipboard organic geochemistry on JOIDES Resolution. *ODP Tech. Note*, No. 7.
- Ewart, A., 1979. A review of the mineralogy and chemistry of Tertiary-Recent dacitic, latitic, rhyolitic and related salic volcanic rocks. In Barker, F. (Ed.), *Trondhjemites, Dacites, and Related Rocks*: Amsterdam (Elsevier), 13-121.
- Ewart, A., Bryan, W. B., and Gill, J., 1973. Mineralogy and geochemistry of the younger volcanic islands of Tonga, southwest Pacific. *J. Petrol.*, 14:429-465.
- Ewart, A., and Hawkesworth, C. J., 1987. The Pleistocene-Recent Tonga-Kermadec arc lavas: interpretation of new isotope and rare earth data in terms of a depleted mantle source model. *J. Petrol.*, 28:495-530.
- Gieskes, J. M., Kastner, M., and Warner, T. B., 1975. Evidence for extensive diagenesis, Madagascar Basin, Deep Sea Drilling Site 245. *Geochim. Cosmochim. Acta*, 39:1385-1393.
- Gieskes, J. M., and Lawrence, J. R., 1981. Alteration of volcanic matter in deep sea sediments: evidence from the chemical composition of interstitial waters from deep sea drilling cores. *Geochim. Cosmochim. Acta*, 45:1687-1703.
- Harland, W. B., Cox, A. V., Llewellyn, P. G., Pickton, C.A.G., Smith, D. G., and Walters, R., 1982. *A Geologic Time Scale*: Cambridge (Cambridge Univ. Press).
- Hawkins, J. W., 1976. Petrology and geochemistry of basaltic rocks of the Lau Basin. *Earth Planet. Sci. Lett.*, 28:283-297.
- _____, 1985. Low-K rhyolitic pumice from the Tonga ridge. In Scholl, D. W., and Vallier, T. L. (Eds.), *Geology and Offshore Resources of Pacific Island Arcs—Tonga Region*. Circum-Pac. Council Energy and Miner. Resour., Earth Sci. Ser., 2:171-178.
- _____, 1989. Cruise Report—ROUNDABOUT Expedition, Legs 14, 15, R/V *Thomas Washington*. *SIO Ref. Ser.*, No. 89-13.
- Hawkins, J. W., and Melchior, J. T., 1985. Petrology of Mariana Trough and Lau Basin basalts. *J. Geophys. Res.*, 90:11,431-11,468.
- Hyndman, R. D., Langseth, M. G., and Von Herzen, R. P., 1987. Deep Sea Drilling Project geothermal measurements: a review. *Rev. Geophys.*, 25:1563-1582.
- Kastner, M., and Gieskes, J. M., 1976. Interstitial water profiles and sites of diagenetic reactions, Leg 35, DSDP, Bellingshausen Abyssal Plain. *Earth Planet. Sci. Lett.*, 33:11-20.
- Lovell, J.P.B., and Stow, D.A.V., 1981. Identification of ancient sandy contourites. *Geology*, 9:347-349.
- Lowe, D. R., 1982. Sediment gravity flows: II. Depositional models with special reference to the deposits of high-density turbidity currents. *J. Sediment. Petrol.*, 52:279-297.
- Mankinen, E. A., Donnelly, J. M., and Grommé, C. S., 1978. Geomagnetic polarity event recorded at 1.1 m.y.r. B.P. on Cobb mountain, Clear Lake volcanic field, California. *Geology*, 6:653-656.
- McDuff, R. E., 1981. Major cation gradients in DSDP interstitial waters: the role of diffusive exchange between seawater and upper ocean crust. *Geochim. Cosmochim. Acta*, 45:1705-1713.
- McDuff, R. E., and Gieskes, J. M., 1976. Calcium and magnesium profiles in DSDP interstitial waters: diffusion or reaction? *Earth Planet. Sci. Lett.*, 33:1-10.
- Miyashiro, A., 1974. Volcanic rock series in island arcs and active continental margins. *Am. J. Sci.*, 274:321-355.
- Nilsson, K., Florendo, F. F., and Hawkins, J. W., et al., 1989. Petrology of a nascent triple junction, northeastern Lau Basin. *Eos*, 70:1389.
- Okada, H., and Bukry, D., 1980. Supplementary modification and introduction of code numbers to the low-latitude coccolith biostratigraphic zonation (Bukry, 1973; 1975). *Mar. Micropaleontol.*, 5:321-325.
- Parson, L. M., et al., 1989. RRS *Charles Darwin* Cruise 33/88, 5 May-1 June 1988. Geophysical and geological investigations of the Lau back-arc basin, SW Pacific. Inst. Oceanogr. Sci. Deacon Lab. Cruise Report, No. 206.
- Parson, L. M., Pearce, J. A., Murton, B. J., and RRS *Charles Darwin* Scientific Party, 1990. Role of ridge jumps and ridge propagation in the tectonic evolution of the Lau back-arc basin, southwest Pacific. *Geology*, 18:470-473.
- Pickering, K. T., Hiscott, R. N., and Hein, F. J., 1989. *Deep Marine Environments: Clastic Sedimentation and Tectonics*: London (Unwin Hyman).
- Schlumberger, 1986. *Dipmeter Interpretation Fundamentals*: New York, (Schlumberger).
- Schmincke, H.-U., 1981. Ash from vitric muds in deep sea cores from the Mariana Trough and fore-arc regions (south Philippine Sea) (Sites 453, 454, 455, 458, 459). In Hussong, D. M., Uyeda, S., et al., *Init. Repts. DSDP*, 60: Washington (U.S. Govt. Printing Office), 473-481.
- von Stackelberg, U., 1990. R.V. *Sonne* cruise SO48: summary of results testing a model of mineralization. *Mar. Min.*, 9:135-144.
- Wilson, M., 1989. *Igneous Petrogenesis: A Global Tectonic Approach*: London (Unwin Hyman).

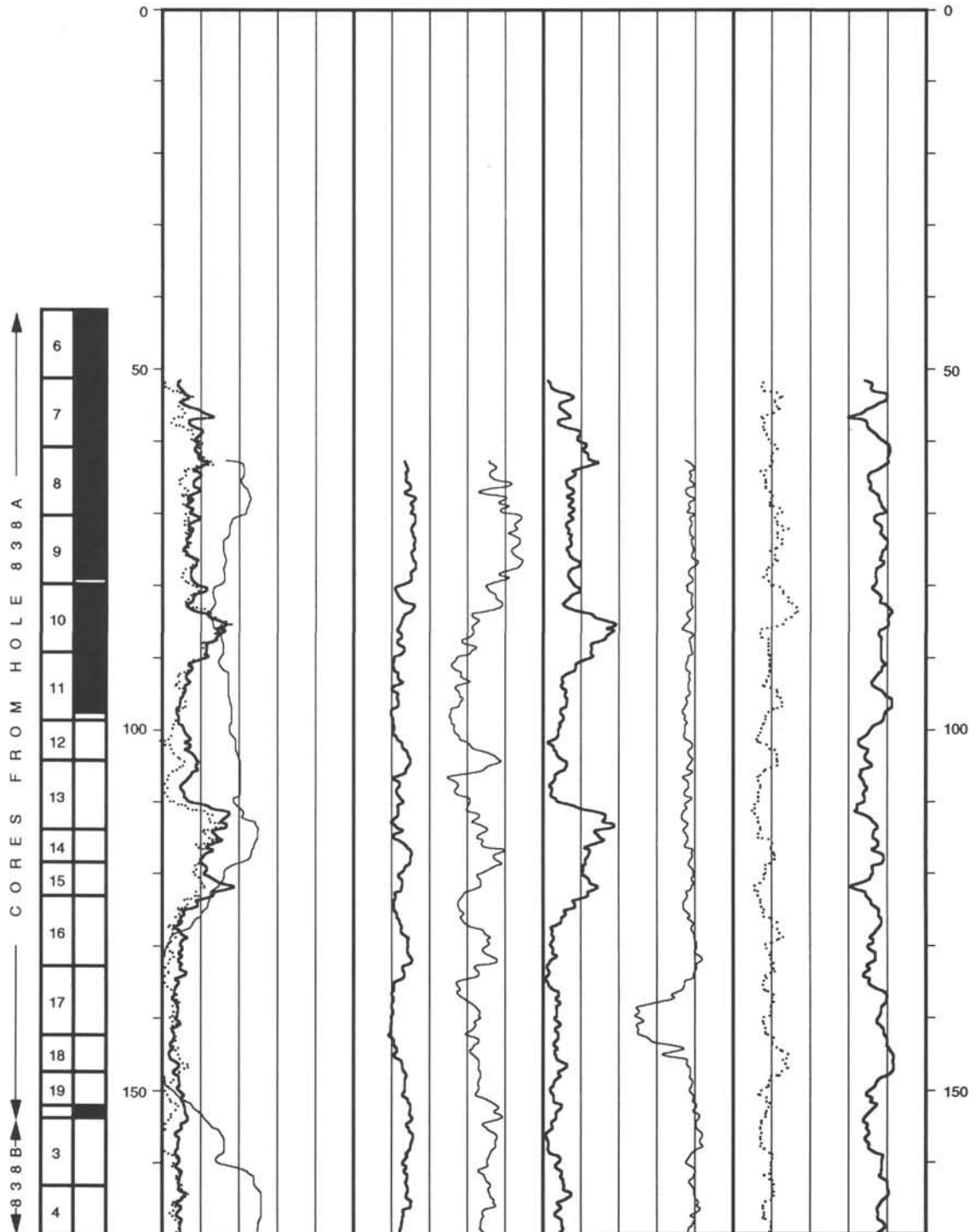
Ms 135A-108

NOTE: All core description forms ("barrel sheets") and core photographs have been printed on coated paper and bound separately as Part 2 of this volume, beginning on page 681.

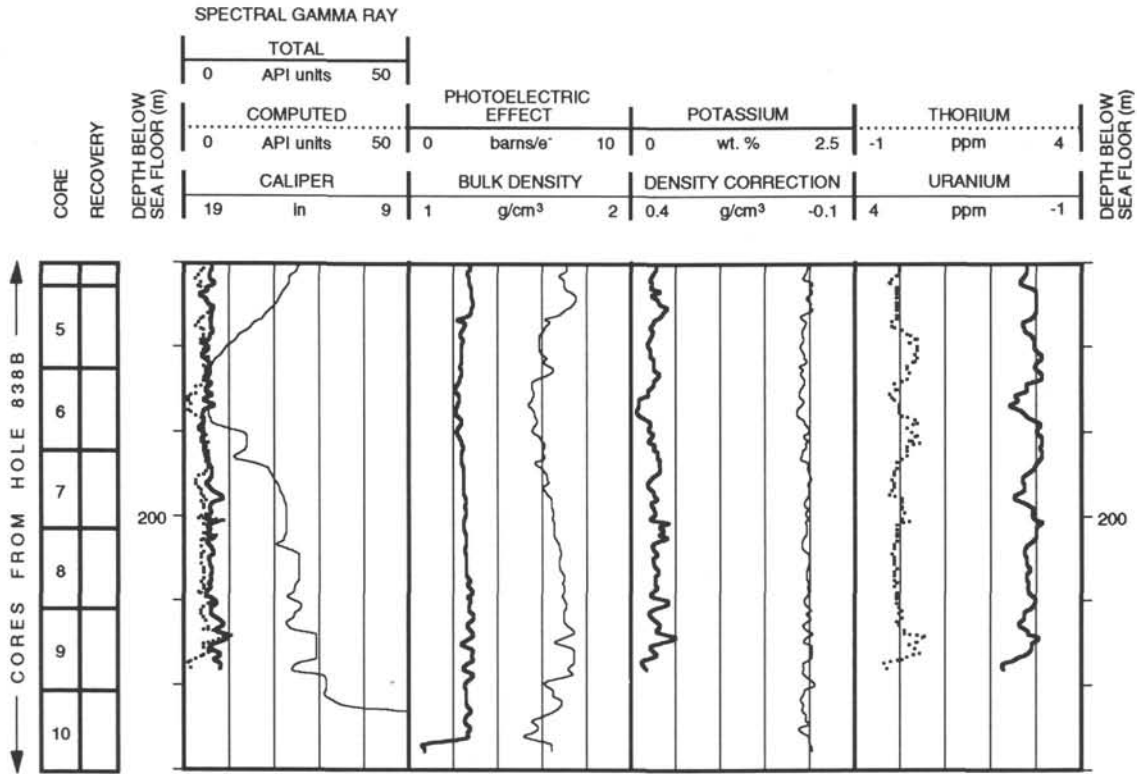
Formation microscanner images for this site are presented on microfiche in the back of Part 2.

Hole 838B: Density-Natural Gamma Ray Log Summary

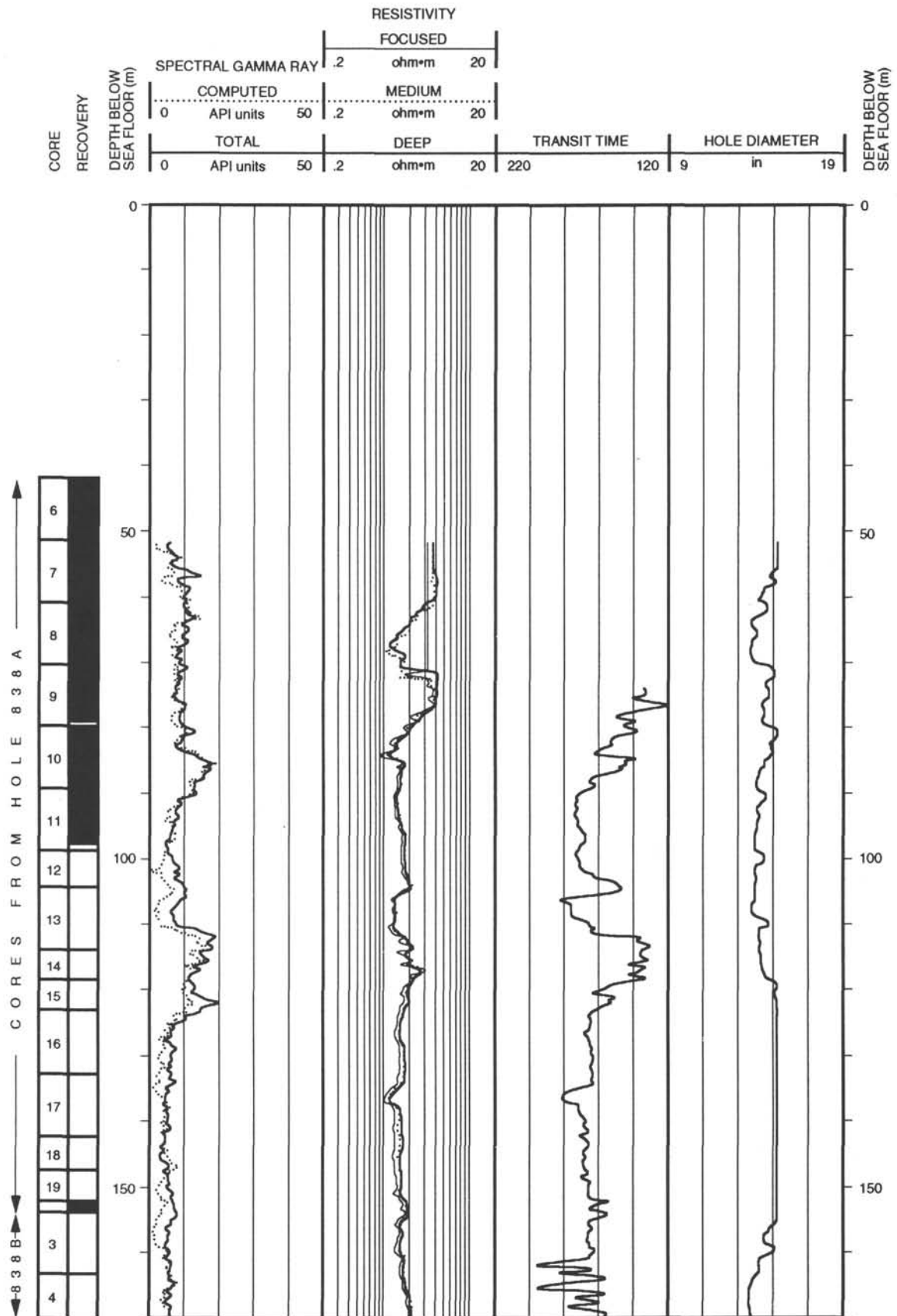
		SPECTRAL GAMMA RAY								
		TOTAL		PHOTOELECTRIC EFFECT		POTASSIUM		THORIUM		
CORE RECOVERY	DEPTH BELOW SEA FLOOR (m)	0	50	0	10	0	2.5	-1	4	DEPTH BELOW SEA FLOOR (m)
		API units		barns/e ²		wt. %		ppm		
		COMPUTED		BULK DENSITY		DENSITY CORRECTION		URANIUM		
		19	9	1	2	0.4	-0.1	4	-1	
		in		g/cm ³		g/cm ³		ppm		



Hole 838B: Density-Natural Gamma Ray Log Summary (continued)

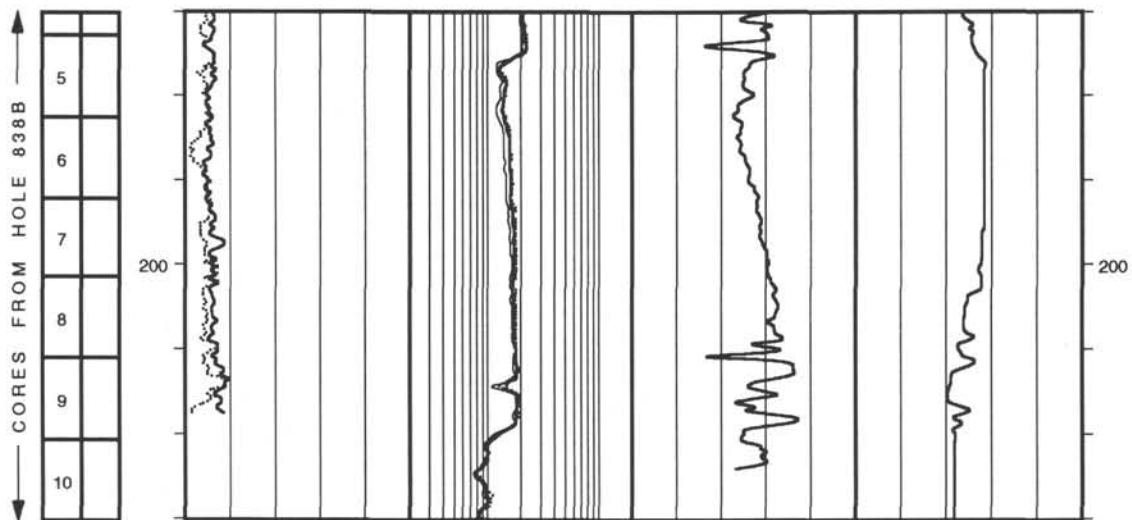


Hole 838B: Resistivity-Sonic-Natural Gamma Ray Log Summary

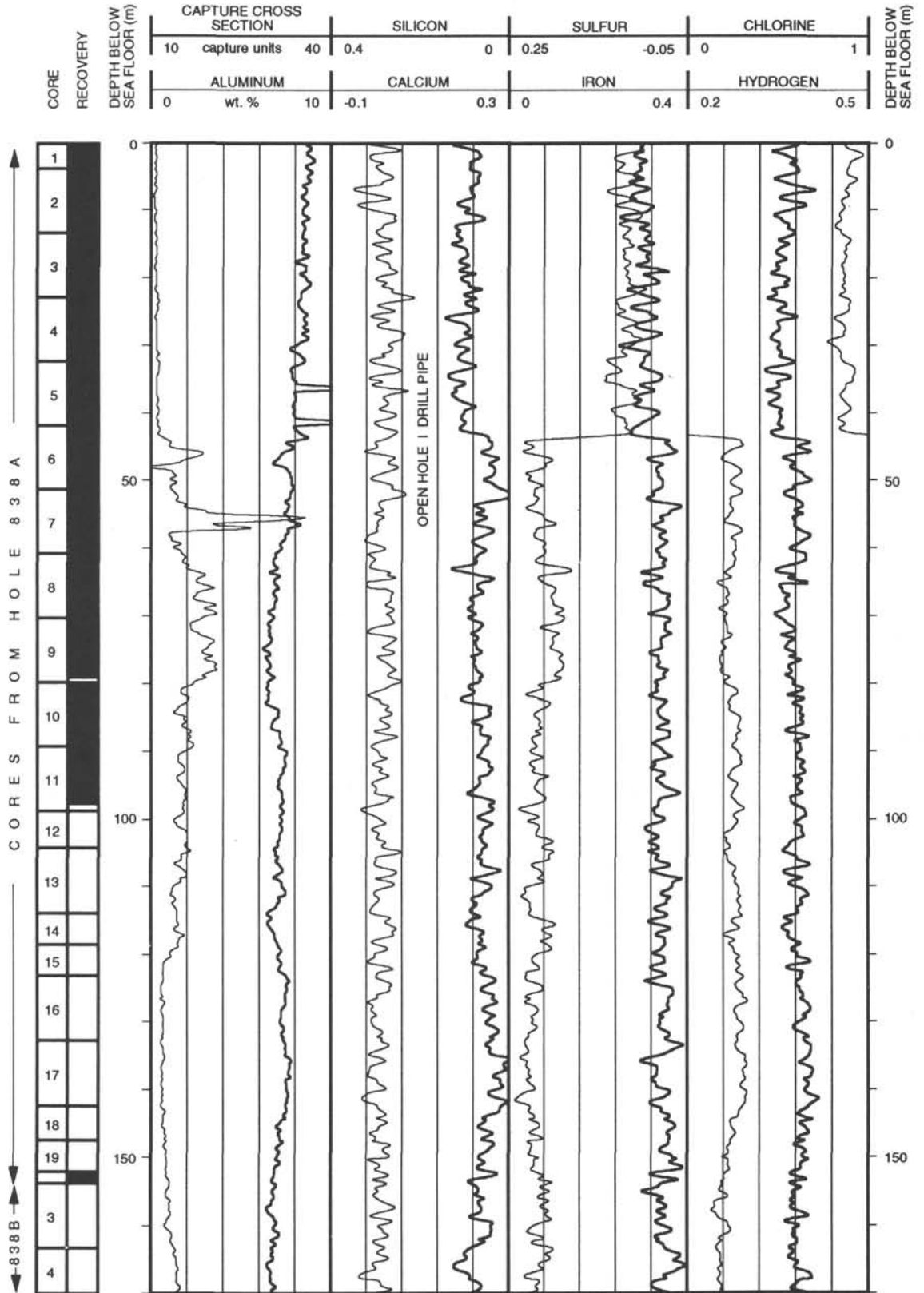


Hole 838B: Resistivity-Sonic-Natural Gamma Ray Log Summary (continued)

CORE RECOVERY	DEPTH BELOW SEA FLOOR (m)	RESISTIVITY								DEPTH BELOW SEA FLOOR (m)		
		SPECTRAL GAMMA RAY		FOCUSED		MEDIUM		DEEP			TRANSIT TIME	HOLE DIAMETER
		API units	50	.2	ohm*m	20	.2	ohm*m	20			
0	0	50	.2	ohm*m	20	220	120	9	in	19		



Hole 838B: Geochemical Log Summary



Hole 838B: Geochemical Log Summary (continued)

CORE RECOVERY	CAPTURE CROSS SECTION		SILICON		SULFUR		CHLORINE		DEPTH BELOW SEA FLOOR (m)
	10	capture units	40	0.4	0	0.25	-0.05	0	
	ALUMINUM		CALCIUM		IRON		HYDROGEN		
	0	wt. %	10	-0.1	0.3	0	0.4	0.2	0.5

